Title
Improvements on Vascular Magnetic Resonance Imaging

Author
Xie, Yibin

Publication Date
2015

UNIVERSITY OF CALIFORNIA

Los Angeles

Improvements on Vascular Magnetic Resonance Imaging

A dissertation submitted in partial satisfaction of the
requirements for the degree Doctor of Philosophy
in Biomedical Engineering

by

Yibin Xie

2015

ABSTRACT OF THE DISSERTATION

Improvements on Vascular Magnetic Resonance Imaging

by

Yibin Xie

Doctor of Philosophy in Biomedical Engineering

University of California, Los Angeles, 2015

Professor Daniel B. Ennis, co-Chair

Professor Debiao Li, co-Chair

Cardiovascular diseases are the leading cause of death globally and atherosclerosis is the primary underlying condition. Magnetic resonance imaging (MRI) is a promising diagnostic tool for evaluating atherosclerosis because of its excellent tissue contrast non-invasiveness. However many vascular MRI techniques have not been utilized clinically due to practical issues related to imaging speed, workflow, contrast media, and image quality. The primary focus of the work in this dissertation is to address some of these limitations and improve the capability of vascular MRI to accurately detect and characterize atherosclerotic lesions. Specifically, there are four areas of improvements of vascular MRI:

First, an online respiratory self-gating method (ADIOS) was developed for noncontrast magnetic resonance angiography of renal arteries. Some drawbacks of the conventional navigator gating method, including complicated planning and saturation artifacts were eliminated. Testing on healthy subjects confirmed that the proposed method was able to provide high-quality visualization of renal arteries with no navigator-induced artifacts, simplified setup, and shorter scan time.

Second, a diffusion-prepared turbo-spin-echo technique (DP-TSE) was developed to enable 3D high resolution diffusion weighted imaging for carotid plaque characterization without the need of contrast agent. The proposed method showed significantly higher vessel wall visibility, less distortion, and less partial volume effect. Apparent diffusion coefficient demonstrated the potential to differentiate lipid core from fibrous plaque tissue.

Third, a black-blood imaging technique (DANTE-SPACE) was developed to improve flow signal suppression in vessel wall imaging. A combined carotid and intracranial arterial wall imaging protocol was designed and tested. DANTE-SPACE demonstrated significantly improved arterial and venous blood suppression compared with conventional methods. Preliminary clinical study showed that the proposed method had the potential to detect vessel wall dissection and accurately differentiate plaque components.

Fourth, an imaging method for coronary plaque characterization was developed to allow simultaneous dark-blood T1-weighted imaging and bright-blood imaging. An image-based affine motion correction algorithm was designed to allow 100% respiratory gating efficiency. Results from healthy subjects demonstrated the feasibility of whole-heart coronary plaque imaging with isotropic high resolution. Preliminary results from patients with coronary artery disease showed the potential of this technique to detect intra-plaque hemorrhage and inflammation in the coronary wall.

The dissertation of Yibin Xie is approved.

Danny J.J. Wang

J. Paul Finn

Daniel B. Ennis, Committee co-Chair

Debiao Li, Committee co-Chair

University of California, Los Angeles

2015

TABLE OF CONTENTS

VITA

2008 BSE Biomedical Engineering, Zhejiang University, Hangzhou, China

2010 MSE Biomedical Engineering, Johns Hopkins University, Baltimore, USA

PEER-REVIEWED JOURNAL PUBLICATIONS

1. **Xie Y**, Fan Z, Saouaf R, Natsuaki Y, Laub G, Li D. Adaptive online self-gating (ADIOS) for free-breathing noncontrast renal MR angiography. Magn Reson Med 2014.
2. **Xie Y**, Yu W, Fan Z, Nguyen C, Bi X, An J, Zhang T, Zhang Z, Li D. High resolution 3D diffusion cardiovascular magnetic resonance of carotid vessel wall to detect lipid core without contrast media. J Cardiovasc Magn Reson 2014;16:67.
3. Nguyen C, Fan Z, **Xie Y**, Dawkins J, Tseliou E, Bi X, Sharif B, Dharmakumar R, Marban E, Li D. In vivo contrast free chronic myocardial infarction characterization using diffusion-weighted cardiovascular magnetic resonance. J Cardiovasc Magn Reson 2014;16:68.
4. Fan Z, Yu W, **Xie Y**, et al. Multi-contrast atherosclerosis characterization (MATCH) of carotid plaque with a single 5-min scan: technical development and clinical feasibility. J Cardiovasc Magn Reson 2014;16:53.
5. Nguyen C, Sharif-Afshar AR, Fan Z, **Xie Y**, Wilson S, Bi X, Payor L, Saouaf R, Kim H, Li D. 3D high-resolution diffusion-weighted MRI at 3T: Preliminary application in prostate cancer patients undergoing active surveillance protocol for low-risk prostate cancer. Magn Reson Med 2015. (In press)

6. **Xie Y**, Yang Q, Fan Z, Pang J, Xie G, Li D. Improved black-blood imaging using DANTE-SPACE for simultaneous carotid and intracranial vessel wall evaluation. Magn Reson Med 2015. (In press)

7. **Xie Y**, Kim Y, Pang J, Kim J, Yang Q, Fan Z, Chang H, and Li D. Whole-heart coronary plaque characterization with interleaved bright-blood imaging. Radiology. (In preparation)

8. Yang Q, Duan J, Fan Z, Qu X, **Xie Y**, Jin L, Bi X, Li K, Ji X, Li D. Magnetic resonance direct thrombus imaging identifies cerebral venous thrombosis. Annals of Neurology. (In review)

9. Xie G, Bi X, **Xie Y**, Liu X, Zheng H, Li D, Fan Z. Fast 3D submillimeter isotropic resolution MRI of peripheral vessel wall based using DANTE-prepared FLASH. J Magn Reson Imaging (In preparation)

SELECTED CONFERENCE ABSTRACTS

Xie Y, Kim Y, Pang J, Kim J, Yang Q, Fan Z, Chang H, Li D. ‘Time-efficient whole-heart coronary plaque characterization with simultaneously acquired MRA’, International Society for Magnetic Resonance in Medicine, 2015: a0557 (oral)

Xie Y, Yang Q, Fan Z, Xie G, Li D. ‘Improved black-blood imaging using DANTE-SPACE for combined carotid and intracranial vessel wall evaluation’, Society of Cardiovascular Magnetic Resonance, 2014: O 17 (oral)

Xie Y, Fan Z, Yu W, Nguyen C, An J, Zhang Z, Li D. ‘High resolution 3D diffusion MRI of carotid plaque on 3T’, Society of Cardiovascular Magnetic Resonance, 2014: O 028 (oral)

Xie Y, Yu W, Fan Z, Nguyen C, An J, Zhang Z, Li D. ‘High-resolution 3D diffusion MRI: detection of lipid-rich necrotic core in plaques without contrast media’, International Society for Magnetic Resonance in Medicine, 2014: a5028 (magna cum laude)

Nguyen C, Fan Z, Afshar A, **Xie Y**, Saouaf R, Kim H, Li D. ‘3D high resolution diffusion-weighted MRI at 3T: preliminary application in patients undergoing active surveillance protocol for low-risk prostate cancer’, International Society for Magnetic Resonance in Medicine, 2014: a4847 (summa cum laude)

Xie Y, Fan Z, Nguyen C, Li D. ‘Sub-millimeter 3D diffusion-weighted imaging of carotid arterial wall’, International Workshop on Magnetic Resonance Angiography, 2013

Xie Y, Fan Z, Natsuaki Y, Laub G, Saouaf R, Li D. ‘Adaptive efficiency-optimized self-navigation (ADIOS) for free-breathing non-contrast abdominal MRA’, International Society for Magnetic Resonance in Medicine, 2012: a4469 (magna cum laude)

Xie Y, Shea S, Fu Y, Gilson W, Ehtiati T, Ouwerkerk R, Kedziorek D, Solaiyappan M, Huang G, Valdeig S, Wacker F, Kraitchman D. ‘Using 19F MR to monitor delivery and engraftment of therapeutic stem cells invivo: accuracy evaluation’, International Society for Magnetic Resonance in Medicine, 2010: a1059 (oral)

ACKNOWLEDGMENTS

I am fortunate and privileged to have Dr. Debiao Li as my PhD advisor and mentor and I would like to thank him for his guidance and support throughout the program. I am grateful to him for the flexible and resourceful research environment at the Cedars-Sinai Biomedical Imaging Research Institute (BIRI). I benefited from the numerous discussions with him that sparked my creativity. Most importantly I learnt the vision and work attitude from him as a top scholar and a first generation Chinese American. His ideals such as “be prepared to impress people”; “always ask ‘what does it mean?’ of your work”; and “value at work lies in reliability” will surely benefit my career even after PhD.

Many thanks go to my PhD committee co-chair, Dr. Dan Ennis, and members, Dr. Danny JJ Wang, Dr Paul Finn and Dr Linda Demer for their help and advice.

Special thanks go to Dr. Zhaoyang Fan for his sincere help since the very beginning of my PhD. I benefited from his technical expertise and experience in vascular imaging on numerous occasions. He was often the first person I consulted whenever I needed an advice or a second opinion - a dependable colleague and a dear friend.

I also want to thank my clinical collaborators including Dr. Yang Qi at Xuanwu Hospital, Dr. Wei Yu at Anzhen Hospital and the team led by Dr. Hyuk-jae Chang at Yonsei University. The collaborations with them facilitated the crucial steps towards the clinical application of the innovations in this dissertation and I am grateful for their work.

It had the pleasure to work with the talented colleagues at BIRI (in alphabetical order): Dr. Jose Agraz, Dr. David Chen, Zixin Deng, Avinash Kali, Dr. Qi Liu, Christopher Nguyen, Dr. Jianning Pang, Scott Powel, Dr. Behzad Sharif, Jaime Shaw, Dr Guoxi Xie, Dr. Jingsi Xie, Randy Yang, and Zhengwei Zhou with whom I shared countless inspiring discussions and thoughts. They were a major fun factor in my pursuit of a PhD. In particular I want to acknowledge Dr Jianing Pang whose VIPR development provided a solid background for my coronary work, and Christopher Nguyen with whom I shared many endeavors in diffusion weighted imaging.

I am grateful for the invaluable support and expertise provided by Siemens team members including Drs. Gerhard Laub, Xiaoming Bi and Yutaka Natsuaki. I would also like to thank the current and previous admins at the BIRI and UCLA bioengineering, especially Eileen Shinn, Johanna Kim, Amy Smith, Anne-Marie Dieters, and Larry Nadeau.

I am indebted to my parents Jianguo Cao and Meiying Xie who gave much freedom for me to pursue my career and provided continuous support. Mostly importantly, I would like to thank my fiancé, Meng Liu, whose love and accompany made the PhD years the best time of my life.

LIST OF TABLES

LIST OF FIGURES

LIST OF ACRONYMS

1D/2D/3D – One/two/three dimensional
ABI – Ankle brachial index
ADC – Apparent diffusion coefficient
ADIOS – Adaptive online self-gating
ANOVA – Analysis of variance
BB – Black blood
bSSFP – Balanced steady-state free precession
CAD – Coronary arteries diseases
CCC – Cross-correlation coefficient
CE – Contrast-enhanced
CHD – Coronary heart disease
CNR – Contrast-to-noise ratio
CSF – Cerebrospinal fluid
CT – Computed tomography
DANTE – Delay Alternating with Nutation for Tailored Excitation
DCE – Dynamic contrast enhanced
DIR – Double inversion-recovery
DP-TSE – Diffusion-prepared turbo-spin-echo
DWI – Diffusion weighted imaging
ECG – Electrocardiography
FDG – Fludeoxyglucose
FLASH – Fast low angle shot
FOV – Field of view
GRAPPA – Generalized auto-calibrating partially parallel imaging
IVUS – Intravascular ultrasound
LDL – Low-density lipoprotein
LRNC – Lipid-rich necrotic core
MIP – Maximum intensity projection

MPR – Multiplanar reformation
MR – Magnetic resonance
MRA – Magnetic resonance angiography
MRI – Magnetic resonance imaging
NC MRA – Noncontrast magnetic resonance angiography
NAV – Diaphragm navigator
NIRS – Near-infrared spectroscopy
NSF – Nephrogenic systemic fibrosis
OCT – Optical coherence tomography
PAD – Peripheral artery disease
PET – Positron emission tomography
RF – Radio-frequency
ROI – Region of interest
SD – Standard deviation
SNR – Signal-to-noise ratio
SPACE – Sampling Perfection with Application optimized Contrasts using different flip angle Evolution
SS-DWEPI – Single-shot diffusion-weighted echo planar imaging

CHAPTER 1: INTRODUCTION

1.1 SIGNIFICANCE

Despite the revolutionary development of modern medicine, cardiovascular diseases, including coronary arteries diseases (CAD), stroke, peripheral artery diseases (PAD), remain the leading global cause of death. They account for approximately 17.3 million deaths per year, a number expected to increase to 23.6 million by 2030 [1]. They also have huge impact on global economy due to health expenditure and lost productivity. For example, the annual direct and indirect costs of cardiovascular diseases exceed $320 billion in US alone [1]. Improvements of the diagnosis and management of cardiovascular diseases would therefore have major impact on society and humanity.

Atherosclerosis, the hardening and thickening of arteries, is the underlying cause of cardiovascular diseases [2]. It is a condition in which plaques made of cholesterols, calcium, fibrous etc., build up in the arterial wall. Plaques can cause partial occlusion of the blood flow, leading to ischemia related conditions. Plaques can also rupture, break off, and cause total blockage of the artery, leading to debilitating conditions such as heart attack or stroke.

Magnetic resonance imaging (MRI) is a promising imaging modality gaining increased interest and application in evaluating atherosclerosis. Vascular MRI has several attractive advantages for potentially wide clinical application: (a) it is non-invasive; (b) it does not involve ionizing radiation; (c) it has relatively high spatial resolution and large anatomical coverage; (d) it has the capability to provide diagnostic information of both lumen and vessel wall; (e) it has excellent soft tissue contrast for identifying and differentiating plaque components.

1.2 OBJECTIVES

The broad, long term goal of the work in this dissertation is to improve vascular MRI for better diagnosis, prognosis, and management of atherosclerosis. The primary focus is on improving the capability of vascular MRI to accurately detect atherosclerotic lesions and characterize their vulnerability. Areas of improvements include imaging speed, image quality, robustness, and new image contrast mechanisms for biomarkers. Specifically, there are four research objectives in this dissertation:

Objective #1: To develop an online respiratory self-gating method for noncontrast magnetic resonance angiography of renal arteries

Cross-pair diaphragm navigator (NAV) is the current preferred technique for free-breathing noncontrast magnetic resonance angiography (NC MRA). However it requires additional planning, scout scans, and acceptance window setup/adjustments, which significantly complicate the exam and restrict its clinical application. The cross-pair navigator excitations cause signal saturation in part of the field-of-view, degrading the visualization of arteries. To overcome these limitations, we proposed to develop a self-gating (SG) method to replace NAV. The SG method was designed to derive respiratory motion information directly from the slab being imaged for online gating without the need for NAV. An online adaptive gating algorithm was developed to maintain scan efficiency and minimize respiratory motion artifacts. In vivo studies on healthy subjects provided the qualitative and quantitative assessments of image quality and results were compared with conventional diaphragm navigator (NAV). Results showed that the proposed method provided high-quality visualization of renal arteries with no diaphragm navigator-induced artifacts, simplified setup, and shorter scan time.

Objective #2: To develop a 3D diffusion weighed imaging method with high spatial resolution for carotid artery plaque characterization

Without the need of contrast media, diffusion-weighted imaging (DWI) has shown great promise for accurate detection of lipid-rich necrotic core (LRNC), a well-known feature of vulnerable plaques. However, limited resolution and poor image quality in vivo with conventional single-shot diffusion-weighted echo planar imaging (SS-DWEPI) has hindered its clinical application. We proposed to apply a diffusion-prepared turbo-spin-echo (DP-TSE) technique for carotid plaque characterization with 3D high resolution and improved image quality. DP-TSE used a diffusion encoding module separated from the TSE framework, allowing for segmented acquisition without the sensitivity to phase errors. In vivo studies on healthy subjects and patients investigated the comparison of DP-TSE vs SS-DWEPI in resolution and image quality, particularly image distortion and partial volume effects. DP-TSE allowed, for the first time, 3D DWI of the carotid arterial wall in vivo with high spatial resolution and improved image quality over SS-DWEPI. It showed the potential to detect LRNC without the use of contrast agent, allowing plaque characterization in patients with renal insufficiency.

Objective #3: to develop a 3D black-blood imaging method for simultaneously evaluating carotid and intracranial arterial vessel wall with improved blood suppression

Both carotid and intracranial atherosclerosis are common etiology for stroke and an ideal imaging method should cover both locations. Successful vessel wall imaging requires complete suppression of the blood in the lumen to provide a good vessel wall to lumen contrast for assessing vessel wall pathology. Conventional double inversion recovery is not compatible with thick slab 3D imaging and the inherent flow dephasing effects by variable flip angle turbo spin echo (SPACE) sequence are not sufficient for complete blood suppression, especially after contrast enhancement. We proposed that Delay Alternating with Nutation for Tailored Excitation (DANTE) pulse train combined with SPACE is a solution for combined carotid and intracranial vessel wall imaging with and without contrast enhancement. In vivo studies on healthy subjects and patients investigated the feasibility of simultaneous high-resolution carotid and intracranial vessel wall imaging, and evaluated the performance of DANTE-SPACE compared with SPACE in arterial and venous blood suppression.

Objective #4: to develop a method for time-efficient whole-heart coronary artery plaque characterization with simultaneously acquired bright-blood reference images

T1-weighted (T1w) MRI with or without contrast enhancement has been used for characterizing coronary plaques showing promising prognostic capability for predicting coronary events. However current protocols using conventional Cartesian acquisition and respiratory gating have several drawbacks hindering its clinical application, including long scan time, limited resolution, and limited coverage to proximal coronary segments. A separate bright-blood MRA acquisition is needed to provide anatomical reference due to highly suppressed background tissue in dark-blood T1w images. We proposed a method based on golden-angle 3D radial trajectory and interleaved dark-blood and bright-blood imaging acquisition to address these limitations. We developed an image-based affine motion correction algorithm to allow 100% gating efficiency of the MR data without inducing breathing artifacts. In vivo studies on healthy subjects demonstrated the feasibility of time-efficient T1w whole-heart coronary plaque imaging with isotropic high resolution and simultaneously acquired bright-blood reference. Results from patients with coronary artery disease showed the potential of this technique to detect intra-plaque hemorrhage and inflammation in the coronary wall.

1.3 DISSERTATION ORGANIZATION

In additional to the Introduction (**Chapter 1**), the main body of this dissertation is organized in six parts (Chapters 2-7). **Chapter 2** provides the context and essential background information for the work of vascular MRI. Atherosclerosis, as the target disease for this work, is described in details through its definition, causes, diagnosis, and treatment. State-of-the-art of different modalities for atherosclerosis imaging is reviewed. **Chapter 3** details the development of a respiratory self-gating method, adaptive online self-gating (ADIOS), for noncontrast magnetic resonance angiography of renal arteries. Qualitative and quantitative assessments of image quality are presented in comparison with conventional diaphragm navigator in healthy subjects. **Chapter 4** presents the development of a diffusion-prepared turbo-spin-echo (DP-TSE) technique for carotid artery plaque characterization with 3D high resolution and improved image quality. Testing and comparison in healthy subjects and preliminary clinical experience in stroke patients are also included. **Chapter 5** describes the work of combined carotid and intracranial vessel wall imaging using DANTE-SPACE for improved black-blood imaging. Simulations and phantom studies to quantify image contrast variations induced by DANTE are included. Additional results cover the comparison between DANTE-SPACE, SPACE and 2D TSE for apparent SNR, CNR and morphometric measurements. Preliminary clinical validation in symptomatic patients is reported. **Chapter 6** presents the technical development of a method for whole-heart, high resolution coronary plaque imaging with simultaneously acquired bright-blood reference. Methodology of the interleaved sequence design, joint motion compensation scheme, and image reconstruction processes are described in details. Preliminary clinical results from CAD patients and comparison with other imaging modalities are included. **Chapter 7** summarizes and concludes the improvements of vascular MRI described in this dissertation and suggests directions for future research and development in this area.

1.4 PREVIOUS PUBLICATIONS

Certain parts of this dissertation have been published previously. The work of adaptive self-gating for renal MRA was published as a journal paper in Magnetic Resonance in Medicine 2014 73:312 titled as *“Adaptive online self-gating (ADIOS) for free-breathing noncontrast renal MR angiography”*. The work of diffusion weighted carotid vessel wall imaging was published in Journal of Cardiovascular Magnetic Resonance 2014 16:67 titled as *“High resolution 3D diffusion cardiovascular magnetic resonance of carotid vessel wall to detect lipid core without contrast media”*. The work of black-blood carotid and intracranial vessel wall imaging was accepted for publication in Magnetic Resonance in Medicine 2015 titled as *“Improved black-blood imaging using DANTE-SPACE for simultaneous carotid and intracranial vessel wall evaluation”*. Lastly the work of coronary vessel wall imaging titled as *“Whole-heart coronary plaque characterization with interleaved bright-blood imaging”* was presented at the ISMRM Workshop on Non-Contrast Cardiovascular MRI at Long Beach, CA, 2015.

CHAPTER 2: BACKGROUND

2.1 ATHEROSCLEROSIS

2.1.1 Definition

Atherosclerosis is the condition of thickening and hardening of arterial wall (arteriosclerosis) due to atheromatous plaques. The word is a portmanteau of Greek words “ἀθήρα” (athera, meaning "gruel") and “σκλήρωσις” (sklerosis, meaning “hardening”). The thickened vessel wall may reduce the lumen size and cause restriction of blood flow (known as stenosis) leading to conditions related to insufficient blood perfusion (known as ischemia). A more detrimental consequence of atherosclerosis is plaque rupture, in which the plaque ulcerates and exposes its content material to the blood flow which forms a blood clot (known as thrombus). Thrombus can cause total occlusion of the vessel lumen and travel with blood flow to other parts of the body, blocking flow to another organ (known as embolism).

Atherosclerosis is a systematic disease that can affect any large artery in the body, including arteries in the heart, brain, kidneys, and extremities [3]. Depending on which arteries are affected, different diseases may develop: coronary heart disease (CHD) occurs when the blood vessels supplying heart muscle are affected by atherosclerosis, which can lead to the damage of the heart muscle (known as myocardial infarction, or heart attack); carotid artery disease and intracranial artery disease occurs when plaques build up in the major arteries in the neck and head, which can lead to ischemic stroke, the damage of brain tissue; peripheral artery disease occurs when the arteries in the limbs are affected by atherosclerosis, leading to numbness, pain, tissue death, and even amputation in serious cases; chronic kidney disease can occur if the renal arteries are affected by atherosclerosis, leading to the loss of renal function over time.

Atherosclerotic plaques are heterogeneous tissue made up of complex components, including collagen, fibrin, calcification, cholesterols, inflammatory cells such as macrophages, hemorrhage, fibrous and necrotic tissue, smooth muscle cells, micro vessels, and various kinds of cytokines. Plaque composition and condition vary significantly depending on the disease states and progression. Atherosclerotic plaques can be separated into two broad categories: stable and unstable (also known as vulnerable) lesions. Certain plaque components and condition are related to how vulnerable it is to rupture and cause catastrophic results. **Table 2.1** summarizes the current recognized properties of vulnerable plaques based on previous post-mortem studies on culprit lesions [4-6].

Table 2.1 Current recognized features of vulnerable atherosclerotic plaques

Morphology/Structure	Activity/Function
Thin fibrous cap	Active inflammation
Large lipid core	Endothelial dysfunction
Severe stenosis	Angiogensis, leaking vasa vasorum, and intra-plaque hemorrhage
Superficial calcification	Platelet aggregation
Positive remodeling	High oxidative stress
High shear stress	High matrix-digesting enzyme activity in the cap
Plaque fissure and injury	High apoptosis rate

2.1.2 Prevalence, Incidence and Mortality

Atherosclerosis affects a large population in the world and is the primary underlying condition for various cardiovascular diseases. The prevalence and incidence of major atherosclerosis-related diseases in US are summarized in Table 2 with data form the 2015 update from American Heart Association [1].

Table 2.2 Prevalence, incidence, and mortality of major atherosclerosis-related cardiovascular diseases in US (2013 data)

Disease	Prevalence	Incidence	Mortality
Coronary heart disease	15.5 M	935.0 K	375.3 K
Stroke	6.6 M	795.0 K	128.9 K
Peripheral artery disease	6.8 M	1.4 M (est.)	13.5 K
Heart failure	5.7 M	870.0 K	58.3 K

2.1.3 Causes, Risk Factors and Prevention

Atherosclerosis is a chronic disease that develops slowly and often remains asymptomatic for years [2]. The onset of the disease could begin as early as childhood [7]. Although the exact cause of the disease is still not clear, it is generally accepted that atherosclerosis is an inflammatory disease [3] that starts with damage or injury to the inner layer of an artery (endothelial cells). The damage may be induced by:

- High cholesterol and triglycerides in the blood
- Mechanical force due to high blood pressure
- Substance from tobacco due to smoking
- Diabetes
- Diseases that create a pro-inflammation environment such as lupus or arthritis

After repetitive micro injuries to the vessel endothelial layer, blood cells, cholesterols, and other cellular products may enter and build up in the vessel wall, forming an atherosclerotic plaque. This process usually takes decades to progress, depending on many genetic and physiological factors. There are ways to systematically assess the cardiovascular risk of an individual, such as Framingham Risk Score [8]. Besides the aforementioned direct causes of endothelial layer damages, additional risk factors are also known to be related to atherosclerosis:

- Physical inactivity
- Overweight and obesity
- Family history and genetics
- Metabolic syndrome

Although there are certain factors such as aging and genetic disposition that are not modifiable, atherosclerosis can be delayed or even prevented. In addition to the treatment of related diseases, certain lifestyle changes are proven effective to prevent atherosclerosis, including:

- Avoid tobacco smoke
- Eat a healthy diet with low saturated fat, cholesterol and sodium
- Exercising regularly
- Reduce stress
- Avoid overweight

2.1.4 Diagnosis Options

The first step of diagnosing atherosclerosis is a physical exam, during which doctors check for signs of narrowed or hardened arteries, such as: decrease in blood pressure in part of the body, weakened pulse, vascular bruits, signs of poor wound healing etc. Depending on the results, additional testing can be performed for specific diseases.

Coronary heart disease

- Electrocardiogram (ECG) – the recording of the electric signals from the beating heart, which can provide evidence of various cardiac abnormalities including myocardial damage due to coronary diseases;
- Imaging tests – imaging of the heart to evaluate the cardiac function and/or vascular narrowing using ultrasound (echocardiography), computed tomography, magnetic resonance imaging, or invasive angiography;
- Stress test – the use of physical activity or pharmaceutical agent to stimulate the heart in order to replicate the symptoms during excise. ECG, echocardiography and nuclear imaging can be used for evaluating the symptoms.

Stroke

- Blood test – detecting the level of cholesterol, glucose, and various blood components related to blood clotting;
- Imaging tests – imaging of the brain tissue and/or blood vessels using computed tomography, magnetic resonance imaging, or cerebral angiograms.

Peripheral artery disease

- Ankle brachial index (ABI) – an index comparing blood pressure in the ankle with the blood pressure in the arm;
- Imaging tests – imaging the blood vessels and evaluating the level of stenosis using ultrasound, computed tomography, magnetic resonance imaging, or invasive angiography.

2.1.5 Treatment Options

There are three categories of treatment for atherosclerosis. First, non-pharmaceutical therapies, such as quitting smoking and healthy diet are generally recommended. Second, various pharmaceutical therapies can be used to relieve the symptoms based on conditions, and to slow or even reverse the underlying atherosclerosis. Some common types of drugs include:

- Statins – to lower the level of low-density lipoprotein (LDL) cholesterol and slow the buildup of fatty deposits in the arterial wall;
- Thrombolytic drugs – to dissolve the thrombus formed by rupture plaques;
- Anti-platelet drugs – to reduce the aggregation of platelet onto areas of stenosis and prevent the formation of thrombus;
- Hypertension drugs – to treat the condition of high blood pressure which is a major risk factor for atherosclerosis;
- Beta-blockers – to lower the heart rate and reduce the cardiac demand, reducing the risk of heart attack.

Lastly, more aggressive surgical treatments may be suitable to alleviate the symptoms of specific conditions:

- Angioplasty – a procedure where a balloon-tipped catheter is inserted into the artery and advance to the lesion location under imaging guidance. The balloon is then inflated to open the vessel, deflated and removed. A stent may be placed to keep the artery open.
- Bypass surgery – a procedure where a piece of healthy blood vessel of similar size is removed from the leg, arm or abdomen and connected to the other arteries near the lesion so the blood flow is bypassed around the diseased area.
- Endarterectomy – a procedure where the plaque is surgically removed from the inner layers of the diseased artery. It is performed only on arteries that are large and easily accessible, such as the carotid arteries.

2.2 STATE OF THE ART OF ATHEROSCLEROSIS IMAGING

2.2.1 X-Ray Angiography

X-ray angiography is a projectional radiography using x-ray based techniques such fluoroscopy to image the lumen of blood vessels. It uses a catheter to inject x-ray contrast medium (typically iodine-based) which is opaque under x-ray into the target blood vessel lumen to evaluate the level of stenosis. Depending on the location of the angiogram, catheter access to the blood vessel is gained through one of the large blood vessels such as femoral artery or jugular vein. Commonly performed types of x-ray angiography include coronary angiography, cerebral angiography, abdominal angiography and peripheral angiography.

X-ray angiography is considered as the “gold standard” for evaluating luminal stenosis with high resolution and accuracy. However its application is limited due to the invasiveness and the involvement of ionizing radiation. Iodine-based contrast agent is also associated with a significant risk of severe reaction [9].

2.2.2 Computed Tomography (CT) Angiography

CT angiography is also an imaging modality based on X-ray. Intravenous contrast medium is used to produce a high contrast angiography. Current generation of CT uses multiple-row detectors and a continuously rotating x-ray source to acquire volumetric data of the target vasculature. The images can be reformatted and reviewed in different planes and orientations.

Besides luminal information, certain plaque components can also be evaluated with CT. Calcification can be readily identified by CT due to high attenuation and the quantification of calcium (calcium score) can be used as a risk assessment tool to provide predictive clinical information [10]. CT can also provide limited differentiation between fibrous plaques and lipid-rich plaques, although there is a large degree of overlap.

The accuracy of CT to evaluate stenosis can be affected by heavy calcification, of which the high signal can obscure the visualization of arterial lumen. CT also involves ionizing radiation and iodine-based contrast, which are associated with increased cancer risk and allergic reactions, respectively. However CT has a high negative predictive value, which is useful for screening low or intermediate risk patients.

2.2.3 Positron Emission Tomography (PET)

PET uses radiolabeled tracers that accumulate preferentially in certain tissues of target. For example fludeoxyglucose (FDG), the most commonly used PET agent, is a glucose analog which can be used as an indicator for cellular metabolic activity. Active inflammation and high macrophage content in vulnerable atherosclerotic plaques will lead to high FDG update therefore can be detected by FDG-PET.

FDG-PET has been used for the characterization of plaques in large arteries such as aorta and carotid arteries, showing a good correlation with macrophages staining [11]. FDG uptake in the carotid plaques has been shown to decrease with treatments as statin and lifestyle improvements.

However the limited spatial resolution (>3 mm) and high myocardial uptake make it difficult to use PET for the evaluation of coronary diseases. The ionizing radiation and high cost associated with PET scans are prohibitive for screening and serial monitoring.

2.2.4 Intravascular Imaging

Intravascular ultrasound (IVUS), optical coherence tomography (OCT), and near-infrared spectroscopy (NIRS) are all catheter-based techniques in which a detector is placed inside of the diseased artery to directly evaluate the vessel wall. The presence of atherosclerosis, plaque burden and composition can be evaluated based on the differences in acoustic, optical, and spectral properties between different tissue types, respectively.

IVUS uses a miniature ultrasound transducer to measure the acoustic properties of the vessel wall. Signal intensity in IVUS images are based on the ultrasound reflection and scattering between different tissues. IVUS has the capability to detect the presence of lipid pools with high specificity although its sensitivity is limited [12]. Newer IVUS techniques using spectral analysis of the ultrasound signal can provide more refined differentiation of plaque composition [13].

OCT uses an intravascular optical probe to measure the interference of light by the tissue. It provides high resolution (10-20 um) cross-sectional images of the tissue in situ. OCT has the capability to differentiate different plaque types: fibrous plaques appear as homogeneous, signal-rich regions; fibrocalcific plaques as well-delineated, signal-poor regions with sharp borders; and lipid-rich plaques as signal-poor regions with diffuse borders [14]. However the penetration of OCT is limited due to optical attenuation therefore it can only assess the superficial layers of the vessel wall. It also requires blood-free field of view which may add significant complexity to the exam.

NIRS is another optical imaging method to characterize plaques. The NIRS probe contains a light source which emits near infrared light with wavelength of 800 to 2500 nm. The probe then convert the diffuse reflectance signals from the tissue after scattering and absorption to produce a spectrum. NIRS has been validated to reliably detect the lipid content in the plaque which has a unique chemical signature by the combination of scattering and absorption [15].

However, all three intravascular imaging modalities require the invasive catheterization procedure and are often performed together with x-ray angiography. The additional cost associated with these tests and the limited availability are restrictive for their wide application.

2.2.5 Vascular MRI

MRI has a noninvasive, non-radiation imaging modality that is capable of assessing both lumen and vessel wall, providing comprehensive evaluation of atherosclerotic lesions.

MR angiography (MRA)

MRA can be performed with or without contrast agent (gadolinium). Contrast-enhanced MRA is commonly used for evaluating aorta, carotid, renal, and peripheral arteries with high SNR and large spatial coverage. Fast low-angle shot (FLASH) is the common choice of sequence for its shortened scan time. Additionally, arteriovenous passage of contrast agent can be visualized as a time-resolved series of images using dynamic sequences [16], to acquire functional information such as blooding filling time.

MRA can also be performed without contrast agent by utilizing flow or relaxation characteristics to generate contrast between luminal blood and static background tissue. Noncontrast MRA has regained an important clinical role due to the concern of nephrogenic systemic fibrosis (NSF) associated with gadolinium contrast usage in patients with renal insufficiency [17]. Time-of-flight and phase-contrast are commonly used techniques. There are flow-independent techniques such as T2 preparation and balanced steady-state free precession that exploit the T1 and T2 differences to isolate arteries form background tissues [18]. However despite its advantages, noncontrast MRA is not used routinely in clinics due to issues in robustness and workflow.

Vessel wall imaging

Vascular MRI can also directly evaluate vessel wall by eliminating the signal from luminal blood with various pulse sequence design, known as black-blood imaging. Through the use of multiple contrast weightings (T1, T2, and proton-density weighting), MRI has the capability of characterizing plaques. Specific plaque features that are related to its vulnerability, including fibrous cap integrity, lipid-rich/necrotic core, intraplaque hemorrhage, and calcification can be differentiated by vascular MRI methods [19].

However the majority of the work in vessel wall MRI has been focused on carotid, aorta, and peripheral arteries. Coronary vessel wall MRI is still in the early stages of development due to motion, resolution, and scan time limitations.

2.2.6 Comparison of Atherosclerosis Imaging Techniques

A comparison of the aforementioned imaging modalities for evaluating atherosclerosis is summarized in Table 3.

Table 2.3 Comparison of current imaging techniques for atherosclerosis

Technique	Evaluation		Spatial resolution	Invasive	Requires contrast agent	Ionizing radiation
	Lumen	Wall				
X-ray angiography	Yes	No	50-200 μm	Yes	Yes	Yes
CT angiography	Yes	Limited	~500 μm	No	Yes	Yes
Positron emission tomography	No	Yes	4-5 mm	No	Yes	Yes
Intravascular ultrasound	Yes	Yes	70-250 μm	Yes	No	No
Optical coherence tomography	Yes	Yes	5-20 μm	Yes	No	No
Near-infrared spectroscopy	No	Yes	100 μm	Yes	No	No
Vascular MRI	Yes	Yes	~1 mm	No	No	No

CHAPTER 3: ADAPTIVE SELF-GATING FOR FREE-BREATHING RENAL MRA

3.1 INTRODUCTION

Noncontrast MR angiography (NC MRA) based on balanced steady-state free precession (bSSFP) and slab-selective inversion-recovery (IR) magnetization preparation has become an attractive alternative for imaging renal arteries [20, 21] without the risk of nephrogenic systemic fibrosis (NSF) associated with gadolinium-based MR contrast agents [17, 22]. Besides the benefits of being contrast-free, NC MRA has additional unique advantages over its contrast-enhanced counterpart. It does not require accurate timing of the acquisition at the first-pass of contrast bolus in order to achieve optimal contrast and venous suppression [23]. Furthermore, ECG-triggering can be used to minimize blurring due to the aortic pulse wave [24]. However the use of bSSFP 3D high resolution acquisition with inversion-recovery magnetization preparation results in a relatively long scan time necessitating the usage of free-breathing approaches. Although bSSFP-based NC MRA has been proposed and developed for almost a decade [25], it has not become a routine clinical exam. One of the major hurdles has been the lack of a robust free-breathing approach to alleviate respiratory motion artifacts.

Currently, diaphragm navigator (NAV) [26] using cross-pair or 2D pencil beam is a preferred free-breathing technique. However, NAV significantly complicates exams due to its excitation volume setup, scout scans, and acceptance window setup/adjustments. Additionally, diaphragm motion only correlates to, rather than linearly represents the respiratory motion at the target slab, and the relationship between the two, defined as the ‘tracking-factor’, has been shown subject-specific as suggested by the work on coronary MRA [27]. Another cause of NAV failure is poor signal-to-noise ratio (SNR) from the liver-lung interface in some patients [28]. Based on our experience this is due to the relatively distal location of diaphragm dome from the imaged abdominal slab causing poor field homogeneity and coil sensitivity at the liver-lung interface in some subjects, especially with wide-bore, high field (>=3T) scanners. The additional cross-pair navigator excitations cause signal saturation in part of the abdominal region, which degrades the visualization of arteries in some subjects.

Respiratory gating with abdominal bellows [29] is an alternative method for free-breathing acquisition with some unique advantages. For example, the usage of bellows does not disrupt imaging sequence or interfere with magnetization preparation. However, bellows signal is not quantitative and does not vary linearly with respiratory motion at the slab being imaged [30], although it correlates with diaphragmatic and heart motion under regular breathing patterns [31]. Therefore gating with bellows is not compatible with slice-tracking or retrospective motion correction. Its performance under varying breathing pattern is also problematic due to signal drift and nonlinear rescaling [32]. Setup of the bellows also increases patient preparation time and prevents the use of ECG triggering in some scanners, leading to suboptimal inflow effect and aortic pulse wave induced blurring [24].

To overcome some of these limitations, various self-gating (SG) methods have been developed that derives motion information directly from MR signal of the volume being imaged [33-35]. Online self-gating is especially attractive clinically as it uses the derived motion information to guide data acquisition and/or motion correction on-the-fly therefore does not require additional post processing or reconstruction. Recently, SG has been applied to carotid vessel wall MRI to prevent artifacts from swallowing motion [36]. So far no online SG techniques have been applied in abdominal MRA to our knowledge. In this work, we developed a real-time SG technique, adaptive online self-gating (ADIOS), for free-breathing bSSFP-based renal NC MRA with adaptive scan efficiency and minimized respiratory motion artifacts. The feasibility of the new NC MRA technique was demonstrated in healthy volunteers by a comparison with the conventional NAV technique.

3.2 METHODS

3.2.1 Self-Gating with Inversion-Recovery Prepared bSSFP

The design of the online SG sequence is based on the clinical NC MRA protocol using inversion-recovery prepared slab-selective bSSFP. According to the central slice theorem, Fourier transform of a k-space center readout line without partition or phase encoding is the 1D projection of the entire imaging slab onto the readout direction [36]. Because respiratory motion in the abdominal region has its largest displacement in the superior-inferior (SI) direction [37], an additional central k-space SG readout line in the SI direction is acquired to probe the respiratory motion at the excited slab. This SG line is embedded as an extra line at the end of each bSSFP readout block to avoid eddy current effects induced by the SI readout gradients on the following imaging data (**Figure 3.1a**). This design also minimizes the temporal delay between SG lines and imaging data compared to using a separate SG module. Since the SG line is integrated and acquired only once per TR, the cost of SG on scanning efficiency is negligible (1 to 2%, depending on the number of segments). The field-of-view of the SG projection in the SI direction is set to the slab thickness and further cropped to its central 50% in order to exclude static edges introduced by the slab-selective excitation and inversion. The other acquisition parameters of the SG line are chosen identical to the imaging lines.

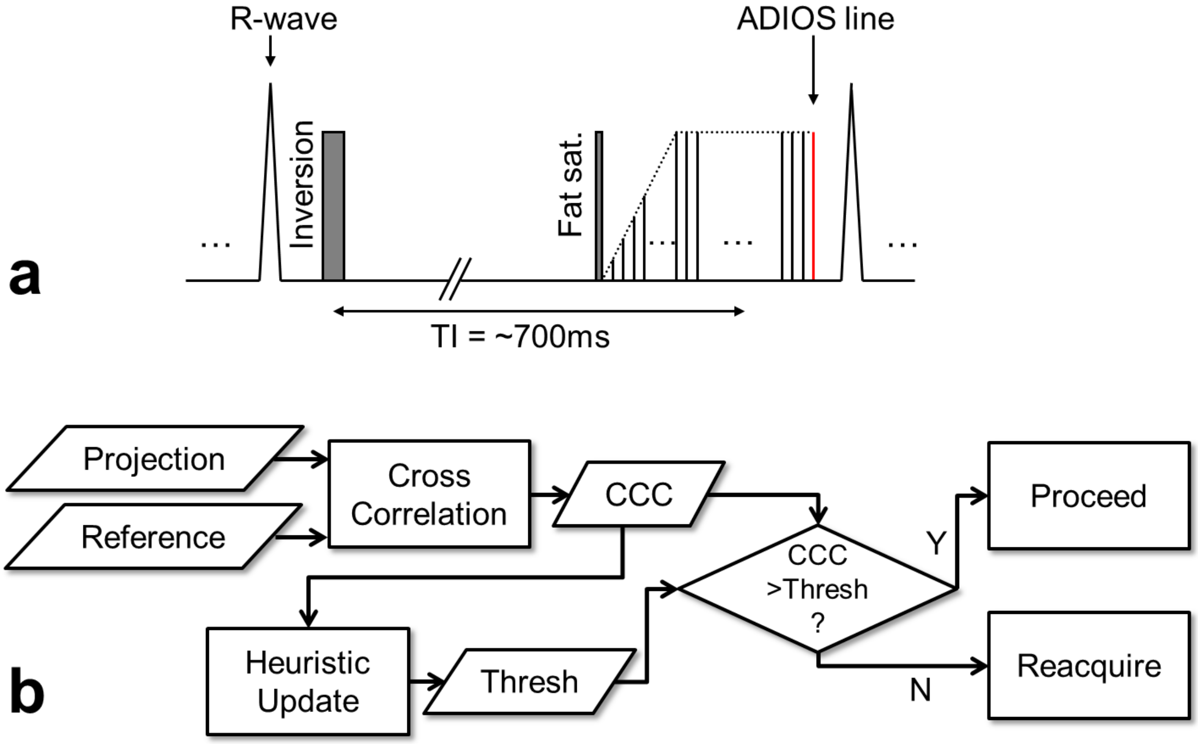

Figure 3.1 a: The pulse sequence diagram of ADIOS bSSFP NC MRA. It is based on the conventional NC MRA sequence which uses a slab-selective inversion RF pulse to suppress background tissue followed by fat-saturation, linear ramp-up catalyzing pulses and bSSFP block. An additional alpha pulse and central k-space readout (no phase encoding) is appended at the end of each bSSFP block to acquire a self-gating line. Readout gradient is set to superior-inferior direction for maximal sensitivity to respiratory motion. b: The schematic diagram of the ADIOS adaptive gating algorithm used for free-breathing NC-MRA. Cross-correlation coefficient (CCC) is calculated between projection profiles and reference profile. Online gating is executed based on CCC versus the threshold. The threshold is updated in real-time using a heuristic method to maintain scan efficiency. All calculations are performed online.

3.2.2 Adaptive Online Self-Gating

We developed a projection-based cross-correlation analysis for the online motion detection. The 1D projection of the imaging slab in the SI direction serves as the ‘fingerprint’ of the current respiratory phase. The scan starts with a brief breath-hold at end-expiration to record the reference projection profile in the second repetition. The first repetition is not used due to the transition to steady state. In each of the subsequent repetitions, a cross-correlation coefficient (CCC) is calculated between the current projection profile and the reference profile. Respiratory motion is detected if the CCC value drops below a defined threshold and the current image lines will be rejected and reacquired in the next repetition. In order to compensate for signal drift and maintain scan efficiency, the threshold is automatically adjusted using a heuristic algorithm in real time. The algorithm stores the ten most recent CCC values sorted in descending order. The threshold is constantly updated to the fourth highest CCC values resulting an acceptance rate of approximately 40%. CCC outliers with abnormal low values (below mean value minus four times of standard deviation) caused by possible bulk movement are excluded from the calculation and a warning message will appear to suggest rescan (**Figure 3.1b**). The initial threshold is set conservatively (0.998) to avoid motion in the data before the automatic algorithm starts regulating the threshold. The reference profile is unchanged throughout the acquisition to maintain the consistency of the heuristic algorithm.

3.2.3 Automatic Coil Combination for Reducing Static Tissue in Self-Gating

One of the drawbacks of projection-based SG is the inclusion of static tissue in the SG profile, which may lead to reduced sensitivity to detecting motion. The multi-coil arrays used for parallel imaging can be utilized to improve respiratory motion estimation with their redundant information [38]. In principle, each array coil has localized sensitivity profile, which includes different amount of static tissue leading to different levels of sensitivity to respiratory motion. Coils that are motion insensitive will compromise the performance of self-gating if a simple combination method is used, such as sum-of-square. Therefore, a coil combination method that excludes those motion-insensitive coils is necessary. Additionally, the method needs to be computationally efficient to operate in real-time for online self-gating. In this work, CCC is calculated individually from each coil with respect to its own reference and then combined into one value with a custom self-weighting function:

$$CCC_{weighted} = 1 - \sqrt{\sum\nolimits_{all\ coils} (1 - CCC_i)^2}$$

where CCC_i is the CCC value calculated from the ith coil. In this formulation CCC values derived from motion-insensitive coils are automatically ‘weighted down’ due to their lack of variation compared to those derived from motion-sensitive coils. As a result, the negative effects caused by static tissue are reduced for more accurate self-gating.

3.2.4 In Vivo Study and Self-Gating Signal Validation

Fifteen healthy volunteers (7 males, 8 females, age range 23–51 years, mean age 32 years) were recruited in accordance with institutional review board approval and scanned on a 3T clinical scanner (MAGNETOM Verio, Siemens AG Healthcare, Erlangen, Germany) using slab-selective inversion-recovery prepared bSSFP. Scan parameters include: ECG-triggered 41 lines/heartbeat; slab-selective inversion TI = 550-750 ms; acquisition time = 4-7 min depending on heart rate; TE/TR = 1.9/3.8 ms; 3D transverse slab with left-right readout; field-of-view (FOV) = 340×201×88 mm^2, image matrix = 304×192×40, yielding acquired spatial resolution = 1.1×1.1×2.2mm^3 (interpolated to 1.1mm isotropic); parallel imaging GRAPPA = 2; bandwidth = 780 Hz/pixel; flip angle = 90°. For comparison, NC MRA with conventional NAV were acquired immediately before or after in a randomized fashion using identical parameters and 6 mm gating window.

To validate the SG signal against the diaphragm NAV, two additional test scans were performed on 3 healthy volunteers in a pre-study. In the first test scan, identical FOV and other scanning parameters as previously described were used except that both NAV and SG readout were enabled in the same scan after the acquisition window during each repetition. The scan was set up for monitoring only and no gating was used. SG readout and NAV readout in each repetition have negligible temporal delay (<20ms) for respiratory motion analysis, therefore are considered simultaneously acquired. To evaluate the effects of slab-selective IR on SG performance, the second test scan was acquired in the same way as the first one except that no slab selective IR preparation was used.

3.2.5 Image Quality Evaluation and Statistics

Subjective qualitative scores and maximal vessel length

A blinded, randomized reading was performed on images of all volunteers acquired with both free-breathing techniques by two reviewers in consensus on a workstation (Leonardo; Siemens AG Healthcare, Erlangen, Germany). Coronal and axial maximum intensity projections were performed to visualize the entire arterial tree while removing overlapping background tissues. Image quality was analyzed for three predefined segments: 1, abdominal aorta; 2, proximal renal arteries including main renal artery and extra-parenchyma branches; 3, distal renal arteries of intra-parenchyma segmental branches. A 5-point scale was used: 1, not diagnostic (no vessel visible); 2, poor (irregular delineation of vessel with significant blurring); 3, acceptable (moderate artery delineation with appreciable blurring at some locations); 4, good (good delineation with minor boundary blurring at some locations); and 5, excellent (sharp and complete vessel delineation with little or no boundary blurring). In addition, maximal visible vessel length for each kidney was measured by manual tracing from the ostium to the end of the most distal branch using the distance measurement tool on the workstation.

SNR and CNR measurements

Mean signal intensities of arterial blood (SI_{artery}) were measured in the proximal-middle portion of the left and right main renal arteries with user-specified ROIs placed within the lumen. The ROIs were randomly selected from either NAV or ADIOS image and copied over to the other image on the workstation. In case of slight translational mismatch between the NAV and ADIOS images, the ROIs were manually adjusted. Otherwise the ROIs were identical between ADIOS and NAV. Additional ROIs with area of at least 15 mm^2 were drawn within uniform areas in the medullae of right and left kidneys and signal mean (SI_{kidney}) and standard deviation (SD_{kidney}) were calculated. SD_{kidney} was used as an estimate of noise [28] because the SD of a ROI outside of body could not be used due to the inhomogeneous noise distribution with parallel imaging [39]. Relative SNR and CNR were calculated as: $rSNR = SI_{artery}/ SD_{kidney}$ and $rCNR = (SI_{artery} - SI_{kidney})/ SD_{kidney}$.

Vessel sharpness

Vessel sharpness was measured using a previously published method [40]. Multiplanar reformatting was performed for each 3D data set to reconstruct a 2D cross-sectional image perpendicular to the vessel axis with 1.1mm thickness at the proximal-middle portion of each main renal artery. The locations were chosen at 2 cm distal to the renal artery ostia, same for both NAV and ADIOS images. Each 2D image was magnified (4x) by interpolation using a custom MATLAB program (ver. 2011b, The Mathworks, Natick, MA) and signal intensity profile was obtained along a user-defined line crossing the lumen center in anterior-posterior direction. On each side of the profile, the distance between the 20% and 80% points between the maximal lumen and background signal intensities were determined. The distance was averaged between both sides and the two 2D images from each 3D data set. Vessel sharpness is calculated as the reciprocal of the averaged distance.

3.3 RESULTS

3.3.1 Self-Gating Signal Validation

Three healthy subjects were successfully scanned with both NAV and SG readout enabled to validate SG signal against conventional NAV. The test scan with IR preparation showed apparently attenuated 1D SG projection profiles compared to the ones without IR preparation (**Figure 3.2a** versus **Figure 3.2d**). In both test scans, nonetheless, SG projection profiles clearly varied according to the underlying respiratory motion and SG CCC values were well matched temporally with diaphragm NAV positions (**Figure 3.2b, c** and **Figure 3.2e, f**). Quantitative analysis showed that the temporal correlation coefficients between SG CCC values and NAV positions was 0.76, 0.91, and 0.87 for the three subjects, respectively, with IR; while 0.82, 0.88, and 0.90 without IR (all $p<0.04$).

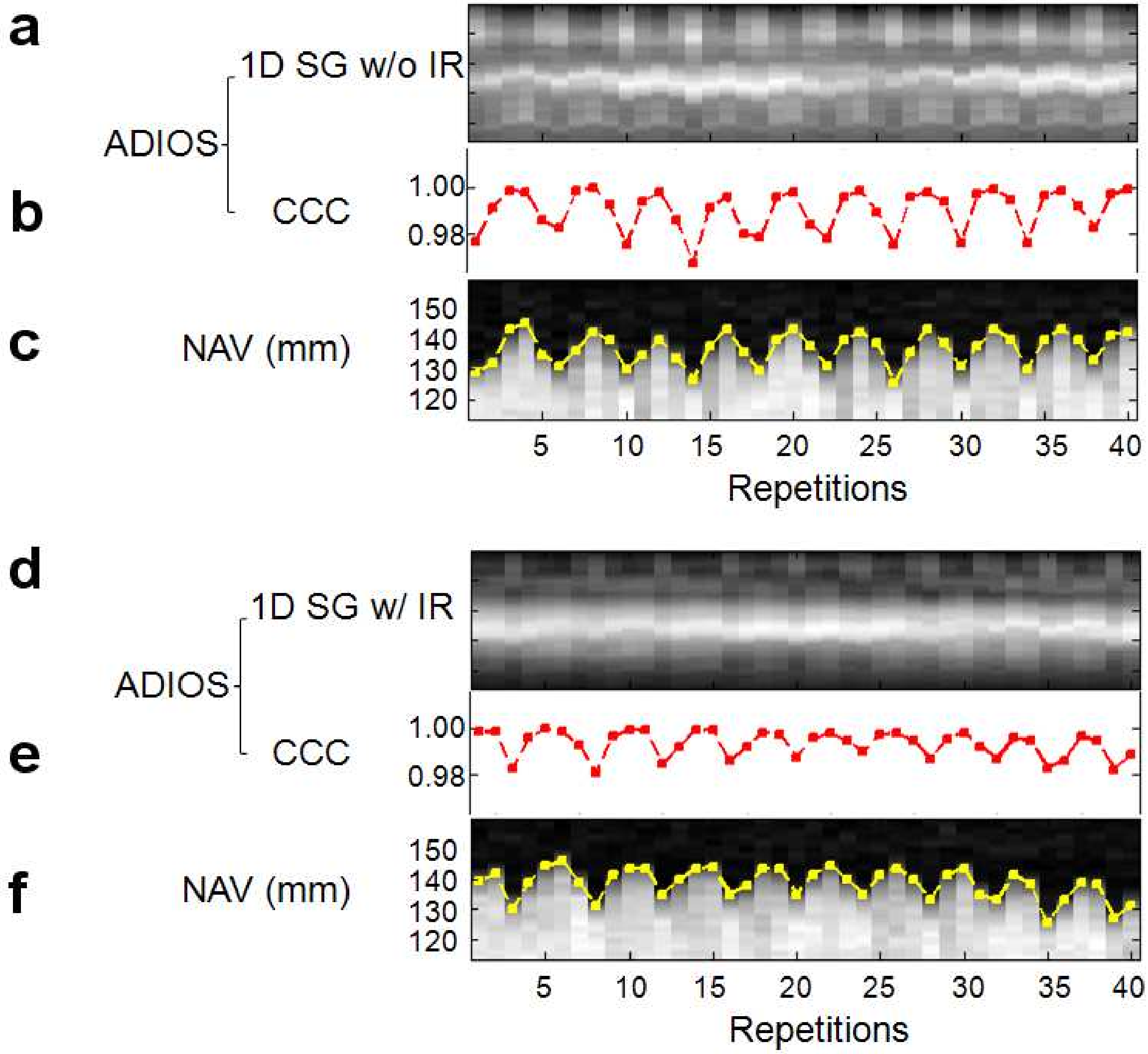

Figure 3.2 1D SG projection profiles without slab-selective inversion recovery (IR) (a) and with IR (d), compared with simultaneously acquired reference diaphragm navigator projections (c, f), all clearly showing variations due to underlying respiratory motion. CCC values (b, e) derived from SG projections showed high temporal correlation to the reference navigator positions (edge tracing in c, f), with temporal correlation coefficient of 0.87 with IR and 0.90 without IR (both p<0.04).

3.3.2 ADIOS Performance in Healthy Subjects

All fifteen healthy volunteers completed the exam with both ADIOS and conventional NAV gating. Bulk motion was detected by ADIOS during the scan of one subject. Relative SNR, relative CNR, subjective reviewer scores of the proximal-middle arteries, and vessel sharpness measurements were tabulated in Table 1. Subjective reviewer scores of the middle-distal arteries, maximal visible vessel length measurements, and scan time information were tabulated in Table 2. A two-tailed paired t-test was performed for all measurements to determine the statistical significance of the differences between ADIOS and NAV. All measures except the p values were presented in the format of ‘mean ± standard deviation’ as well as ‘mean paired difference ± standard deviation’ in the tables. To control for the effects of scan time on image quality, all subjects were retrospectively sorted based on their scan time and divided into two groups: in Group A (n=9), ADIOS and NAV had similar scan time (5’37”±1’8” for ADIOS vs. 5’43”±1’6” for NAV, p=0.46); in Group B (n=6), NAV used significantly longer scan time than ADIOS (mean difference between ADIOS and NAV = -2’18”±52”, p=0.002). Data from Group A, Group B, and both combined (Group T) were presented in the top, middle, and bottom four rows in the tables, respectively.

In general (Group T), satisfactory visualization of the renal arteries was achieved bilaterally except in one subject who has congenital solitary kidney. ADIOS had overall higher efficiency with about 1 minute shorter scan time on average than NAV. The reviewer scores of right middle-distal renal arteries were significantly higher with ADIOS than those with NAV (p=0.006). Similarly, maximal visible vessel length was found 0.35 cm longer on average in right kidneys with ADIOS than that with NAV (p = 0.012). These improvements were mainly due to the lack of saturation with ADIOS as no significant difference was found in the left kidneys. Although rSNR, CNR and vessel sharpness were on average better in ADIOS than NAV, statistical significance was not shown. In Group A, where the scan times of both ADIOS and NAV were similar, the performance of the two gating methods was very similar, with none of the measures significantly different. In Group B, NAV performed worse than ADIOS although it used about two more minutes on average than ADIOS. ADIOS provided significantly higher vessel sharpness than NAV (p=0.01). ADIOS was also superior to NAV in the maximal visible vessel length measurements and the reviewer scores of middle-distal arteries.

Table 3.1 Image quality comparison between ADIOS and NAV at proximal-middle portion of renal arteries (main renal arteries and extra-parenchyma branches)

	rSNR	rCNR	Reviewer score**		Vessel sharpness (mm^{-1})
			L	R	
ADIOS (A*)	44.9±6.9	31.0±6.0	4.44±0.50	4.63±0.48	0.88±0.13
NAV (A*)	44.5±4.5	31.2±8.7	4.44±0.50	4.38±0.70	0.87±0.11
Paired diff.	0.4±4.2	0.1±3.6	0	0.25±0.66	0.01±0.06
p value	0.78	0.94	1	0.35	0.70
ADIOS (B*)	38.3±2.9	28.1±3.7	4.33±0.75	4.50±0.76	**0.90±0.08**
NAV (B*)	34.7±7.4	24.5±7.1	4.50±0.76	4.50±0.76	**0.85±0.07**
Paired diff.	3.5±4.3	3.6±4.6	-0.17±0.37	0	**0.05±0.03**
p value	0.13	0.14	0.36	1	**0.01**
ADIOS (T*)	42.3±6.5	29.9±5.4	4.40±0.61	4.57±0.62	0.89±0.11
NAV (T*)	40.6±9.2	28.3±6.9	4.46±0.62	4.43±0.73	0.87±0.09
Paired diff.	1.7±4.5	1.5±4.4	-0.07±0.25	0.14±0.52	0.02±0.05
p value	0.19	0.22	0.33	0.34	0.14

rSNR = relative signal-to-noise ratio; rCNR = relative contrast-to-noise ratio.
ADIOS = adaptive online self-gating; NAV = diaphragm navigator.
* A = Group A; B = Group B; T = Total (Group T).
** Based on five-point scale (from 1 = non-diagnostic to 5 = excellent).

Table 3.2 Image quality comparison between ADIOS and NAV at middle-distal portion of renal arteries (intra-parenchyma branches)

	Reviewer score**		MVVL (cm)		Scan time (min’sec”)
	L	R	L	R	
ADIOS(A*)	4.00±0.82	4.25±0.66	7.71±0.66	8.66±0.82	5’37”±1’8”
NAV (A*)	3.89±0.87	3.88±0.93	7.91±0.61	8.34±0.58	5’43”±1’6”
Paired diff.	0.11±0.31	0.37±0.48	-0.20±0.41	0.32±0.44	-6”±23”
p value	0.35	0.080	0.20	0.092	0.46
ADIOS(B*)	4.00±0.82	**3.83±0.69**	**8.07±0.82**	8.40±0.89	**5’1”±1’15”**
NAV (B*)	3.83±1.07	**3.00±1.00**	**7.88±0.79**	8.01±0.10	**7’19”±1’20”**
Paired diff.	0.17±0.37	**0.83±0.69**	**0.20±0.15**	0.39±0.43	**-2’18”±52”**
p value	0.36	**0.042**	**0.034**	0.097	**0.002**
ADIOS(T*)	4.00±0.82	**4.07±0.70**	7.85±0.75	**8.55±0.86**	**5’22”±1’13”**
NAV (T*)	3.87±0.96	**3.50±1.05**	7.89±0.69	**8.20±0.80**	**6’21”±1’26”**
Paired diff.	0.13±0.34	**0.57±0.62**	-0.04±0.39	**0.35±0.43**	**-59”±1’15”**
p value	0.16	**0.006**	0.69	**0.012**	**0.010**

MVVL = maximal visible vessel length.
ADIOS = adaptive online self-gating; NAV = diaphragm navigator.
* A = Group A; B = Group B; T = Total (Group T).
** Based on five-point scale (from 1 = non-diagnostic to 5 = excellent).

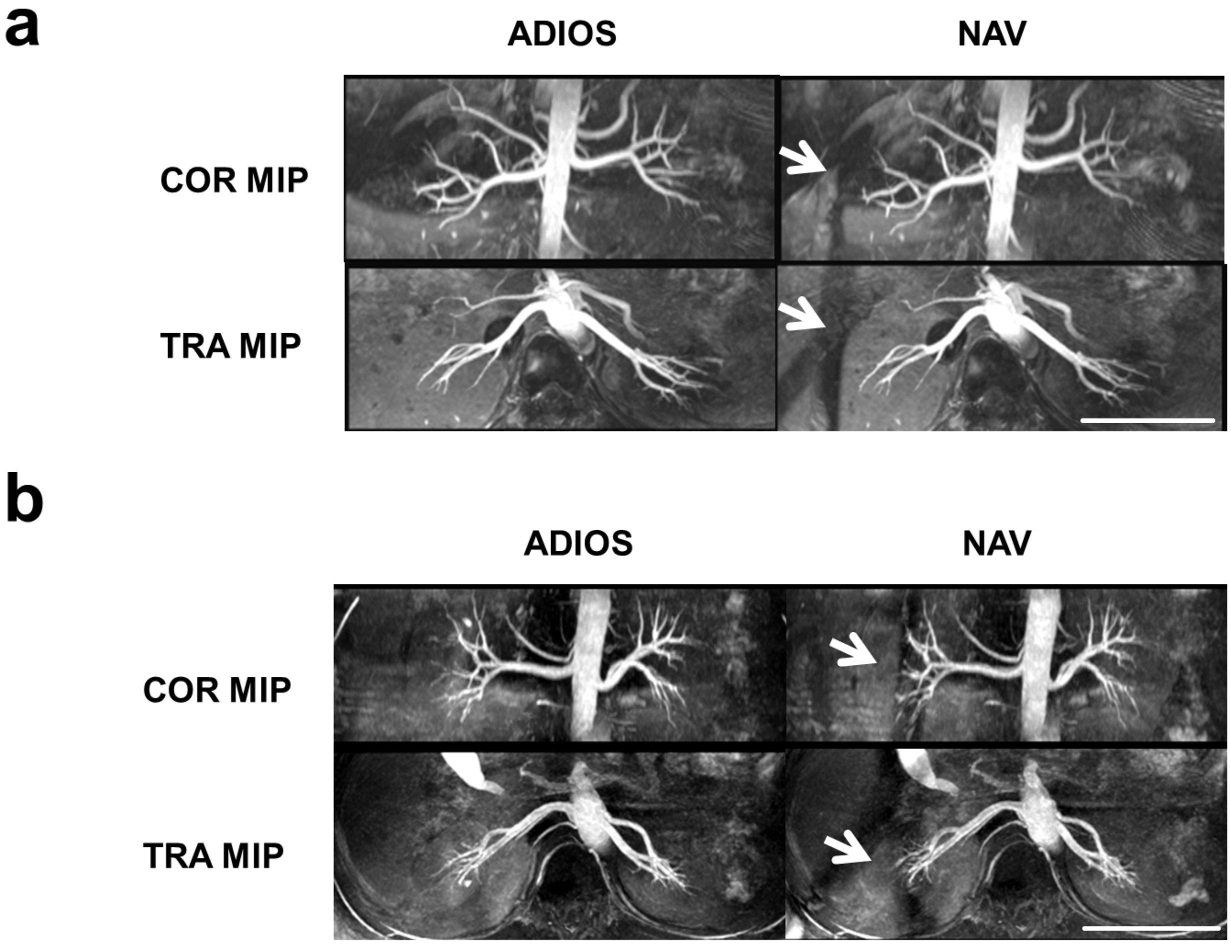

Figure 3.3 Representative coronal (COR) and transverse (TRA) maximal intensity projection (MIP) images from two healthy subjects comparing image quality of ADIOS and conventional diaphragm navigator gating (NAV), both acquired with spatial resolution of 1.1×1.1×2.2 mm3 and TR of two heartbeats. Scale bars represent 10 cm. Note the saturation bands caused by NAV (arrows in a, b). In some cases, NAV saturation bands degraded the visualization of distal right renal arteries (arrows in b), whereas in the ADIOS images there was no such effect.

3.4 DISCUSSION

In this study we have shown the feasibility of applying a real-time self-gating technique (ADIOS) to enable free-breathing renal bSSFP NC MRA without the use of diaphragm navigator (NAV) or abdominal bellows. Preliminary results of ADIOS from healthy volunteers have demonstrated similar image quality in the proximal-middle portion of renal arteries, significantly improved middle-distal vessel visualization in the right kidneys, and shorter scan time compared to conventional NAV gated acquisition. Replacing conventional NAV with SG has several benefits for the clinical usage of abdominal NC MRA. First, it eliminates the saturation bands caused by cross-pair navigator excitation which causes signal loss in region-of-interest (e.g. renal arteries) in certain patients. Second, it no longer requires additional NAV setup and scouting, reducing the overall patient time with simplified imaging planning and less required operator expertise. In this study, the typical time needed to setup NAV was 2 to 3 minutes including scout scans, window adjustments, etc., and it may go up to 7 minutes if the NAV signal was suboptimal on the first try. Third, in contrast to NAV, SG is based on the motion information derived directly from the slab being imaged, therefore may be a better indicator of motion *in situ* rather than the correlated diaphragm displacement. SG signal may also have more reliable SNR than NAV signal which originates from relatively remote anatomy.

A fast automatic online gating algorithm for SG is designed in this work to minimize overall motion artifacts by trading-off between gating efficiency and residual motion within the acceptance window. It adaptively regulates the gating to compensate for respiratory signal drift and maintains a relatively defined scan time, avoiding prolonged acquisition and associated breathing pattern change and/or bulk movement. As a result of the adaptive algorithm, total scan time of ADIOS was on average 15% (59 seconds) shorter than that of NAV with no apparent penalty on image quality in terms of motion artifacts. In the grouped sub-analysis, NAV acquisitions that had long scan time (about 2 minutes longer than that of ADIOS on average) performed worse than ADIOS. In those cases, long scan time and its associated signal drift and/or motion were the most possible culprit for the inferior image quality with NAV. ADIOS alleviated this problem to certain extent with its adaptive gating scheme. With its adaptability ADIOS may potentially provide better image quality and diagnosis in patients who have difficulties holding still during prolonged scan.

There are limitations in the implementation of self-gating in this work. First, a short (2 heartbeats) breath-hold is needed for acquiring an end-respiratory reference projection. This reference is not necessarily ideal for end-expiration phase during free-breathing because of possible mismatch between free-breathing and breath-hold even at the same respiratory phase. This limitation can be resolved in future work by utilizing other analysis of the SG projections to extract physical translational information, such as template shifting [41], to eliminate the need for a breath-hold reference projection. Second, residual respiratory motion within the accepted data was not corrected. The main focus of this work was to demonstrate the feasibility of a real-time SG technique to facilitate the clinical usage of NC MRA. Therefore motion correction technique that requires additional post-processing was not used. However, in future work it is possible to incorporate motion correction techniques that are typically performed offline [42] into the online image reconstruction process.

Lastly, the online self-gating technique developed in this work is not specific to bSSFP-based renal NC MRA. It is a general free-breathing approach that can be applied for other sequences and/or other organs for respiratory motion compensation. The adaptive gating algorithm provides some flexibility for designing other SG applications. If necessary, projections in multiple directions may be used to more accurately compensate for 3D translational motion.

3.5 CONCLUSION

In conclusion, we have developed an online self-gating technique for free-breathing renal NC MRA that offers no-setup respiratory gating, shorter scan time, and improved distal vessel visualization compared to conventional diaphragm NAV.

CHAPTER 4: HIGH RESOLUTION DIFFUSION IMAGING OF CAROTID VESSEL WALL

4.1 BACKGROUND

Stroke is a major worldwide health problem - every year it accounts for the death of an estimated 5 million people and leaves another 5 million permanently disabled [43]. Carotid artery atherosclerosis is a major cause of stroke and its subsequent disability and mortality [44]. Atherosclerotic plaques may cause stenosis of the arterial lumen resulting impaired cerebral perfusion. However, as a chronic and progressive disease, atherosclerosis remains asymptomatic in the majority of people due to the outward (positive) remodeling of the vessel wall. Therefore the degree of luminal stenosis alone is a relatively poor indicator of cerebral events [4, 45]. Plaque disruption and rupture are believed to be more common etiology of cerebral ischemia and it is now widely accepted that greater emphasis should be placed on plaque composition characterization to determine its vulnerability [6, 46]. Several histological studies from carotid endarterectomy specimens suggest that a typical culprit carotid plaque has a large lipid-rich necrotic core (LRNC), also known as “lipid core”, with a thin over-lying fibrous cap [6, 47]. When the integrity of the fibrous cap is compromised, the lipid core is exposed to the blood-stream and thrombus formation and subsequent cerebral embolization may occur.

High-resolution multiple-contrast weighted MRI has been used together with contrast enhancement (CE) to identify different plaque components with good histology correlation [48, 49]. Gadolinium-based contrast media can preferentially enhance the fibrous cap providing the distinction from the LRNC, providing more accurate characterization than noncontrast T1- and T2-weighted imaging. Because MRI is noninvasive and does not involve ionizing radiation, it can be used clinically to monitor the progression of atherosclerotic disease and the outcome of therapeutic interventions [50]. However, several epidemiology studies have shown the association between atherosclerosis and chronic renal disease and many atherosclerosis patients have concomitant impaired renal function [51, 52]. This makes the usage of CE MRI highly undesirable due to the increased risk of gadolinium-associated nephrogenic systemic fibrosis [53]. Moreover, the added cost and procedural complexity of CE reduces the appeal of MRI as a potential tool for disease screening in large population and longitudinal evaluation of therapeutics.

As a noncontrast alternative, diffusion-weighed imaging (DWI) with apparent diffusion coefficient (ADC) mapping has showed great promises for carotid plaque characterization, with excellent image contrast for discriminating the LRNC from the surrounding fibrous tissue. For example Qiao et al reported that DWI can selectively identify LRNC with high contrast and accuracy, whereas conventional T1- and T2-weighted images, by comparison, do not accurately identify LRNC [54]. Clarke et al compared eight MR contrast weightings including T1w, T2w, PDw etc., and found diffusion weighting was the only image contrast in which the signal standard deviation for LRNC and fibrous tissue did not overlap [55]. Two other groups applied DWI in vivo and achieved good correlation with histology for the detection of LRNC [56, 57].

However, to our knowledge, all in vivo DWI studies so far were based on 2D single-shot diffusion-weighted echo-planar imaging (SS-DWEPI). It is a time-efficient sequence and available on all major commercial systems, yet is known to suffer from suboptimal image quality with susceptibility-induced image distortion, dropout, blurring, and signal loss. In carotid imaging applications, the air/tissue and bone/tissue interfaces around the cervical spine region have large susceptibility differences therefore are especially challenging for SS-DWEPI acquisitions. Moreover, SS-DWEPI provides very limited spatial resolution (typical in-plane pixel size ≥1.0x1.0 mm^2). Attempts to increase spatial resolution will further deteriorate image quality with more T2* decay during the course of SS-DWEPI. When imaging fine anatomy such as atherosclerotic plaques, where the regions-of-interest (ROIs) typically contains only a few pixels, conventional SS-DWEPI will likely cause severe partial volume effects and inaccuracies in plaque ADC measurements [54, 58].

The purpose of this work is to develop a novel DWI method for noncontrast carotid plaque characterization that provides three major improvements over current 2D SS-DWEPI: (1) 3D imaging capability; (2) high spatial resolution (0.6x0.6x2 mm3); and (3) reliable image quality.

4.2 METHODS

4.2.1 Pulse Sequence Design

The MR pulse sequence development contains the design and implementation of two major parts: a motion-compensated diffusion preparation module and a reduced field-of-view (rFOV) 3D turbo spin echo (TSE) readout (**Figure 4.1**). The diffusion preparation module was implemented based on a driven equilibrium (DE) preparation [59, 60], of which the variants are commonly used in dark-blood imaging [61, 62]. Bipolar diffusion sensitizing gradients were used to compensate for 1st-order motion and to reduce eddy currents. Additional specifications of the preparation module are included in Table 1. Acquisitions of different diffusion weightings were interleaved in order to minimize the mismatch between images. Pulse-triggering was utilized to synchronize the sequence to each subject's cardiac rhythm in order to minimize arterial pulsatile motion. Imaging readout was implemented based on a 3D TSE kernel for reliable image quality at 3T and high SNR. Reduced field-of-view was developed to reduce scan time with inner-volume refocusing pulses [63]: gradients of the refocusing pulses in TSE were moved from the slice-encoding direction to the phase-encoding direction, with their magnitude modified accordingly based on the desired rFOV size. Arterial blood suppression scheme was designed with a combination of double inversion recovery (DIR) and flow-sensitive dephasing (FSD) [64] in order to effectively suppress flow artifacts, improve vessel wall visualization and reduce partial volume effect.

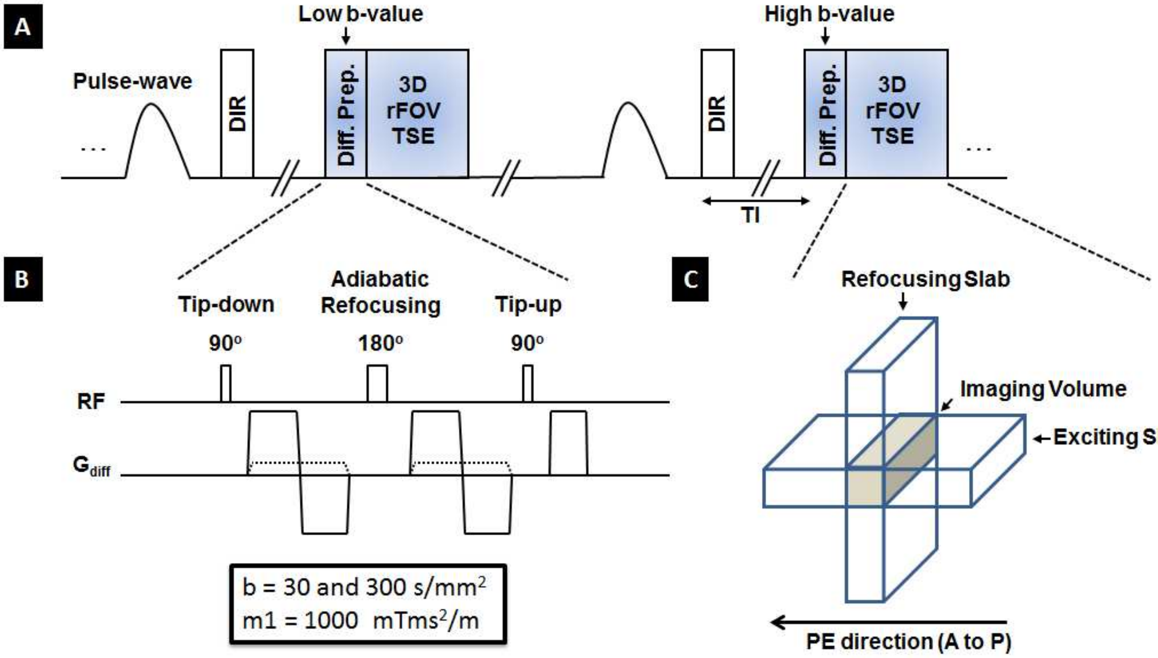

Figure 4.1 Imaging sequence design of black-blood DP-TSE with rFOV. (A) The pulse-triggered data acquisition scheme consists of a black-blood (DIR) preparation module, a diffusion-preparation module, and a segmented 3D TSE kernel with reduced field-of-view. Two diffusion-weighted images were acquired in an interleaved fashion to minimize the mismatch between them. (B) Diffusion preparation module. A pair of bipolar gradients was used for diffusion encoding with complete compensation for first-order motion. Adiabatic refocussing pulse was used for its insensitivity to b1-inhomogeneity. In order to suppress residual arterial blood, additional flow-dephasing gradients were incorporated into the module with moderate first gradient moment of 1000 mTms2/m at both diffusion weightings. (C) Illustration of the reduced field-of-view scheme. Excitation slab is perpendicular to the slice direction whereas the refocussing slab was oriented to be perpendicular to the phase direction, limiting the imaging volume to the overlapping region between the two slabs (brown region). Because of the reduced imaging volume, phase encoding steps could be greatly reduced to shorten scan time.

4.2.2 In Vivo Imaging

With informed consent and approval from internal review board (IRB), healthy volunteers (n = 15; 5 M, 10 F; aged 23-48 y/o) and patients with diagnosed or suspected carotid atherosclerosis (n = 6; 4M, 2F; aged 58-81 y/o) were recruited and scanned on a 3T scanner (MAGNETOM Verio; Siemens AG, Erlangen, Germany) with a 4-channel carotid coil (Machnet BV, Roden, The Netherlands). Scanning parameters included 3D transverse slab of 12 slices with in-plane resolution of 0.6x0.6 mm^2 and slice thickness of 2 mm. Two diffusion weighted images with *b* values of 30 and 300 s/mm^2 were acquired in an interleaved fashion. FSD with first gradient moment of 1000 mTms^2/m was used for blood suppression in combination with conventional double inversion recovery (DIR) preparation. Other details of this protocol are summarized in Table 1.

Healthy volunteers were also scanned using conventional SS-DWEPI for comparison. Due to the limitations of SS-DWEPI, lower in-plane resolution (1.2x1.2 mm^2) were used along with 75% partial Fourier in the phase direction. Diffusion weightings of b = 50 and 300 s/mm^2 along the slice direction were acquired. Other parameters are also listed in Table 1. This protocol was adapted for the scanner based on previously published studies by other groups [57, 58].

Patients underwent additional clinical scans of pre-contrast T2-weighted imaging as well as pre- and post-contrast enhanced T1-weighted imaging as the reference using a conventional 2D TSE protocol similar to the ones described by previous studies [48, 49]. Common imaging parameters include: FOV = 160x160 mm^2;

in-plane resolution = 0.6x0.6 mm^2; slice thickness = 2.0 mm; and TR/TE = 720/9.4 (T1w), 4000/60 (T2w).

Table 4.1 Sequence parameters of DP-TSE and SS-DWEPI used in this study.

	DP-TSE	SS-DWEPI
Acquisition type	3D	2D
In-plane resolution (mm2)	0.6x0.6	1.2x1.2
Number of slices	12	12
Slice thickness (mm)	2.0	2.0
TR (s)	2RR	4.3
TE (ms, same for both b-value)	42 (effective)	75
Matrix	256x76	128x128
Partial Fourier	No	0.75
Field of view (mm)	160x47	160x160
ETL	12	N/A
BW (Hz/pixel)	130	1002
NEX	2	32
b value (s/mm2)	30/300	50/300
Fat suppression	CHESS	CHESS
Max diffusion grad. (mT/m)	43	Default (25)
Max FSD grad. (mT/m)	2.2	N/A
Diffusion grad. direction	All three axes	Slice
Scan time	~5’30”	5’24”

4.2.3 Image Processing and Evaluation

SNR, CNR and ADC measurement

Vessel wall SNR and CNR were evaluated using region of interest (ROI) analysis on both of the diffusion weighted images. Measurements were performed using image analysis toolbox in MATLAB (ver. 2011, Mathworks, Natick, MA). For each 3D volume, three image slices from the center to the peripheral of the slab were analyzed. ROIs of vessel wall and lumen from both sides of the carotid arteries were manually contoured and the signal intensities (S_{wall}, S_{lumen}) are recorded. Noise level (S_{noise}) was defined as standard deviation within ROIs drawn in peripheral air space of the image uncontaminated by artifacts. The relative vessel wall SNR and CNR were defined as:

$$\mathbf{SNR} = S_{wall} / S_{noise}; \qquad \mathbf{CNR} = (S_{wall} - S_{lumen}) / S_{noise}$$

ADC of normal carotid wall was calculated from the ADC map using similar ROI analysis. ADC of LRNC and fibrous plaque tissue in patients was measured based on the ROIs identified on the post-contrast enhanced T1-weighted image of the two types of tissue, respectively.

Wall visibility

Vessel wall visibility was quantified on both DP-TSE and SS-DWEPI images by three independent reviewers (ZF, CN and XB) who are blinded to the image type. Three DWI (300 s/mm^2) images at the level of common carotid arteries were evaluated from each subject. In total 90 common carotid vessel walls from the 15 healthy subjects were rated based on the fractions of vessel wall visible ranging from 0% to 100%. The vessel wall visibility grading was averaged among the reviewers and then classified to groups: less than 20% (not visible); 20%-50% (poor); 50%-75% (good); 75-95% (excellent); more than 95% (complete). A histogram was then generated of the counts of vessel walls with different levels of wall visibility for DP-TSE versus SS-DWEPI.

Wall thickness

In order to evaluate the partial volume effect, a computer assisted morphometric analysis of vessel wall was performed on a workstation using Image-Pro Premier (Media Cybernetics, Rockville, MD). This software performed semiautomatic tracing of the vessel wall inner and outer boundaries and calculated the distance between them, of which the mean was defined as wall thickness. Two common artery vessel walls were measured from each of the subjects on DP-TSE image, SS-DWEPI image, and conventional anatomical image (T2-weighted 2D TSE).

Statistical analysis

Seven slices with LRNC were identified in three patients using CE T1w images as the reference. ROIs of LRNC, fibrous plaque tissue and normal vessel were defined in CE T1w images and copied to DWI and ADC images for quantification. Slight translational adjustments of the ROIs were made in the cases where inter-scan movement was observed. In total, 265 pixels of LRNC, 289 pixels of fibrous plaque tissue, and 356 pixels of normal vessel wall from DP-TSE images were included in the calculation and the global mean and standard deviation of ADC values were computed. No normalization was used on ADC values between subjects and different tissue types. An unbalanced one-way ANOVA was performed on the mean ADC values of LRNC, fibrous plaque tissue, and adjacent normal vessel wall at each plaque location after verification of normality with quantile-quantile plot and Shapiro-Wilk test. Paired Student's t-tests were performed on the vessel wall visibility comparison and vessel wall thickness comparison between DP-TSE and SS-DWEPI. All statistical analysis was performed in R statistical programming language (ver. 3.0.3, The R Foundation for Statistical Computing, Vienna, Austria).

4.3 RESULTS

In each of the 21 subjects, the proposed DP-TSE method showed improved visualization of carotid vessel wall than SS-DWEPI, in which signal loss and distortion were commonly observed. The increase in spatial resolution and reduction of image artifacts, especially distortion, yielded markedly sharper vessel wall images in DP-TSE images. **Figure 4.2** shows a representative case of a healthy subject comparing the image quality of DP-TSE, on the left, versus SS-DWEPI, on the right, at two b-values and the resultant ADC maps. **Figure 4.2A** and **Figure 4.2B** are representative DP-TSE images of carotid vessel wall from healthy subjects at b = 30 and 300 s/mm^2, respectively. Arterial blood suppression was effective throughout the slices with clear visualization of vessel wall at both b-values. No visible susceptibility-induced artifacts were observed. ADC map at the corresponding slice showed clear, complete vessel wall (**Figure 4.2C**).

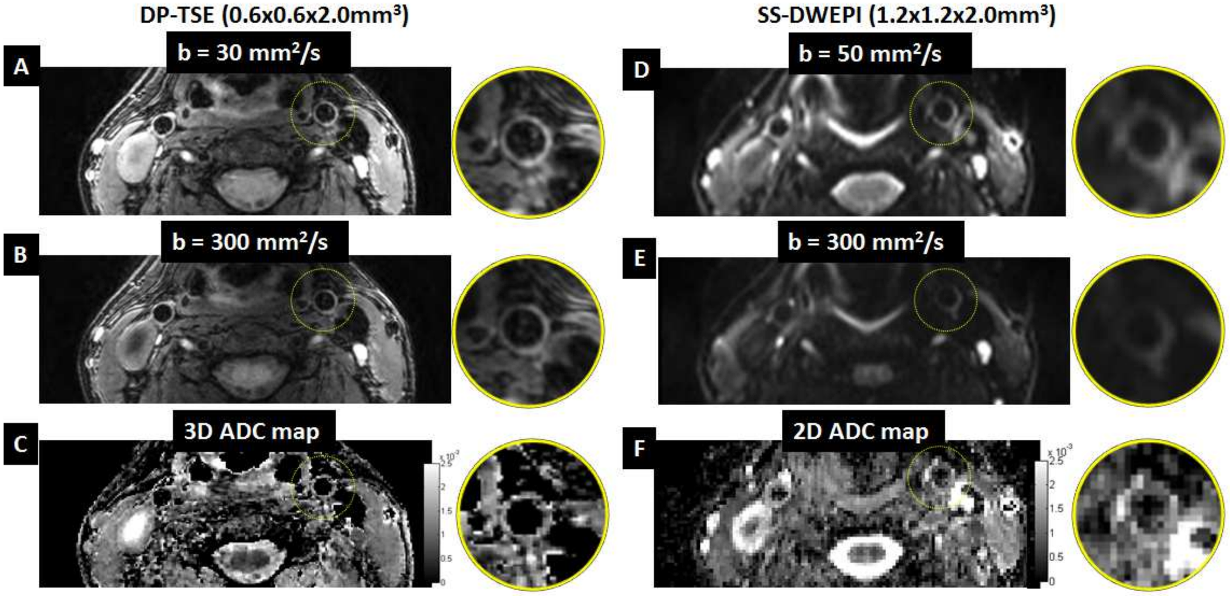

Figure 4.2 Representative image quality of 3D DP-TSE compared with that of conventional 2D SS-DWEPI from a healthy subject. (A to C) DWI of b = 30 mm2/s, DWI of b = 300 mm2/s and ADC map, respectively, acquired using DP-TSE with resolution of 0.6x0.6x2.0 mm3. (D to F) DWI of b = 50 mm2/s, DWI of b = 300 mm2/s and ADC map, respectively, acquired using SS-DWEPI with resolution of 1.2x1.2x2.0 mm3. Note that blurring, distortion and artifacts were present in the SS-DWEPI images compared with their counterparts from DP-TSE. Also note that SS-DWEPI images had higher T2 decay due to the longer required TE than that of the proposed DP-TSE.

There was no apparent signal loss due to motion in the DP-TSE images which suggested that 1st-order motion compensation was effective. **Figure 4.3** demonstrates the effects of motion compensation in the diffusion preparation with a representative case. At the same b-value, motion compensated preparation (**Figure 4.3A**) preserved the vessel wall signal well whereas the uncompensated preparation (**Figure 4.3B**) resulted in major loss of signal in the vessel wall due to the large first order gradient moment. A pulse wave-gated cine of the carotid vessel wall is presented to demonstrate the pulsatile motion in the carotid artery caused by arterial flow [see Additional file 1].

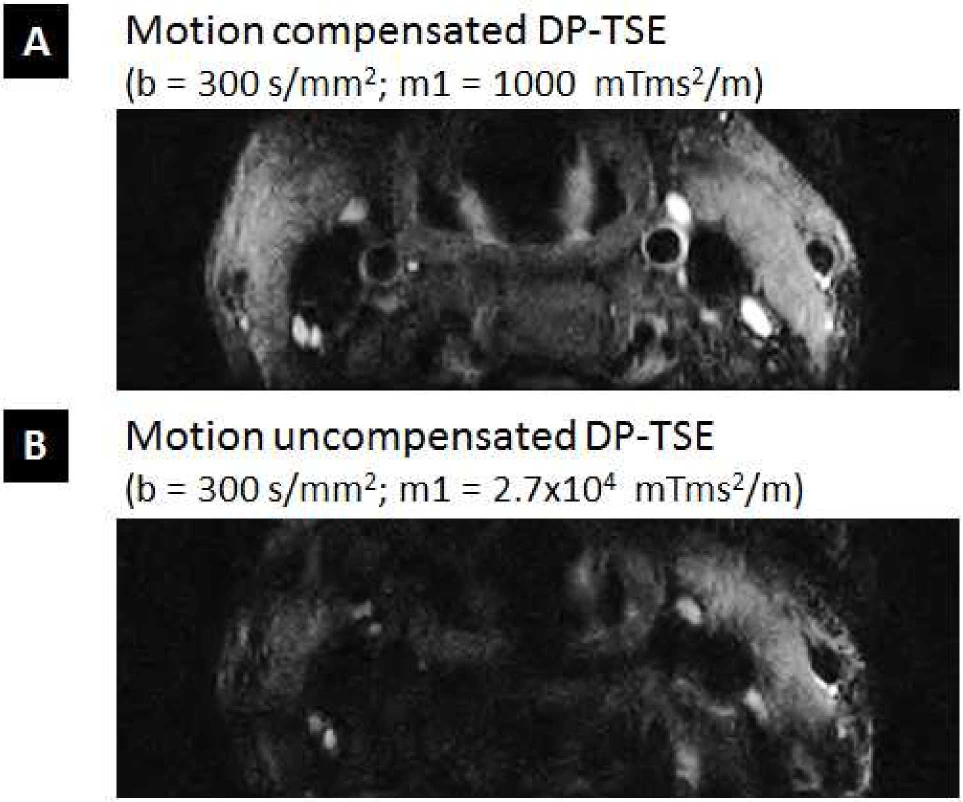

Motion compensated DP-TSE

($b = 300$ s/mm^2; $m1 = 1000$ mTms^2/m)

Motion uncompensated DP-TSE

($b = 300$ s/mm^2; $m1 = 2.7 \times 10^4$ mTms^2/m)

Figure 4.3 Effectiveness of motion compensation in diffusion preparation. At the same b-value, motion compensated preparation preserved the vessel wall signal well whereas the uncompensated preparation resulted in major loss of signal in the vessel wall due to the large first order gradient moment. A pulse wave-gated cine of the carotid vessel wall is presented [see Additional file 1] to demonstrate the pulsatile motion in the carotid artery.

Vessel wall visibility was significantly better with DP-TSE. **Figure 4.4A** shows representative images from DP-TSE and SS-DWEPI with different levels of visualization ranging from 0% to 100%. The histogram of the vessel wall visibility shows that the distribution of DP-TSE lied towards the higher end of the chart than that of SS-DWEPI

(**Figure 4.4B**). The average wall visibility of DP-TSE images was 84±15%, significantly higher than 41±28% of SS-DWEPI images ($p < 0.001$).

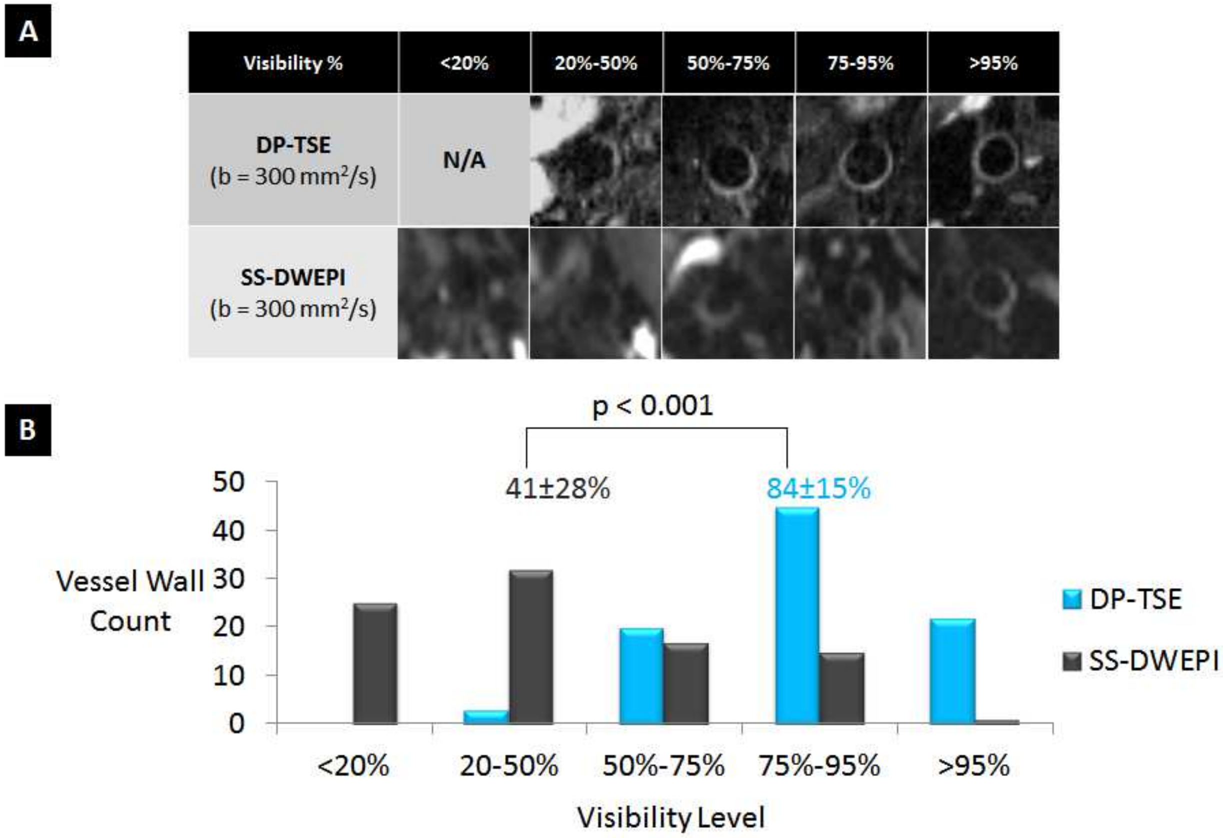

Figure 4.4 Vessel wall visibility comparison between 3D DP-TSE and conventional 2D SS-DWEPI. (A) Representative diffusion-weighted images from the DP-TSE and SS-DWEPI with different levels of visualization ranging from 0% to 100%. (B) Vessel wall visibility histograms of DP-TSE and SS-DWEPI. DP-TSE displayed a higher distribution and significantly higher average visibility than SS-DWEPI.

Vessel wall SNR and CNR quantified by ROI analysis was summarized in Table 2. Satisfactory vessel wall SNR provided further confirmation that there was no major signal loss due to motion. The vessel wall to lumen CNR suggested that the arterial blood suppression was effective.

DP-TSE provided more accurate wall thickness measurements than SS-DWEPI. **Figure 4.5B** shows that the mean vessel wall thickness measured from the proposed method was close to the reference anatomical images, which was 35% thinner than SS-DWEPI images ($p<0.001$) due to less image distortion and less partial volume effect.

The ADC measurement of carotid vessel wall in healthy subjects from this study was $1.53\pm0.23\times10^{-3}$ mm^2/s, which was comparable with previous in vivo and ex vivo studies (**Figure 4.6**).

Table 4.2 SNR, CNR measurements of carotid vessel walls in DP-TSE images.

Image Quantification	b = 30	b = 300
Mean SNR	14.9±2.8	11.6±2.1
Mean CNR	13.2±2.6	9.9±1.9

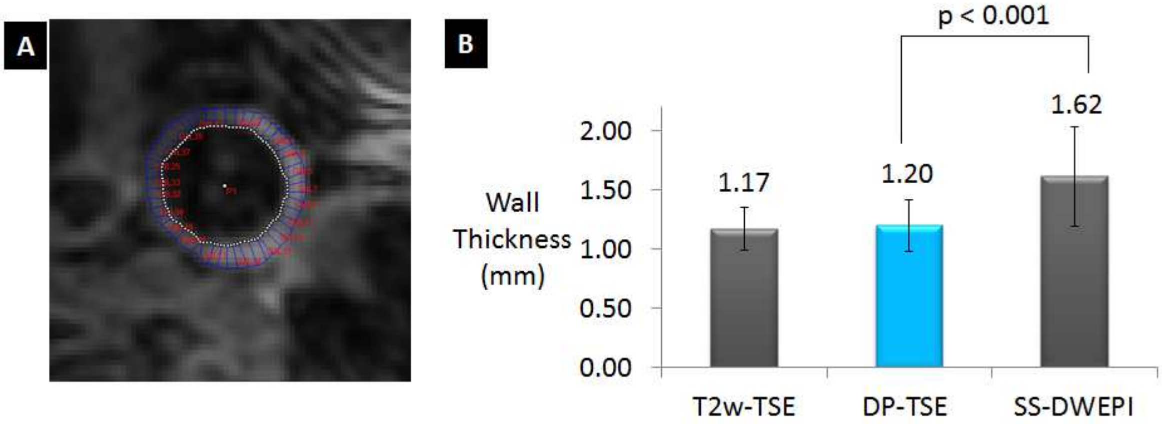

Figure 4.5 Computer-assisted morphometric measurements of vessel wall thickness. (A) Representative vessel wall thickness measurements on a DP-TSE image. Vessel wall inner and outer boundaries are traced and wall thicknesses are calculated along these traces using a semiautomatic program. (B) Vessel wall

thicknesses measured from DP-TSE were significantly thinner (35% on average) than those from the EPI images due to less distortion and partial volume effect.

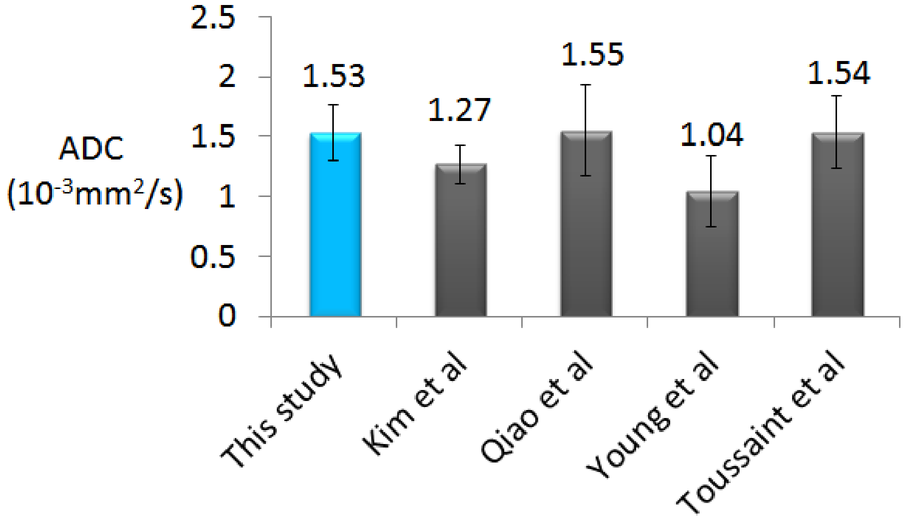

Figure 4.6 ADC measurements of normal carotid wall from 3D DP-TSE images. The value is comparable with previous in vivo (Kim, Young) and ex vivo (Qiao, Toussaint) studies.

Excellent agreement was observed between DP-TSE images (both DWI and ADC map) and conventional CE MRI in identifying LRNC. Two representative studies are presented in **Figures 4.7** and **Figures 4.8**. In both cases pre-contrast T1-weighted and T2-weighted TSE images provided little diagnostic information on the plaque composition. Post-contrast T1-weighted image showed a clear hypo-intense area within the plaque surrounded by enhanced fibrous plaque tissue, indicating LRNC. DWI (b = 300 s/mm^2) showed an area with reduced diffusion (hyper-intense) which matched to the area in the post-contrast T1-weighted image with low contrast uptake (hypo-intense). The resultant ADC map also confirmed that the area with low diffusion within the plaque was spatially matched to the LRNC region in the post-contrast T1-weighted image.

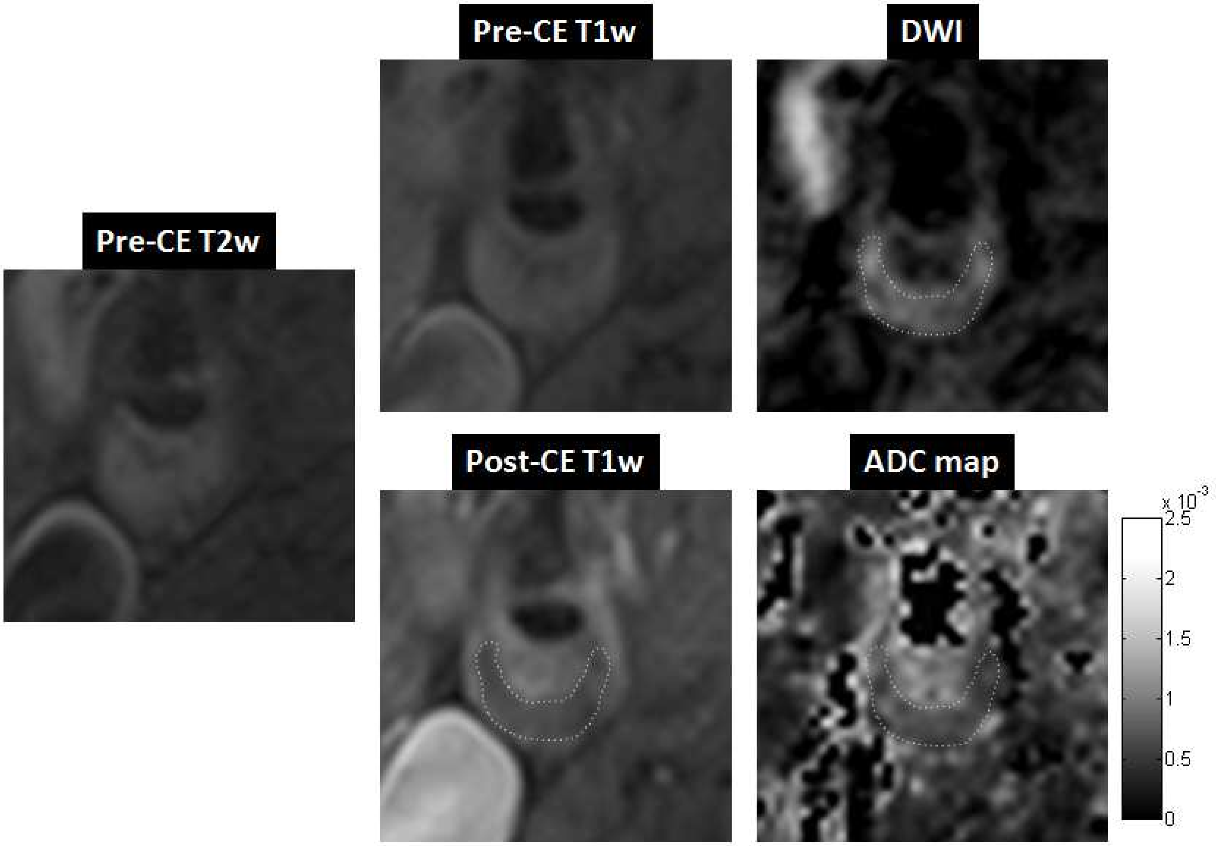

Figure 4.7 A case study of a symptomatic subject with an atherosclerotic plaque of 70% stenosis in the right internal carotid artery. Pre-contrast T2-weighted image showed slightly hyper-intense signal throughout the plaque area. Pre-contrast T1-weighted image was iso-intense in the plaque area. Post-contrast T1-weighted image showed a clear hypo-intense area within the plaque, a typical LRNC appearance, surrounded by enhanced fibrous plaque tissue. DWI (b = 300 mm2/s) using DP-TSE showed a hyper-intense region, i.e. low diffusion, that spatially matched to the LRNC area in the post-contrast T1-weighted image. ADC map showed an area with low diffusion (0.62±0.15x10-3mm2/s) within the plaque that spatially matched to the LRNC finding in the post-contrast T1-weighted image.

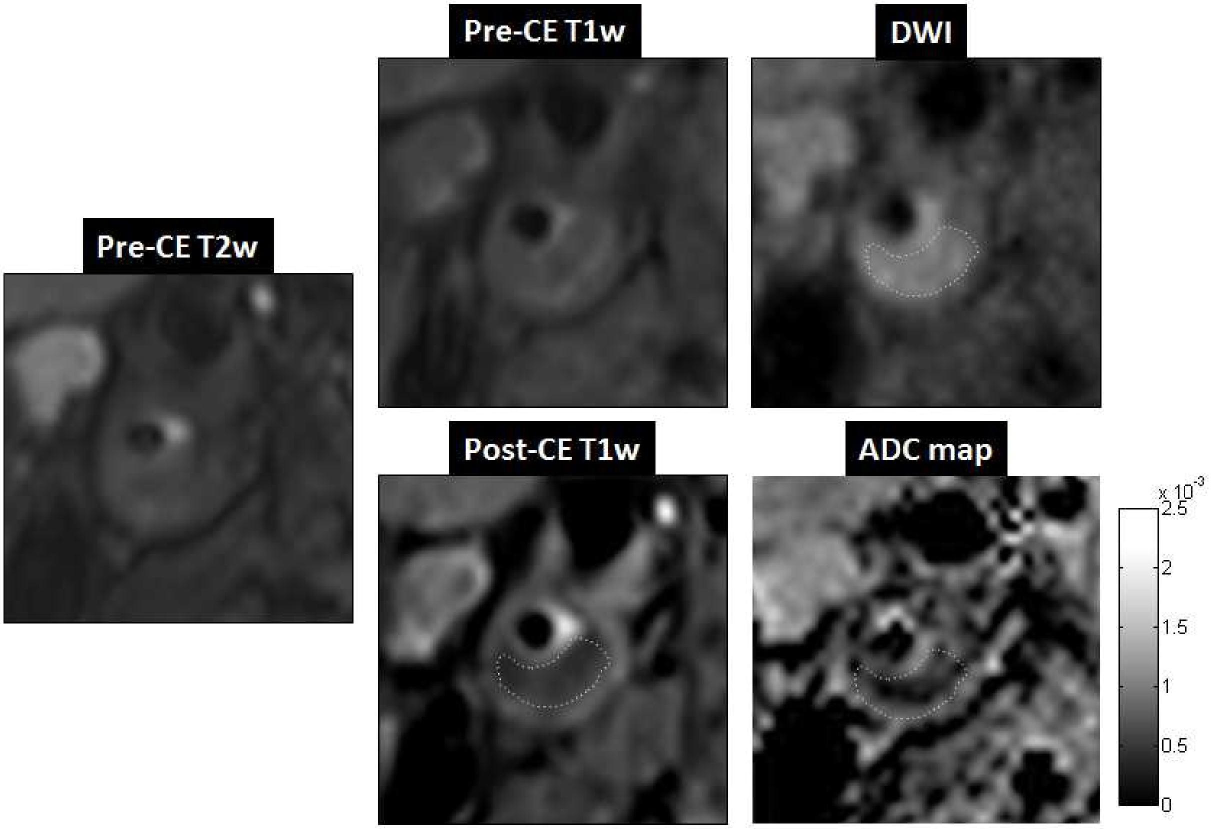

Figure 4.8 A case study of a symptomatic subject with an atherosclerotic plaque of 80% stenosis in the right internal carotid artery. Pre-contrast T2-weighted image and T1-weighted image were both iso-intense in the plaque area. Post-contrast T1-weighted TSE image showed a hypo-intense area within the plaque surrounded by enhanced tissue, indicating a large LRNC. DWI (b = 300 mm2/s) using DP-TSE shows a hyper-intense region, i.e. low diffusion, that spatially matched to the LRNC area in the post-contrast T1-weighted image. ADC map showed an area with low diffusion (0.46±0.22x10-3mm2/s) within the plaque that also spatially matched to the LRNC finding in the post-contrast T1-weighted image.

The ADC measurements in plaques based on region-of-interest analysis revealed markedly reduced apparent diffusion in LRNC compared with fibrous plaque tissue and normal vessel wall (**Figure 4.9**). The mean ADC of LRNC (265 voxels) was $0.60 \pm 0.16 \times 10^{-3}$ mm^2/s, whereas the mean ADC of fibrous plaque tissue (289 voxels) and normal vessel wall (356 voxels) was 1.27±0.29×10^{-3} mm^2/s and 1.42±0.38×10^{-3} mm^2/s, respectively. The one-way ANOVA showed significant difference between the mean values (F(2,20) = 79; p<0.01).

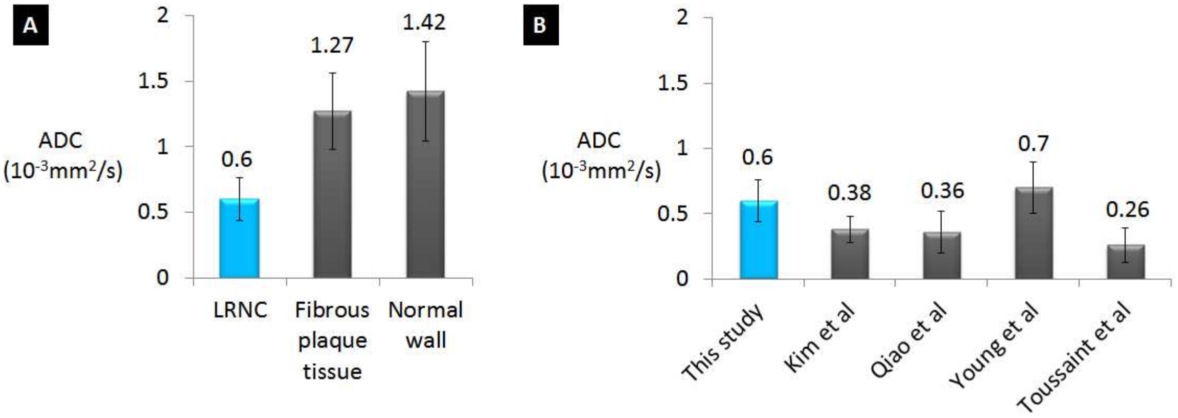

Figure 4.9 (A) The mean ADC measured from DP-TSE images in LRNC areas was significantly lower (0.60±0.16×10-3 mm2/s) than that of the fibrous plaque tissue (1.27±0.29×10-3 mm2/s) and normal wall tissue (1.42±0.38×10-3 mm2/s) with p<0.01. (B) The mean ADC of LRNC measured from DP-TSE images in this study compared with results from previous in vivo (Kim, Young) and ex vivo (Qiao, Toussaint) studies.

4.4 DISCUSSION

A 3D DP-TSE technique was developed for high-resolution DWI of the carotid artery wall. With comparable imaging time, the proposed method provided four-times better spatial resolution (0.6x0.6x2 mm^3 for DP-TSE vs 1.2x1.2x2 mm^3 for SS-DWEPI), markedly improved wall visibility, and more accurate wall thickness compared with SS-DWEPI in healthy volunteer studies. In contrast, signal loss and distortion were commonly seen in the conventional SS-DWEPI images, an observation consistent with the previous in vivo study by Kim et al [58]. In patient studies, excellent agreement was observed between DP-TSE and conventional CE MRI in identifying LRNC. ADC measurements in LRNC were significantly different from those of the fibrous plaque tissue and normal vessel wall.

DP-TSE allowed, for the first time, 3D DWI of the carotid arterial wall in vivo with sub-millimeter spatial resolution and excellent image quality on 3T. This was made feasible by the sequence design of a separated diffusion encoding module from the imaging readout, therefore enabling segmented acquisition. Unlike multi-shot EPI which is usually sensitive to phase errors [65], the separated driven-equilibrium diffusion preparation module tipped up the magnetization to the longitudinal axis and spoiled the residual transverse magnetization at the end of the preparation to eliminate phase dispersion. It was therefore less vulnerable to phase inconsistency between shots. Essentially, diffusion preparation only modulated the longitudinal magnetization to introduce diffusion-weighting. For the same reason, it did not violate the CPMG condition required by the following TSE readout kernel.

Imaging readout was developed based on TSE with reduced field-of-view. TSE is known to be relatively robust to field inhomogeneity [66], therefore adopted in this work for imaging carotid arteries at 3T. Inner-volume reduced field-of-view method was used to reduce phase encoding steps therefore shortening scan time. The disadvantage of rFOV is the SNR reduction associated with reduced imaging volume. However, even with rFOV, 3D TSE had approximately four-times the excited volume as conventional 2D TSE carotid imaging with comparable scan time.

The diffusion preparation design focused on two important aspects to cater to carotid vessel wall imaging: blood suppression and motion compensation. Effective arterial blood suppression (black-blood) was required to eliminate flow-induced artifacts commonly seen in carotid vessel wall imaging. Additionally, black-blood improved vessel wall visibility and eliminated blood pool partial volume effects at the blood/wall interface. In this study, the diffusion preparation and imaging readout were gated to the diastole in order to minimize the effects of motion. The slow flow in diastole and thick 3D imaging slab made black-blood imaging more challenging than conventional ungated 2D imaging. To address this, black-blood was achieved using the synergy of DIR and FSD [64]. DIR was utilized prior to the diffusion preparation when faster systolic inflow occurs. FSD is integrated into the non-selective diffusion preparation to dephase the residual blood spins throughout the imaging slab, therefore relaxing the requirement of complete inflow on DIR. Bipolar diffusion encoding gradients were used in all three directions to null the first order gradient moment, making the preparation relatively insensitive to motion. Additional FSD gradients were applied only in the slice direction, where flow was at its maximum and pulsatile motion was at its minimum [67].

ADC measurements of the healthy carotid vessel wall, LRNC, and fibrous plaque tissue in this study were comparable with those reported in previous in vivo and ex vivo studies [54, 56, 57, 68]. This provided preliminary support for the proposed new DWI method. However further validation is mandatory due to the limited magnitude of the patient study and the lack of histology in this technical work. With the indications from these preliminary results, double-blinded readings of DWI and CE MRI shall be performed and compared with histological results independently in a larger patient population in the future.

As a quantitative biomarker, ADC could potentially provide a more objective measure of the plaque lipid content. Young et al have shown that ADC can demonstrate not only the presence of lipid but also the amount [57]. ADC may serve as a surrogate marker for longitudinal studies evaluating the effectiveness of lipid-lowering therapies and other medical treatments. As a similar observation we noticed in this study that the mean ADC from atherosclerosis patients was lower than that from healthy subjects even for normal vessel wall. We hypothesize that even with no visible plaque, the ‘normal wall’ in patients may have lipid infiltration that caused the reduction of ADC. However it is important to note that although significantly lower ADC values have been observed in LRNC, the reference ADC ranges for healthy wall and LRNC in vivo have not been established. The limited resolution and image quality issues with conventional SS-DWEPI have been a major obstacle and the proposed method may serve as a step towards more accurate plaque diffusion quantification. Lastly, carotid plaque characteristics reflect generalized atherosclerosis [69] and the composition of carotid plaques determined by DWI may reveal the vulnerability of atherosclerotic plaques elsewhere.

4.5 CONCLUSIONS

DP-TSE is a promising method for 3D diffusion imaging of carotid vessel wall with high spatial resolution and improved image quality over SS-DWEPI. It provides a potential means to detect LRNC in carotid plaque in vivo without the use of gadolinium-based contrast media, allowing carotid plaque characterization in patients with renal insufficiency.

CHAPTER 5: SIMULTANEOUS BLACK-BLOOD IMAGING OF CAROTID AND INTRACRANIAL VESSEL WALL

5.1 INTRODUCTION

Stroke is a global health concern and majority of stroke cases are ischemic stroke. The major underlying cause of ischemic stroke is atherosclerosis. MRI is one of the most promising noninvasive modalities for vessel wall imaging [44]. Unlike CT and ultrasound, MRI can provide excellent tissue contrast for directly assessing vessel wall in addition to angiographic images for evaluating luminal stenosis. This advantage became more desirable in light of recent evidences showing that stenosis alone is a poor predictor for cerebral events as significant luminal narrowing may be absent in patients with severe atherosclerosis owing to arterial remodeling [44, 70]. In addition, direct imaging of the blood vessel wall offers the potential to discriminate between different vascular pathologies with similar luminal defects therefore helping determine the optimal treatment [4].

Atherosclerosis is a systematic disease that usually affects multiple vascular beds and diseases in extracranial and intracranial arteries are both commonly associated with ischemic stroke [71]. An ideal imaging protocol therefore should cover all of the frequently affected locations including common carotid artery bifurcation, the siphon, the 1st segment of the middle cerebral artery (M1), 1st and 4th segments of the vertebral artery (V1, V4) and the 1st segment of the basilar artery (BA) [72]. The conventional extracranial carotid vessel wall imaging is based on multi-slice 2D TSE

[19]. However, applying this technique to intracranial vessels may lead to inaccuracy due to their small size and tortuous course [73]. Recently 3D variable-flip-angle TSE (SPACE for Siemens, VISTA for Philips, and CUBE for GE) emerged as a promising technique for extracranial carotid [64] and intracranial [74] vessel wall that provides several advantages over its 2D counterpart: 1) higher resolution especially in the slice direction, potentially isotropic; 2) larger anatomical coverage with coronal acquisition; 3) capability of retrospective reformatting with arbitrary slice orientation and thickness. However current SPACE protocols typically focuses on a single station and using multiple scans to cover all frequently affected vascular locations is time-consuming and infeasible for certain patients.

Successful vessel wall imaging requires complete suppression of luminal blood, i.e. black-blood (BB) imaging, to provide a good vessel wall to lumen contrast for assessing vessel wall pathology [75]. Commonly used BB techniques such as double inversion recovery (DIR) [76] are more difficult to work with large FOV 3D acquisitions due to larger outflow volume. Despite inherent black-blood effects by SPACE, residual blood signal is often observed in carotid artery which could be mistaken as plaque. Blood suppression in intracranial vessels may be more challenging due to slower flow. To address these issues, additional BB techniques such as flow-sensitive dephasing (MSDE) have been attempted in SPACE imaging, however, with unwanted T2 signal decay [64, 77]. The use of gadolinium contrast agent for enhancing plaque components (fibrous cap, inflammation etc.) makes post-contrast blood suppression more difficult due to shortened blood T1. Recently a new BB technique using Delay Alternating with

Nutation for Tailored Excitation (DANTE) pulse train has been used in gradient echo sequences providing good suppression of slow flow, less signal loss, and less T2 weighting than MSDE preparation [78]. We hypothesize that the combination of slow-flow suppression by DANTE preparation and inherent BB effects by SPACE may be a solution for post-contrast vessel wall imaging.

Based on the aforementioned considerations, the goal of this study is to develop a time-efficient 3D combined carotid and intracranial vessel wall imaging protocol with high isotropic resolution that: 1) covers all frequently affected vascular locations in a single scan; and 2) suppresses blood effectively both pre- and post-contrast.

5.2 METHODS

5.2.1 Theoretical and Technical Considerations

SPACE is a variant of 3D TSE that significantly improves k-space sampling efficiency with longer echo train duration and shorter echo spacing. The use of longer echo train duration is enabled by using variable flip angle refocusing pulse train that compensates for T2 decay. Additionally echo spacing is reduced by the use of nonselective refocusing pulses. Satisfactory T1-weighting (or PD-weighting) can be achieved with carefully designed reordering which enables the central part of k-space to be sampled at the beginning of the echo train.

SPACE has inherent flow suppression properties that are primarily based on two mechanisms: 1) Gradient moments induced intravoxel dephasing. Flowing blood spins within a voxel has a range of velocities and accelerations that will result in a widespread of phase dispersion leading to signal cancellation under the influence of uncompensated gradient moments during each echo train. This is less effective when the flow is not parallel to the readout direction, of which the gradient moments are typically much higher than those in the other two directions [79]. 2) Stimulated echo induced intravoxel dephasing. The non-180 variable flip angle refocussing pulses used in SPACE introduce various stimulated echoes that go through different coherence pathways than corresponding spin echoes leading to further dephasing of moving spins.

DANTE suppresses signal of moving spins through a different mechanism than SPACE. DANTE consists of a series of low flip angle nonselective pulses interleaved with gradient pulses with short repetition times which drive static spin systems into a steady-state. Flowing spins cannot establish such steady state due to the spoiling effect caused by the applied gradient and the velocity variations throughout the pulse train. This attenuation effect is insensitive to flow rate as long as it is above 0.1 cm/s, whereas static tissue signal can be largely preserved by the use of small flip angle pulses [80].

The combination of DANTE and SPACE may be complementary for suppressing flow especially in the context of post-CE imaging: 1) Flow suppression in SPACE is directional as the effect is greatest in the readout direction. Therefore it is often under-utilized due to the fact that readout direction is largely limited by anatomical coverage and the course of blood vessels is naturally tortuous (e.g., carotid and intracranial vessels). DANTE can supplement SPACE by applying gradient pulses in the phase encoding directions where its flow suppression is insufficient. 2) DANTE can help suppress slow flow for which SPACE does not generate enough intravoxel phase dispersion. 3) Post-CE the T1 of blood is much shortened (e.g. <150ms) leading to fast recovery of blood signal. Thus even if DANTE can suppress blood completely, its effect will not sustain throughout the readout period (e.g. >150ms). SPACE generates intravoxel dephasing throughout its echo train thus can help maintain the black-blood effect.

The sequence diagram of DANTE-SPACE is shown in **Figure 5.1**, consisting of a DANTE preparation module, an optional anti-aliasing regional saturation module (R-sat) and a fat saturation module (F-sat) played out immediately before SPACE readout module.

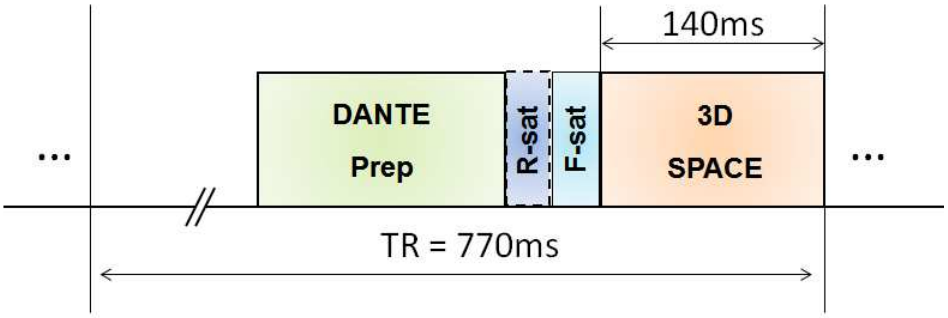

Figure 5.1 Sequence diagram of DANTE-SPACE. A DANTE preparation module, an optional anti-aliasing regional saturation module (R-sat) and a fat saturation module (F-sat) are played out immediately before SPACE readout module. DANTE preparation module consists of a series of small flip-angle RF pulses interleaved with dephasing gradients as described by Li et al [80]. DANTE module is played out immediately before F-sat when R-sat is not needed. DANTE parameters include: flip angle = 10°, phase increment = 0°, number of pulses = 100; inter-pulse repeat time= 1ms; Gxyz = 25mT/m.

5.2.2 Numerical Simulations and Phantom Study

Bloch equation simulations were performed to investigate the effects of DANTE module on SPACE images in terms of image contrast. Using the approximation of nonflowing magnetization as described by Li et al. in [80], a range of T1 (400~1550ms) and T2 (20~300ms) values relevant to plaque tissue types were simulated. The relative signal differences between DANTE-SPACE and SPACE were quantified. In addition, contrast ratios of different plaque tissue types including normal wall, recent hemorrhage, lipid core and fibrous tissue were calculated and compared between DANTE-SPACE and SPACE. Reference signal intensity was based on skeletal muscle, a commonly used reference for identifying carotid plaque components [81]. Relaxation parameters (T1, T2 in msec) were assumed for normal wall (1115, 54), recent hemorrhage (500, 107), lipid core (720, 37), fibrous tissue (1006, 56), fibrous tissue after CE (600, 40), and skeletal muscle (1412, 50) based on literature values [82, 83]. Different combinations of DANTE parameters including flip angle, echo train length, and echo spacing were tested. Other imaging parameters were kept identical as the following in vivo studies. Coding and visualization were written in MATLAB (The Mathworks, Inc, Natick, MA; version 2010b).

A phantom was constructed to evaluate the contrast variations. It consists of eight test tubes containing deionized water doped with different concentrations of gadolinium submerged in a cylindrical water tank. It was scanned using DANTE-SPACE, SPACE, and T1w 2D TSE. Different combinations of DANTE parameters including flip angle (5° to 10°), echo train length (90 to 200), and echo spacing (0.5ms or

1ms) were tested. The resultant images were normalized and signal intensities were measured from each test tube. In comparison, intraclass correlation coefficient (ICC) and mean square error (MSE) were calculated between DANTE-SPACE and SPACE, as well as between DANTE-SPACE and 2D TSE, respectively.

5.2.3 Healthy Subject and Patient Studies

Study population

The study was approved by institutional review board. Fourteen healthy volunteers (8 males, 6 females; age range 23-60, mean 37) with no history of carotid or intracranial vascular disease and six patients (4 males, 2 females; age range 37-85, mean 60) with known carotid and/or intracranial stenosis based on previous MRA or CTA were consecutively recruited for the study. Informed consent was obtained from all study participants.

System and coil configuration

All studies were performed on a clinical 3T MR system (MAGNETOM Verio; Siemens AG Healthcare, Erlangen, Germany). The scanner's integrated body coil was used for RF transmission. Due to coil availability, a 12-channel integrated head/neck coil was used together with a 4-channel bilateral special purpose surface coil on the healthy subjects, whereas the same head/neck coil was used together with a 4-channel phased-array carotid coil (Machinet BV, Elde, The Netherlands) on the patients.

Imaging protocol

Standard triple-plane localizers were followed by a 3D time-of-flight (TOF) MRA for localizing carotid and intracranial arteries. As shown in **Figure 5.2A**, TOF covers the vasculature in the entire neck and part of brain up till the level of corpus callosum with multiple transverse slabs. Maximum intensity projection (MIP) images of TOF were then used for the planning of the subsequent vessel wall imaging.

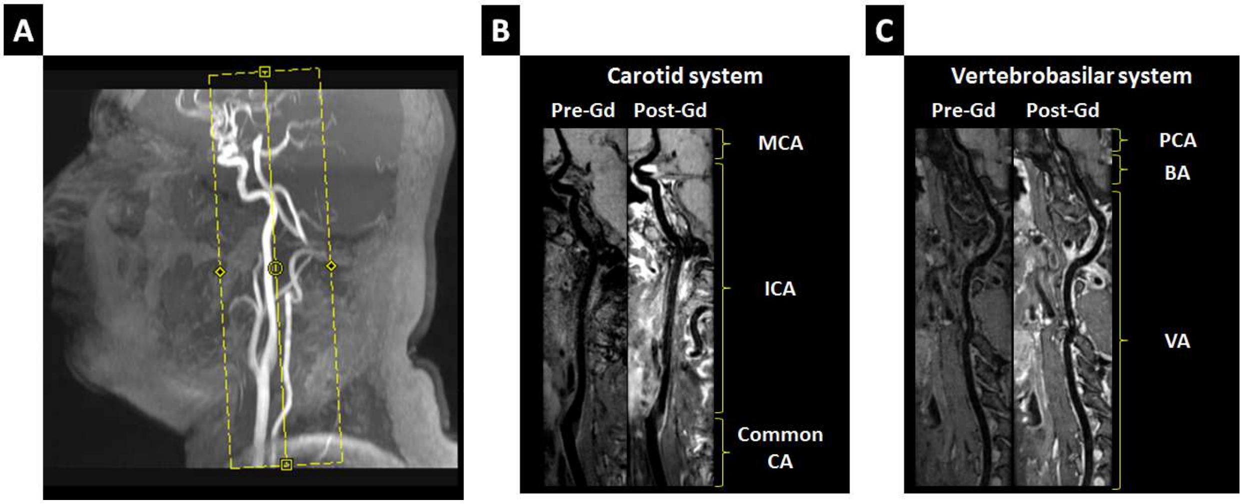

Figure 5.2 Combined imaging of carotid and intracranial vessel wall with DANTE-SPACE. (A) Anatomical coverage of the proposed protocol demonstrated on a sagittal MIP image of TOF MRA. A coronal imaging slab was rotated slightly (yellow box) to cover both carotid and vertibrobasilar arterial systems. (B) Reformatted pre- and post-CE DANTE-SPACE images of carotid arteries and major branches from 2 inches below the bifurcation up to the 2nd segment of middle cerebral artery. (C) Reformatted pre- and post-CE DANTE-SPACE images of vertebral arteries, basilar arteries and major braches up to anterior/posterior cerebral arteries.

Conventional multi-slice T1w 2D TSE images were acquired as reference. Sixteen slices centered at the carotid bifurcations were prescribed with no gap in-between. To further suppress arterial and venous flow, a pair of parallel saturation bands each with thickness of 50mm were placed 10mm above and below the slices group, as described in previous studies [64, 84]. Other imaging parameters include: FOV = $190 \times 190 mm^2$; in-plane resolution = $0.74 \times 0.74 mm^2$; slice thickness = 2mm; TR/TE = 770/9.4ms; turbo factor = 7; pixel bandwidth = 528Hz; refocussing flip angle = 180°; total scan time = 3’33”.

SPACE and DANTE-SPACE images were acquired afterwards. As shown in **Figure 5.2A**, an oblique coronal slab slightly rotated transversely were prescribed to include both carotid and vertibrobasilar arterial systems with a coverage of 190mm in the head-feet direction. It consists of 80 slices each with thickness of 0.74mm, yielding a total slab thickness of 59.2mm in the anterior-posterior direction. A variable flip angle scheme was used for refocusing pulses in order to achieve T1 image contrast. Additional parameters regarding the SPACE readout module include: FOV = $166 \times 190 mm^2$; spatial resolution = 0.74mm isotropic; TR/TE = 770/22ms; turbo factor = 31; pixel bandwidth = 528Hz; parallel imaging iPAT factor = 2; total scan time = 5’57”. After testing on healthy subjects, DANTE echo train parameters were optimized based on the following trade-offs and constraints: 1) larger flip angle provides higher flow sensitivity however at the price of static tissue SNR and increased SAR; 2) higher number of pulses is desired to reach true steady state of static tissue but leads to prolonged scan; 3) motion-sensitizing gradients are required in all three directions to suppress the multi-directional flow in the tortuous intracranial vessels. Final parameters choices for DANTE module include: flip angle = 10°, phase increment = 0°, number of pulses = 100; inter-pulse repeat time= 1ms; Gxyz = 25mT/m.

Post-CE imaging was performed 2 minutes after an intravenous injection of gadoversetamide (OptiMARK, Mallinckrodt, Hazelwood, MO, USA) at the dose of 0.1 mmol/kg body weight. DANTE-SPACE and SPACE images were acquired in randomized order followed by T1w 2D TSE. All imaging parameters were kept identical to those of pre-CE imaging.

5.2.4 Image Processing and Analysis

Signal, noise and morphometric measurements

Images were reviewed and analyzed by two reviewers including an experienced radiologist on a clinical workstation (Leonardo, Siemens AG Healthcare). Multi-planar reformatting (MPR) was performed on each 3D dataset at internal carotid arteries right above carotid bifurcations where residual blood artifacts were most commonly observed. SPACE and DANTE-SPACE images were de-identified and reviewed side-by-side following an automatic co-registration to correct any possible inter-scan motion. Four contiguous 2D cross-sectional images with thickness of 2mm (matched with 2D TSE) of carotid arteries were reconstructed from each dataset for the measurements. Arterial lumen signal (S_{lumen}) was measured as the mean signal intensity within a manually drawn region of interest (ROI) covering the entire arterial lumen. When apparent residual arterial blood was observed, signal of blood (S_{blood}) was measured with a ROI covering the residual blood area. Identical blood ROIs were used on DANTE-SPACE and SPACE image in order to avoid potential bias in the comparison. Vessel wall signal (S_{wall}) was measured as the mean signal intensity of a one-pixel-width circumferential path traced through the middle of the arterial wall in order to mitigate potential inaccuracy induced by partial volume effects.[61] Similarly, venous blood signal (S_{venous}) were measured by a ROI covering the entire lumen of the internal jugular vein. Cerebrospinal fluid (CSF) signal (S_{csf}) was measured at a homogenous area surrounding the cervical spinal cord. Noise level (σ) was defined as the signal standard deviation within a ROI drawn in the adjacent air space of the image uncontaminated by artifacts. Same noise measurement area was used on DANTE-SPACE and SPACE images. The apparent SNR and CNR were defined as:

$$SNR_x = 0.695 \times S_x / \sigma \qquad [1]$$

$$CNR_{x\text{-}to\text{-}y} = 0.695 \times (S_x - S_y) / \sigma \qquad [2]$$

Where S_x denotes the signal intensity of x anatomy (arterial lumen, arterial vessel wall, venous lumen, or CSF); and S_y denotes the signal intensity of background (arterial lumen or residual arterial blood). Multiplier 0.695 is the multi-coil correction factor [85].

Arterial lumen area and vessel wall area were measured on SPACE, DANTE-SPACE and slice-matched 2D TSE images. The inner and outer boundaries of vessel wall were manually traced to form two concentric ROIs. Lumen area was measured by the inner ROI whereas vessel wall area was defined as the area difference between the two ROIs. All measurements were performed blinded to the image type and images from the same subject were analyzed at the same session to ensure consistency.

5.2.5 Statistical Analysis

R statistical programming language (ver. 3.0.3, The R Foundation for Statistical Computing, Vienna, Austria) was used for all statistical analysis. A two-tailed paired Student’s t-test was performed between DANTE-SPACE and SPACE images for SNR_{lumen}, SNR_{wall}, $CNR_{wall\text{-}to\text{-}lumen}$, $CNR_{wall\text{-}to\text{-}blood}$, LA, and WA following verification of data normality with Shapiro-Wilk test. Additionally, agreement in WA and LA measurements between DANTE-SPACE and 2D TSE were assessed with intraclass correlation coefficient. All numerical data are presented in the format of mean±SD and statistical difference is considered significant when $p<0.05$.

5.3 RESULTS

Figure 5.2B and **Figure 5.2C** are representative curved MPRs of pre- and post-CE DANTE-SPACE images from a healthy subject showing integrated views of carotid arteries, middle cerebral arteries, vertebral arteries, basilar arteries and major braches up to anterior/posterior cerebral arteries.

Figure 5.3A shows an example of the simulation results for the percentage relative signal differences between DANTE-SPACE and SPACE within the T1 range of 400~1550ms and T2 range of 20~300ms. It is important to note that simulation results will vary based on DANTE parameters especially DANTE flip angle and in this particular example DANTE and SPACE parameters were assumed identical to the in vivo studies. Signal differences between the two had little dependence on T1 values and showed larger variations towards the lower T2 range (<30ms), although all of which were below 10% across the simulated ranges.

Figure 5.3B shows the comparison between DANTE-SPACE and SPACE for image contrast ratios that are relevant to the identification of different plaque components. The differences between the two sequences were below 3% for all components.

The phantom results in **Figure 5.3C** verified that the addition of DANTE to the SPACE sequence had little impact on the resultant images in terms of contrast variations. The ICC between the signal intensities of DANTE-SPACE and SPACE was very high, ranging from 0.9989 to 0.9999 depending on different DANTE parameter settings. The MSE between the two was all below 0.0005. Similarly, DANTE-SPACE demonstrated consistent contrast behavior compared with conventional T1w 2D TSE, with the ICC between the two ranging from 0.9595 to 0.9738, and MSE below 0.009.

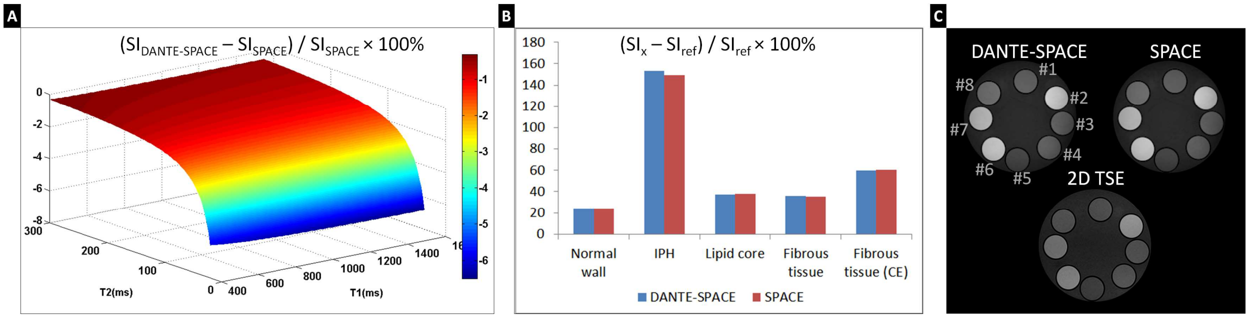

Figure 5.3 (A) Simulated results for the percentage relative signal differences between DANTE-SPACE and SPACE across a range of physiologically relevant T1 (400~1550ms) and T2 (20~300ms) values. DANTE-SPACE parameters included: echo train length = 100; echo spacing = 1ms; TR/TE = 770/22ms. SI = signal intensity. (B) Comparison between DANTE-SPACE and SPACE for image contrast ratios of normal wall, recent hemorrhage, lipid core, and fibrous tissue (each versus skeletal muscle as reference). (C) Images of a T1 phantom consisting of multiple water tubes with different Gd concentration. T1/T2 values of the tubes measured by a basic spin-echo sequence are (in msec): #1:1276/885; #2:261/200; #3:1038/674; #4:1223/813; #5:1845/898; #6:368/291; #7:428/339, and #8:1144/757, respectively. Images were acquired by DANTE-SPACE, SPACE and 2D TSE with the same imaging parameters as the in vivo studies.

Improved arterial blood suppression by DANTE-SPACE was observed in the in vivo study both pre-CE and post-CE. In the 14 healthy subjects who completed the comparative study between DANTE-SPACE and SPACE, apparent arterial residual blood was observed in 5 (pre-CE) and 9 (post-CE) subjects on SPACE images, and 2 (post-CE) subjects on DANTE-SPACE images. **Figure 5.4A** and **Figure 5.4B** are representative examples of improved arterial blood suppression by DANTE-SPACE from two subjects at the carotid bifurcation and the petrous segment of internal carotid, respectively. SPACE images had significant residual blood in the lumen that obscured the vessel wall boundary whereas DANTE-SPACE images had clean lumen free of residual blood with well delineated vessel wall. Quantitative analysis revealed that both pre- and post-CE SNR_{lumen} was significantly decreased by DANTE-SPACE compared with SPACE (Table 1). A slight reduction in SNR_{wall} with DANTE-SPACE was also observed. However, pre-CE $CNR_{wall\text{-}to\text{-}blood}$ was improved by approximately 30% with DANTE-SPACE (11.3±3.6) over SPACE (8.7±3.6) as residual blood was present in the latter. The improvement was more conspicuous for post-CE as $CNR_{wall\text{-}to\text{-}blood}$ was improved by approximately 100% with DANTE-SPACE (24.0±7.7) over SPACE (12.0±4.2).

DANTE-SPACE also enhanced the suppression of venous blood and CSF. **Figure 5.5** shows a representative example of improved venous blood suppression. Post-CE SPACE images had largely unsuppressed venous blood causing overlaying flow artifacts along the PE direction (left to right), whereas slice-matched DANTE-SPACE images showed dark venous lumen with well-suppressed venous blood. The level of flow artifacts was also markedly reduced in the DANTE-SPACE images. Quantitatively, the overall SNR_{venous} was significantly reduced by DANTE-SPACE compared with SPACE, both pre-CE and post-CE (Table 1). **Figure 5.6** includes a representative case of enhanced CSF suppression by DANTE-SPACE. CSF appeared much darker in the DANTE-SPACE images and the outer boundaries of basilar arteries and its branches were better delineated. In all subjects an approximately 40% reduction on average was observed in $\mathrm{SNR}_{\mathrm{csf}}$ with DANTE-SPACE compared with SPACE (Table 1).

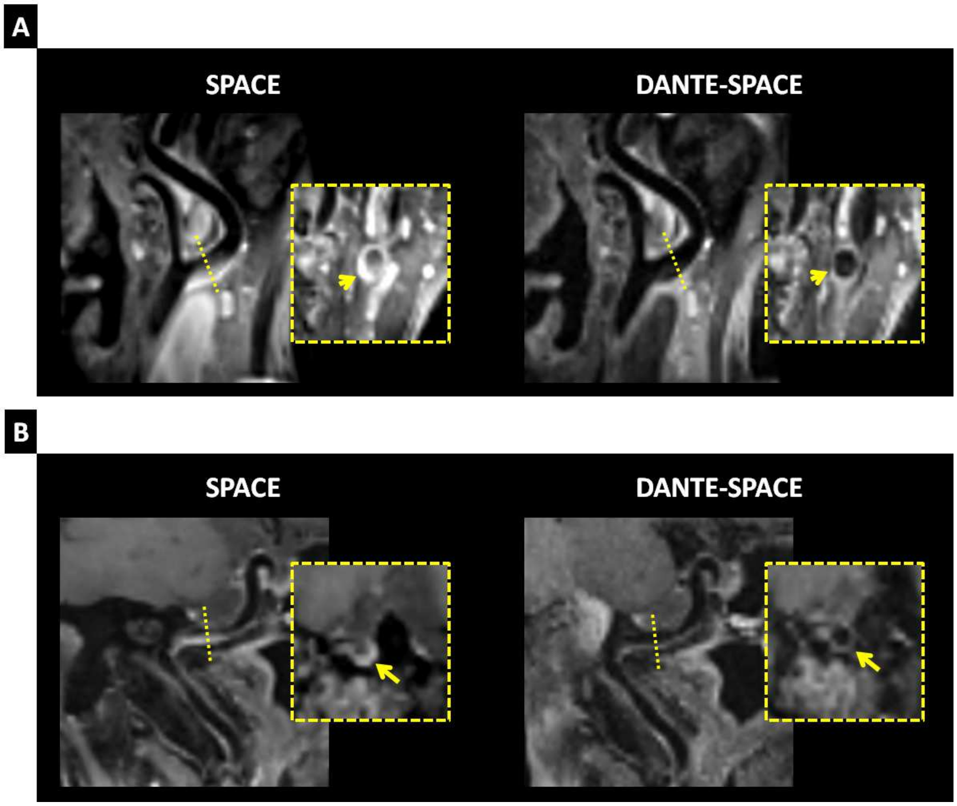

Figure 5.4 Two representative examples of improved arterial blood suppression by DANTE-SPACE. (A) Reformatted post-CE images at the carotid bifurcation from a healthy subject acquired using both SPACE and DANTE-SPACE. On the SPACE images significant residual blood was observed at the origin of internal carotid artery. It obscured the boundary between lumen and vessel wall and may be misidentified as a plaque (yellow arrow). On the DANTE-SPACE images lumen was clean and vessel wall appeared thin. (B) Reformatted post-CE images at internal carotid artery from a symptomatic patient suspected of stroke. Similar findings were observed in comparing SPACE and DANTE-SPACE.

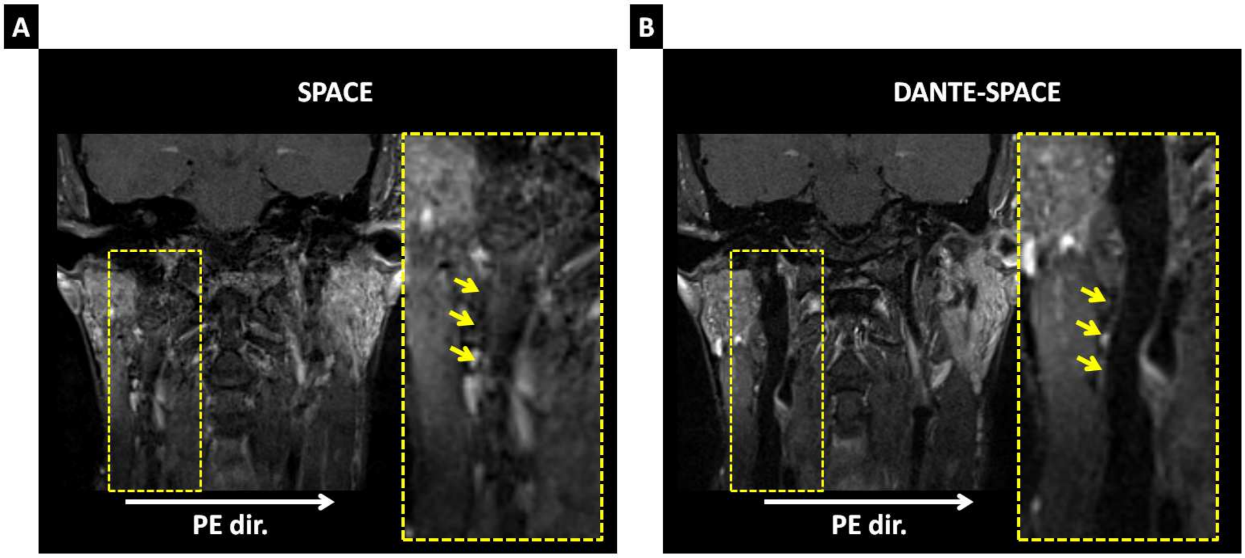

Figure 5.5 A representative example of improved venous blood suppression by DANTE-SPACE. (A) On the post-CE SPACE images the venous blood was largely not suppressed causing visible flow artifacts along the PE direction (left to right). (B) On the post-CE DANTE-SPACE images the venous blood was well suppressed and the venous lumen appeared dark (arrows). Also note the reduced level of flow artifacts compared to SPACE images.

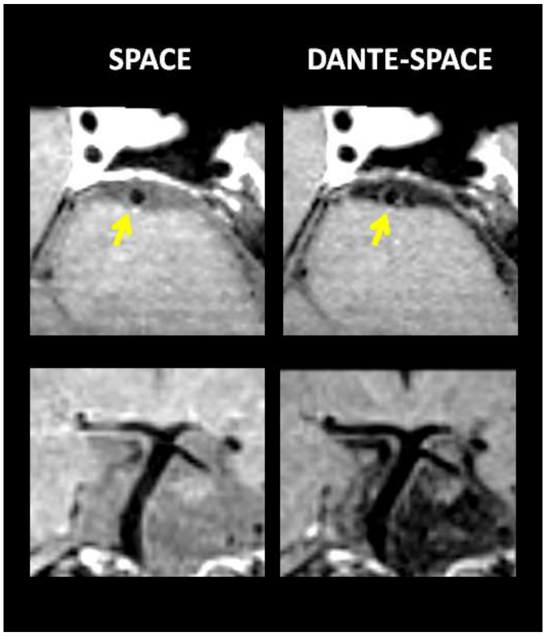

Figure 5.6 A representative example of improved CSF suppression by DANTE-SPACE from a healthy subject. The CSF surrounding the basilar arteries and its branches was further suppressed by DANTE-SPACE compared with SPACE, which helped better visualize the outer vessel boundaries.

Table 5.1 Signal and morphological measurement comparison between DANTE-SPACE and SPACE.

		DANTE-SPACE	SPACE	% Difference	p
Pre-CE	SNR_{lumen}	9.6±2.7	11.0±3.2	-13.2	<0.001
	SNR_{wall}	26.9±7.3	31.0±8.5	-13.3	<0.001
	$CNR_{wall\text{-}to\text{-}blood}$	11.3±3.6	8.7±3.0	+30.8	0.003
	SNR_{venous}	16.8±5.9	22.6±7.7	-25.6	<0.001
	SNR_{csf}	15.1±4.9	24.2±7.5	-37.8	<0.001
	Lumen area	37.6±7.0	37.2±7.2	+1.2	0.05
	Wall area	28.0±6.0	28.5±5.9	-1.8	0.01
Post-CE	SNR_{lumen}	15.9±4.7	20.5±6.3	-22.5	<0.001
	SNR_{wall}	46.0±12.6	52.0±14.4	-11.4	<0.001
	$CNR_{wall\text{-}to\text{-}blood}$	24.0±7.7	12.0±4.2	+100.6	<0.001
	SNR_{venous}	25.5±8.9	40.8±13.6	-37.6	<0.001
	Lumen area	37.4±6.9	36.0±7.2	+3.8	0.001
	Wall area	28.3±5.8	29.9±5.9	-5.3	<0.001

Lumen area and Wall area measured in mm^2

Preliminary clinical study suggested that the proposed DANTE-SPACE protocol had the advantages of a large anatomical coverage and the potential to identify plaque components. **Figure 5.7** shows a case of a patient suspected of carotid artery dissection. The large FOV visualized the carotid arterial system from both sides in its entirety and helped identify the diffused wall thickening along the middle segment of ICA. A thrombus near the bifurcation was also clearly visualized. In-plane and cross-sectional MPR images from the same dataset demonstrated double lumen sign in the intracranial segments of ICA (**Figure 5.7B**). **Figure 5.8** shows a case of a patient with recent stoke. Plaque components including intraplaque hemorrhage (IPH), calcification, and thin fibrous cap were clearly visualized in the DANTE-SPACE images with slice-matched T1w 2D TSE as reference.

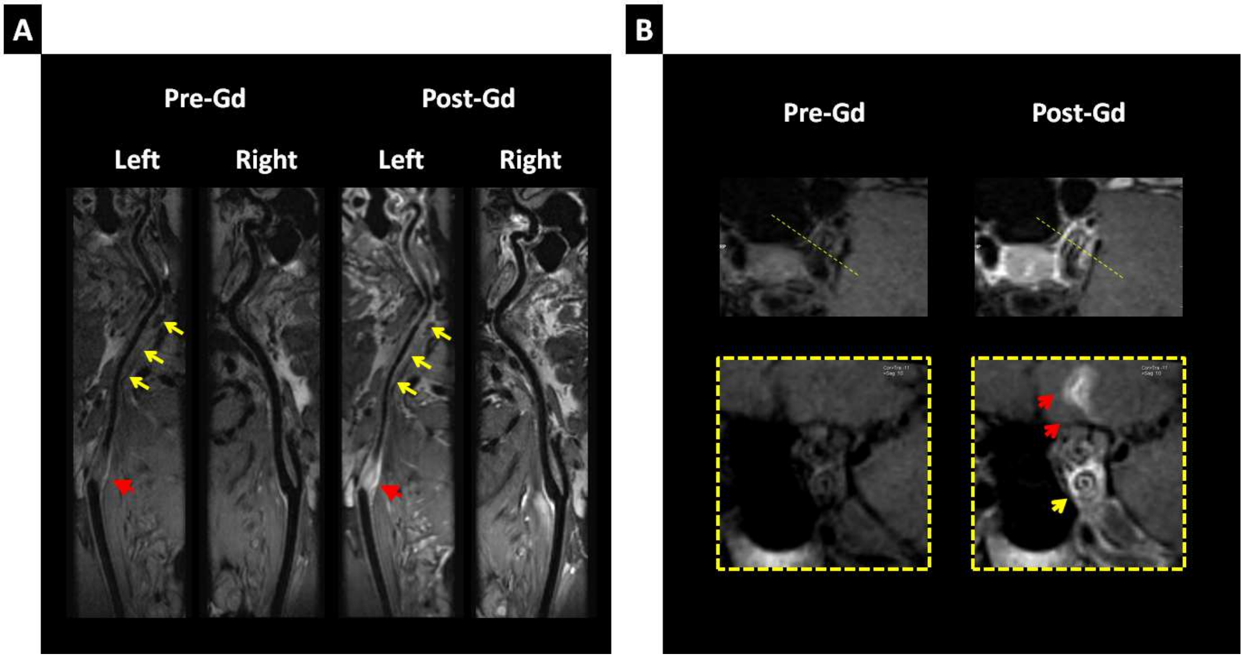

Figure 5.7 Reformatted pre- and post-CE DANTE-SPACE images from a patient suspected of internal carotid artery dissection. The patient was a 43 y/o male with stroke symptoms. (A) Curved MPR images of both the dissected carotid arterial wall (left) and the normal carotid arterial wall (right). Note the thrombus near the bifurcation of the left ICA (single red arrow), and diffused arterial wall thickening along the middle segment (triple yellow arrows). (B) In-plane and cross-sectional images showing double lumen sign (single yellow arrow) of intracranial carotid artery which confirmed the diagnosis of dissection. Also note the enhancement of brain infarct in the post-CE image (double red arrows).

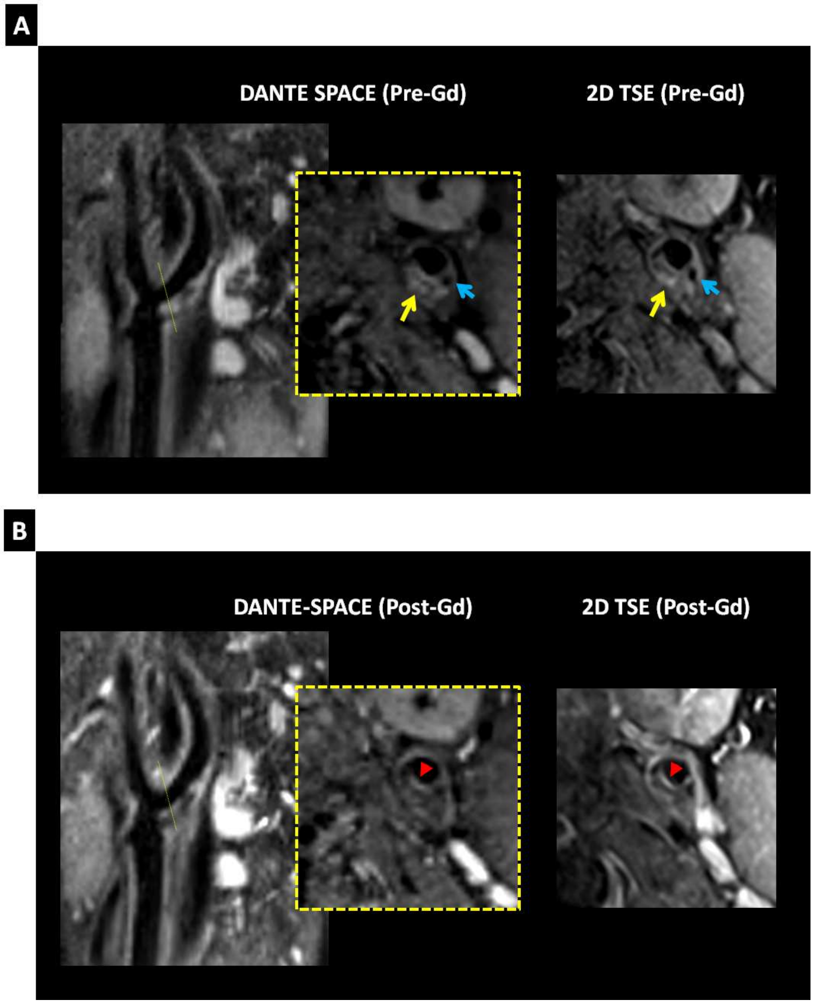

Figure 5.8 Reformatted pre- and post-CE DANTE-SPACE images of a vulnerable plaque. The patient was a 41 y/o male with stroke symptoms. Slice-matched T1w 2D TSE images were acquired as reference. (A) Pre-CE DANTE-SPACE images at the bifurcation showed hyperintensive plaque component suggesting intraplaque hemorrhage (yellow arrows). Also note the hypointense plaque component suggesting calcification (blue arrows). (B) Post-CE DANTE-SPACE images showed enhanced plaque component next to the lumen suggesting thin fibrous cap (red arrows).

Morphometric analysis of the images revealed certain bias between DANTE-SPACE and SPACE images. Increased wall area (WA) and decreased lumen area (LA) were observed in SPACE images compared with DANTE-SPACE images both pre- and post-CE (Table 1). Notably, WA and LA measurements showed significant difference between pre-CE and post-CE in SPACE images (p<0.001), whereas no such phenomenon was observed in DANTE-SPACE images (p>0.1). DANTE-SPACE and 2D TSE images showed good correlation: the ICC between the two on lumen area was 0.997 for pre-CE and 0.987 for post-CE, whereas the ICC on wall area was 0.996 for pre-CE and 0.989 for post-CE (all p<0.001).

Two subjects required using the optional anti-aliasing regional saturation module, which largely eliminated aliasing from the shoulders and improved vessel wall visualization (**Figure 5.9**).

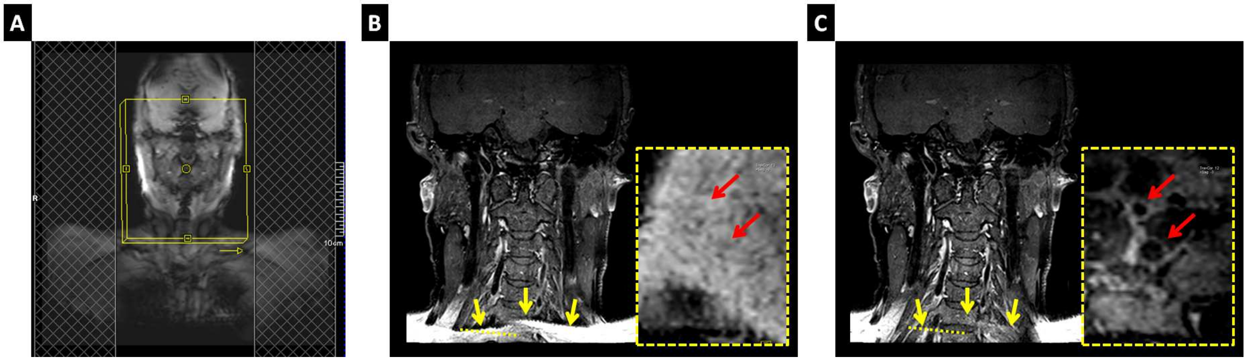

Figure 5.9 A representative case in which anti-aliasing regional saturation module (R-sat) improved vessel wall visualization. (A) The positioning of R-sat bands (gray shaded area) relative to the imaging slab (yellow box) for the suppression of shoulder signal. (B) Without R-sat bright signal from the shoulders overlapped into the FOV, making vessels completely invisible. (C) With R-sat the vessel wall of common carotid and vertebral arteries were visible (red arrows).

5.4 DISCUSSION

In this work we introduced an improved black-blood imaging protocol with DANTE-SPACE for combined evaluation of both carotid and intracranial vessel wall. Superior suppression of arterial blood, venous blood and CSF was observed with DANTE-SPACE compared with SPACE. The proposed protocol covered a large anatomical region with common sites of atherosclerosis formation and 3D imaging with high isotropic resolution (0.7mm) was achieved in a clinically acceptable scan time (<6mins).

Complete blood suppression is crucial to accurate measurements and evaluation of arterial vessel wall and plaques. However we observed in this study that relying on the native black-blood effects by SPACE alone was not sufficient for many subjects, leaving residual luminal blood that can be mistaken as thickened wall. This was particularly problematic for post-CE imaging as the majority of the subjects in the study showed apparent residual blood in SPACE images, presumably due to vastly shortened blood T1. DANTE-SPACE reduced the residual blood signal in these subjects. Notably, $CNR_{wall\text{-}to\text{-}blood}$ was increased by about 30% and 100% in DANTE-SPACE images pre-CE and post-CE, respectively. Increased lumen area and reduced vessel wall area were also observed in DANTE-SPACE images which suggested that near-boundary blood signal was further suppressed.

In SPACE images, residual blood artifacts were more likely to occur at certain anatomical locations, including carotid bifurcations, petrous and lacerum segments of ICAs. The irregular anatomy and flow patterns at these locations could result in slow or stagnant flow [64], leading to insufficient phase dispersion during SPACE's echo train. We hypothesize that the improvements by DANTE-SPACE arose from a two-fold mechanism: 1) it suppressed slow flow because of the application of a steady-state pulse train; 2) it supplemented SPACE in directions where native blood suppression was insufficient. In particular, we observed that DANTE-SPACE provided very robust arterial blood suppression in post-CE imaging regardless of the delay time after contrast bolus injection as similar results were achieved even without any delay time (data not shown). This may provide more flexibility in its clinical usage and reduce the possibility of inter-scan motion between pre- and post-CE images. Combining with more advanced imaging acceleration techniques, DANTE-SPACE may be used for 3D black-blood dynamic contrast-enhanced (DCE) imaging for assessing plaque inflammation.

In addition to improved arterial wall imaging, an interesting 'byproduct' of DANTE-SPACE sequence was the further suppression of venous blood and CSF. Venous blood flows at a much lower rate than arterial blood and is not as rhythmic [86]. Incomplete and inconsistent venous blood signal intensity between shots could lead to flow artifacts and degradation of image quality. Flow artifacts were generally negligible in pre-CE SPACE images but became more noticeable post-CE imaging. The improved venous blood suppression by DANTE-SPACE reduced flow artifacts and may also benefit certain applications such as venous thrombus imaging [87]. We observed that DANTE-SPACE significantly reduced CSF signal and improved the visualization of vessel walls surrounded by CSF, such as BA and intracranial segments of carotid artery. The improvement in contrast between vessel wall and CSF would become more beneficial for T2- and proton-weighted imaging as CSF naturally appears bright in these images. We hypothesize that the primary reason behind these findings is the property of DANTE module to suppress 'slow' flow. The study by Li et al [80] found that DANTE preparation can attenuate signal from moving spins with velocity as low as 1 mm/s. However, it is important to note that venous and CSF flow rate may vary greatly depending on locations and disease states. Therefore a systematic study, preferably on patients, is mandatory to further validate these benefits.

The proposed DANTE-SPACE protocol had several advantages compared with the conventional 2D TSE protocol as demonstrated in the preliminary patient study. First, it provided sub-millimeter isotropic spatial resolution (0.7x0.7x0.7 mm^3), with about three-fold improvement in the slice direction compared with the 2D technique (0.7x0.7x2.0 mm^3). This may provide substantial clinical benefits for visualizing individual plaque components as their size are typically sub-millimeter [44], smaller than a single voxel in the 2D technique. We found that the resolution improvement was particularly useful for fibrous cap assessment, which can be very difficult due to partial volume effect in 2D images [49]. Second, 3D image volume can be easily reformatted to images with arbitrary slice thickness and orientation, providing great flexibility for clinicians to accurately evaluate the extent of lesion. It should also make it easier to correct for misregistration between different scans, for example, in comparing images before and after therapy. Third, the protocol provides large anatomical coverage which enables an integral assessment of both extra- and intracranial vessel wall. Typical 2D TSE protocols use multiple transverse slices that only covers 50mm or less of vasculature at a time. Intracranial arterial wall can only be imaged separately and the locations of plaques have to be carefully identified on MRA images before slices can be prescribed at the lesions [88]. The proposed protocol covered 190mm of vasculature and can be prescribed without a priori knowledge of plaque locations. The large FOV could also facilitate the evaluation of conditions that affect extensive vascular beds, as shown in the ICA dissection case in the patient study. In certain patients the proposed imaging orientation may cause aliasing from the shoulders, which can be largely eliminated by applying regional saturation bands.

This study has certain limitations. First, DANTE-SPACE reduced SNRwall for approximately 13% compared with SPACE in this study, resulting in appreciable differences between the two. However, the SNR reduction was less than those typically seen in studies using MSDE, which ranges from 20% to 40% [61, 64, 77, 89]. Similar SNR advantages by DANTE were also observed by Li et al when using it with FLASH readout (DASH) [78]. The DANTE pulse train parameters should be designed according to imaging strategy. Generally the BB effect of DANTE module increases with larger flip angle, at the expense of higher signal loss to static tissue. We used a moderate flip angle of 10° in the study design as we intended to use DANTE as a supplement to SPACE's native BB effect with less of a penalty on SNR. Second, both the BB module and readout module were relatively long in DANTE-SPACE, which may potentially increase motion sensitivity to the 3D acquisition. One way to mitigate pulsatile motion is the use of ECG triggering, which should not increase scan time because the TR in the current protocol is similar to a typical RR interval. Navigator [90] or self-gating [91] methods may be adopted in the future. Third, we only designed a T1w protocol in order to reduce the overall exam duration. Multiple contrasts may facilitate the identification of plaque composition [44]. It is important to note that T2- and PD-weighted contrasts are also possible to achieve since image contrast is dominated by the readout contrast in DANTE prepared sequences [78].

5.5 CONCLUSION

DANTE-SPACE is a promising black-blood technique that significantly improves arterial and venous blood suppression pre- and post-CE compared with conventional SPACE technique. Simultaneous high-resolution 3D carotid and intracranial imaging using DANTE-SPACE is feasible and time-efficient, with the potential ability to identify different plaque components and evaluate plaque vulnerability in the head and neck.

CHAPTER 6: WHOLE-HEART CORONARY PLAQUE CHARACTERIZATION WITH INTERLEAVED BRIGHT-BLOOD REFERENCE

6.1 BACKGROUND

Plaque rupture is the most common type of coronary plaque complication, accounting for approximately 70% of fatal acute myocardial infarctions and/or sudden coronary deaths [6, 46]. Recently T1-weighted (T1w) MRI with [92] or without [93] contrast enhancement (CE) has been attempted for characterizing coronary plaques. Noguchi et al examined the signal intensity of coronary plaques on noncontrast T1w MRI from 568 patients with suspected or know coronary artery disease (CAD), and showed that high intensity plaques are associated with higher coronary events during a six-year follow-up [94]. Varma et al investigated the coronary wall enhancement by gadolinium in T1w MRI images from CAD and lupus patients and found that coronary CE may serve as a direct marker for vessel wall injury and remodeling related to inflammation [95].

Despite the promising prognostic capability of T1w MRI for CAD, the current protocols using conventional Cartesian acquisition and navigator gating has several drawbacks that may hinder the clinical application of this technique. First, the anatomical coverage is limited to only the proximal segments of coronary arteries. Second, current spatial resolution is low and anisotropic, leading to blurring and partial volume effects. Third, the acquisition time is long and unpredictable, depending largely on the breathing pattern of the patient. Patient movement associated with prolonged scan can cause considerable exclusion rate due to poor image quality [94]. Lastly, because the background tissue in T1w MRI is heavily suppressed, a separate acquisition of bright-blood images is needed in order to provide the anatomical reference for identifying and localizing lesions. This further lengthens the total scan time and requires additional image registration with T1w images.

To address the aforementioned limitations of current protocols, the purpose of this work is to develop a time-efficient protocol for coronary artery plaque characterization that provides 1) 3D whole-heart coverage, 2) isotropic high spatial resolution (1.1^3 mm^3), and 3) simultaneously acquired dark-blood T1w images and bright-blood images as anatomical reference.

6.2 METHODS

Pulse sequence design

The proposed MR acquisition method was based on prospectively ECG-gated, inversion recovery (IR) prepared spoiled gradient echo (FLASH) sequence with golden angle 3D radial trajectory (**Figure 6.1A**). The IR pulse was played out every other heartbeat, allowing interleaved acquisition of dark-blood T1w images and bright-blood reference images. Slab-selective excitation pulses were used to suppress the tissue outside of the heart in order to reduce the streaking artifacts. Spectral Adiabatic Inversion Recovery (SPAIR) was used together with water-only excitation pulses to suppress the signal from epicardial fat. No respiratory gating was applied with all of the imaging data utilized for reconstruction (100% respiratory gating efficiency). Diaphragm navigator was only turned on in 'monitor-only' mode for monitoring patients' breathing condition during the scan.

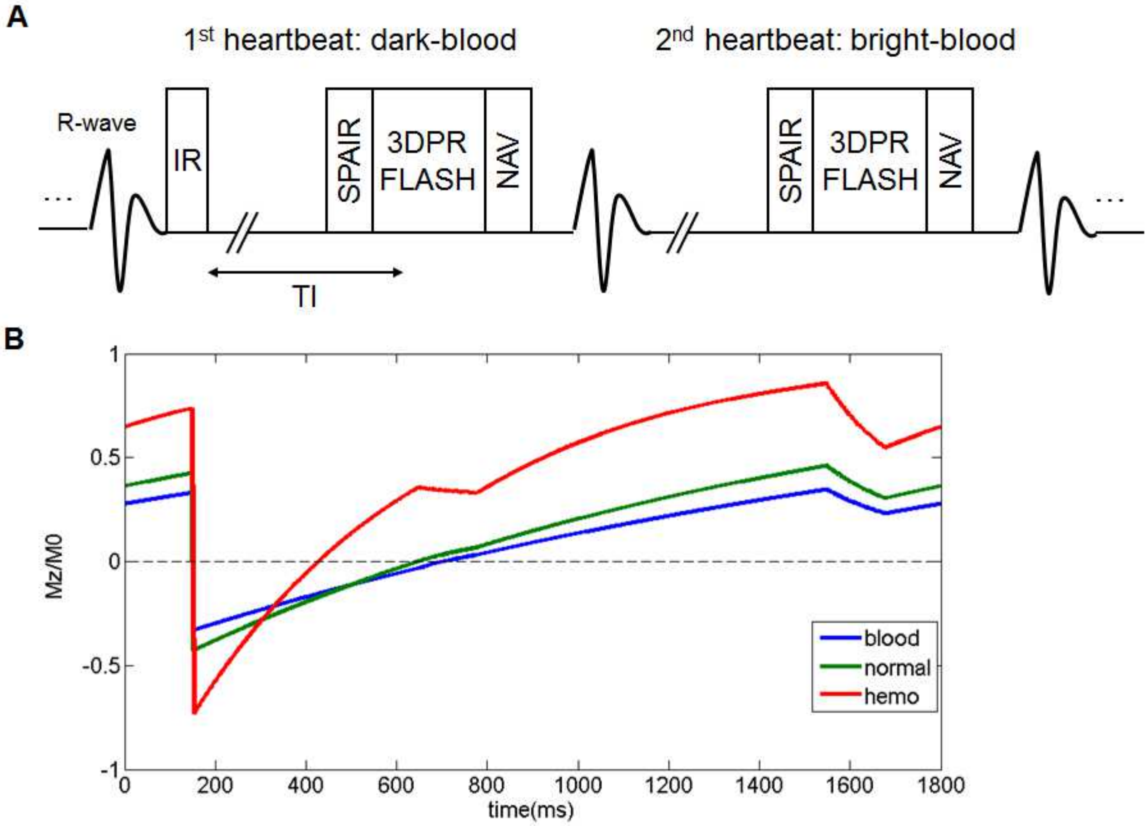

Figure 6.1 A: Sequence diagram of 3DPR interleaved dark-blood (T1w) and bright-blood coronary imaging. B: Simulated steady-state signal behavior of different tissue types (blood, normal vessel wall, and hemorrhage).

Image reconstruction scheme

Retrospective motion correction was performed with an integrated self-calibrating iterative SENSE scheme. Both dark-blood and bright-blood k-space data were segmented into six respiratory bins using the navigator signal as a uniform reference. An image-based affine motion correction algorithm [96] was used to correct for respiratory motion between different bins (**Figure 6.2**). Breathing motion was estimated based on the high SNR bright-blood data. Identical motion transformation matrices were then shared by both dark-blood and bright-blood images because they were acquired in an interleaved fashion.

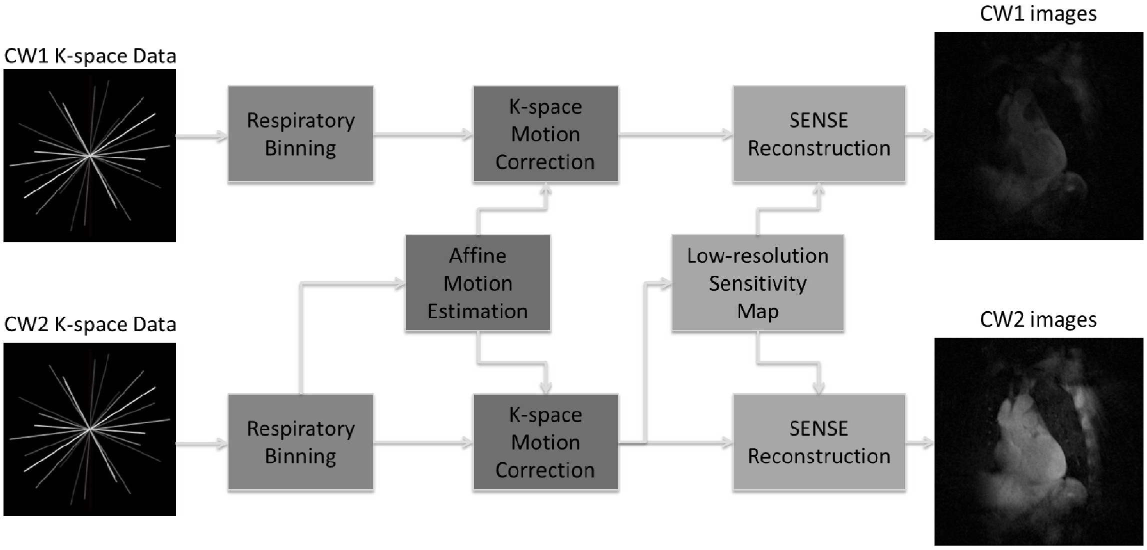

Figure 6.2 Schematic flow chart of the image reconstruction processes of interleaved dark-blood T1w images and bright-blood reference images. Motion compensation and parallel imaging (SENSE) were integrated in the joint reconstruction utilizing the high SNR of the bright-blood MR data. CW = contrast weighting.

In vivo imaging

Healthy volunteers (n=12) and CAD patients with stable and unstable angina (n=26) were recruited with informed consent and scanned on a 3T scanner (Siemens Magnetom Trio) before and after contrast enhancement. Gadoterate meglumine (Dotarem, Bloomington, IN, USA) was injected intravenously with the dose of 0.1 mmol/kg bodyweight at the injection rate of 2mL/second, followed by 20 mL of saline flush. T1w MRI was acquired using the following parameters: 3D sagittal slab covering the entire heart with FOV = 330^3 mm^3; matrix size = 288^3; spatial resolution = 1.13 mm^3; FA = 12°; TR/TE = 4.6/2.3 ms; BW = 721 Hz/pixel; total number of radial projections = 8500; scan time was approximately 10 minutes depending on heart rate. After completing MRI, 21 CAD patients underwent interventional X-ray angiography and intracoronary optical coherence tomography (OCT) for coronary plaque evaluation.

6.3 RESULTS

All 38 subjects successful completed the pre-CE T1w MRI. All 12 healthy volunteers and 23 eligible patients also completed the post-CE T1w MRI. None of the healthy subjects showed hyper-intensive plaques in either pre-CE or post-CE T1w MRI. Three patients showed HIPs on pre-CE T1w MRI and 4 patients showed HIPs on post-CE T1w MRI, respectively.

Figure 6.3 shows a representative patient case with a HIP on pre-CE T1w MRI. Pre-CE T1w images showed a HIP at middle LAD as localized on the bright-blood images. CTA and X-ray showed significant stenosis (70%) at that location and the plaque appeared to be of low-density. OCT image showed large signal-poor area suggestive of possible lipid core/intra-plaque hemorrhage (yellow arrows).

Figure 6.4 shows a representative patient case with a HIP on post-CE T1w MRI. Pre-CE T1w images showed no HIP. Post-CE T1w showed diffused wall enhancement at proximal RCA as localized on the bright-blood images. Corresponding X-ray angiography showed only mild stenosis (30%) at proximal RCA. CTA showed marked positive modeling at the location of the stenosis. OCT image showed strong multi-focal back reflections and signal heterogeneity within the overlying tissue suggestive of high macrophage density (yellow arrows).

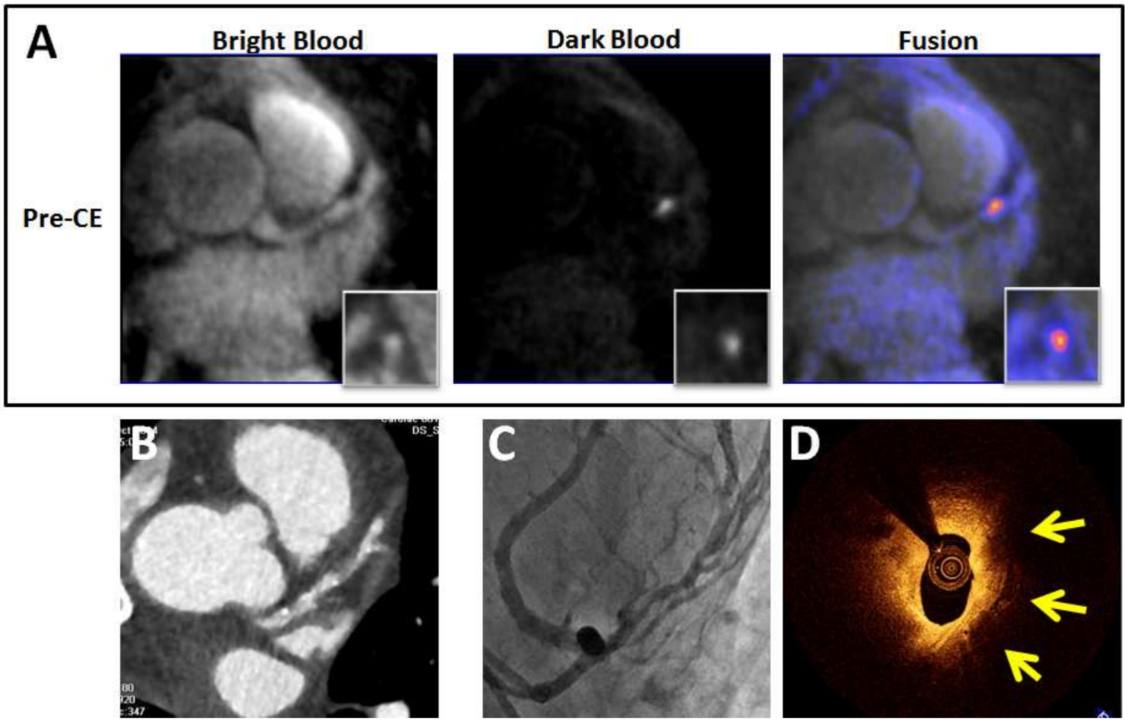

Figure 6.3 Representative case of a CAD patient with a HIP at middle LAD on pre-CE T1w MRI. A: Pre-CE dark-blood T1w images and bright-blood reference images. B: CT angiography. C: X-ray angiography. D: OCT cross-sectional image at the corresponding location of the HIP on MRI.

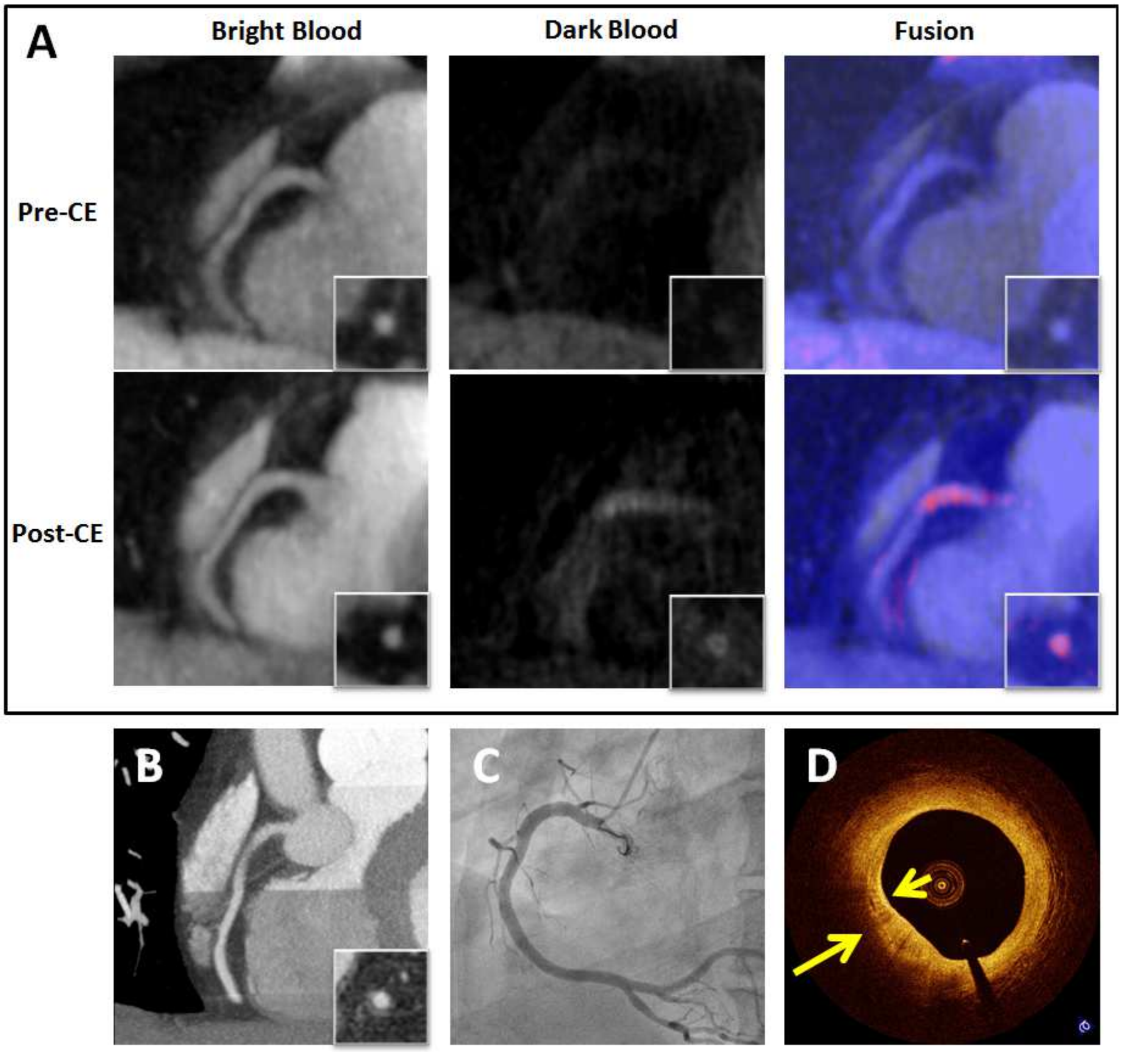

Figure 6.4 Representative case of a CAD patient with a HIP at proximal RCA on post-CE T1w MRI. A: Pre-CE and post-CE dark-blood T1w images and bright-blood reference images. B: CT angiography. C: X-ray angiography. D: OCT cross-sectional image at the corresponding location of the HIP on MRI.

6.4 DISCUSSION

The proposed imaging method allowed, for the first time, whole-heart coronary plaque characterization with simultaneously acquired bright-blood reference. The bright-blood images were inherently co-registered to the T1w images therefore may be used for localizing lesions and evaluating luminal stenosis. Significant acceleration in image acquisition was allowed by the advanced image reconstruction scheme including motion correction (100% respiratory gating efficiency) and parallel imaging (SENSE). Isotropic high resolution coronary imaging was possible with clinically feasible scan time of approximately 10 minutes.

Preliminary comparison with OCT suggested that the HIPs on the pre-CE T1w images may be associated with lipid core and/or hemorrhage, whereas HIPs on the post-CE T1w images may be associated with neovascularization/inflammation. Further clinical validation of this technique with OCT in a larger population is currently underway. Future studies should include correlation to the gold standard histology using specific animal models of intra-plaque hemorrhage and inflammation [97].

6.5 CONCLUSION

Time-efficient T1-weighted whole-heart coronary plaque imaging with isotropic high resolution and simultaneously acquired bright-blood reference was feasible. The proposed method demonstrated the potential to characterize atherosclerotic plaques in the coronary wall.

CHAPTER 7: SUMMARY AND FUTURE WORK

7.1 SUMMARY OF THE WORK

The general aim of this dissertation is to improve the capability of vascular MRI to accurately detect and characterize atherosclerotic lesions. Specifically, four areas of improvements are made in this work.

7.1.1 Self-Gated Renal MRA

Conventional diaphragm navigator gating has several drawbacks, including complicated planning, and saturation artifacts. A noncontrast MRA pulse sequence and online self-gating program (ADIOS) were developed to address these limitations. Motion information was derived directly from the imaging slab for prospective online gating. Scan efficiency was maintained by an automatic adaptive online algorithm. Qualitative and quantitative assessments of image quality were performed and compared with conventional diaphragm navigator. Similarly good image quality was observed in the proximal-middle renal arteries with the proposed method compared with navigator. Superior image quality was observed in the middle-distal renal arteries in the right kidneys with no navigator-induced artifacts. Maximal visible artery length was significantly longer with ADIOS versus navigator in the right kidneys. ADIOS completely eliminated navigator setup and significantly reduced scan time.

7.1.2 Diffusion-Weighted Imaging of Carotid Arteries

Current imaging MRI techniques for detecting plaque lipid core require contrast enhancement and are not available to patients with renal insufficiency. A diffusion-prepared turbo-spin-echo (DP-TSE) technique was developed to enable 3D high resolution diffusion weighted imaging for carotid plaque characterization without the need of contrast enhancement. DP-TSE uses a diffusion encoding module separated from the readout, allowing for segmented acquisition without causing phase errors between shots. An interleaved, motion-compensated sequence was designed to enable 3D black-blood DWI of carotid arteries with sub-millimeter resolution. In the study of healthy subjects and patients, DP-TSE demonstrated advantages over conventional sequence for resolution and image quality. Specifically, the proposed method showed significantly higher vessel wall visibility, less distortion, and less partial volume effect. Apparent diffusion coefficient demonstrated its potential to differentiate lipid core from fibrous plaque tissue.

7.1.3 Simultaneous Intracranial and Carotid Vessel Wall Imaging

Complete luminal blood suppression is crucial for vessel wall imaging however difficult to achieve. This is even more difficult after contrast injection, which causes fast blood signal recovery. To address these limitations a new flow suppression module, DANTE preparation, was incorporated into the conventional SPACE sequence to improve blood signal suppression. Simulations and phantom studies were performed to quantify image contrast variations induced by DANTE. DANTE-SPACE, SPACE and the reference 2D TSE were compared for apparent SNR, CNR and morphometric measurements in healthy subjects. Results showed that simultaneous high-resolution carotid and intracranial vessel wall imaging was feasible with scan time under 6 minutes. DANTE-SPACE significantly improved arterial and venous blood suppression compared with SPACE. Preliminary clinical validation was performed in six symptomatic patients. Results showed that the proposed method had the potential to accurately detect vessel dissection and differentiate plaque components.

7.1.4 Coronary Plaque Imaging with Interleaved Bright-Blood Reference

Current coronary plaque imaging methods suffer from long scan time, limited resolution and coverage. We developed new acquisition and reconstruction strategies for coronary plaque characterization with interleaved dark-blood and bright-blood imaging. We designed golden-angle 3D radial trajectory and an image-based affine motion correction algorithm to allow 100% gating efficiency of the MR data without inducing breathing artifacts. Results from healthy subjects demonstrated the feasible of time-efficient T1w whole-heart coronary plaque imaging with isotropic high resolution and simultaneously acquired bright-blood reference. Preliminary results from patients with coronary artery disease demonstrated the potential of this technique to detect intra-plaque hemorrhage and inflammation in the coronary wall.

7.2 FUTURE WORK

7.2.1 Elimination of Breath-Holding and Residual Respiratory Motion

Current implementation of online self-gating mechanism in this work involves a short breath-hold to establish the reference diaphragm position for subsequent data acquisition. The need for breath-hold can be eliminated in future by integrating an analysis of self-gating profiles in the algorithm to automatically identify the end-expiration phase and record the reference profile.

Residual respiratory motion within the acquired data is not addressed in the current prospective self-gating scheme. Although no apparent effects on image quality were observed in healthy subjects, patients with large and irregular breathing motion may be challenging to image with only prospective gating. Future development shall focus on incorporating retrospective motion correction into the image reconstruction to reduce residual motion in the gated data. One possible solution is to estimate the physical translation based on the self-gating profile shift and apply corresponding phase correction on the acquired k-space data.

7.2.2 Quantitative Analysis of Plaque Apparent Diffusion Coefficient

In our study the ADC values measured from lipid core were significantly lower than normal vessel wall and fibrous plaque tissue which provided promise of using ADC as a way to specifically detect lipid core. However since the work was primarily focused on the technical development, only a limited number of patients were studied. Future work should include the validation in a larger patient population, preferably with comparison to histology of endarterectomy tissue samples as the gold standard. Double-blinded readings of DWI and CE MRI shall be performed independently in the patients. Reference ADC value ranges need to be established for healthy vessel wall and different plaque components including lipid core, fibrous tissue and so forth. The quantitative relationship between ADC and lipid amount in the plaque needs to establish, allowing ADC as a biomarker for evaluating lipid-lowing therapies.

7.2.3 Black-Blood Module Optimization

The black-blood DANTE module provides large flexibility in its design including RF pulse amplitude (flip angle), phase, echo spacing, and total number of RF pulses. Black-blood properties of DANTE depend heavily on these parameters. Signal loss in the static tissue related to DANTE also depends on its parameter setup. Future work is warranted to optimize DANTE and image readout parameters based on particular applications. For example, spinal cord imaging may require a ‘strong’ DANTE module to achieve complete suppression of the slow-flowing CSF (at the expense of more signal loss) whereas venous thrombus imaging may only require a ‘moderate’ DANTE module. Custom design should be based on specific location, anatomy, and flow properties in healthy and disease states.

7.2.4 Robustness to Arrhythmia and Compatibility with Stents

Coronary plaque imaging protocol developed in this work has shown promising clinical potential to detect intra-plaque hemorrhage and vascular inflammation by comparison to other modalities. However, currently there is no gold standard to confirm these results and further validate the detection of the two biomarkers. Future study shall be focused on using animal models and comparing with histology to verify the MRI findings.

There are two potential major practical issues in the application of this technique to larger patient population. Firstly, current technique still relies on ECG triggering and relatively stable heart rate. Image quality will likely suffer significant degradation in patients with severe arrhythmia. A possible solution is retrospective cardiac gating based on ECG recording with asynchronous, fixed sequence timing. Secondly, many patients already have received stents from previous procedures, which will cause severe signal loss in MRI. Potential solutions may include replacing regular inversion pulse with wide-band pulse and using ultra-short echo time during the imaging readout.

BIBLIOGRAPHY

1. Mozaffarian, D., et al., *Heart disease and stroke statistics--2015 update: a report from the American Heart Association.* Circulation, 2015. **131**(4): p. e29-322.

2. Ross, R., *Atherosclerosis is an inflammatory disease.* Am Heart J, 1999. **138**(5 Pt 2): p. S419-20.

3. Ross, R., *Atherosclerosis--an inflammatory disease.* N Engl J Med, 1999. **340**(2): p. 115-26.

4. Virmani, R., et al., *Histopathology of carotid atherosclerotic disease.* Neurosurgery, 2006. **59**(5 Suppl 3): p. S219-27; discussion S3-13.

5. Maseri, A. and V. Fuster, *Is there a vulnerable plaque?* Circulation, 2003. **107**(16): p. 2068-71.

6. Naghavi, M., et al., *From vulnerable plaque to vulnerable patient: a call for new definitions and risk assessment strategies: Part I.* Circulation, 2003. **108**(14): p. 1664-72.

7. Enos, W.F., R.H. Holmes, and J. Beyer, *Coronary disease among United States soldiers killed in action in Korea; preliminary report.* J Am Med Assoc, 1953. **152**(12): p. 1090-3.

8. D'Agostino, R.B., Sr., et al., *General cardiovascular risk profile for use in primary care: the Framingham Heart Study.* Circulation, 2008. **117**(6): p. 743-53.

9. Callahan, M.J., et al., *Nonionic iodinated intravenous contrast material-related reactions: incidence in large urban children's hospital--retrospective analysis of data in 12,494 patients.* Radiology, 2009. **250**(3): p. 674-81.

10. Detrano, R., et al., *Coronary calcium as a predictor of coronary events in four racial or ethnic groups.* N Engl J Med, 2008. **358**(13): p. 1336-45.

11. Tawakol, A., et al., *In vivo 18F-fluorodeoxyglucose positron emission tomography imaging provides a noninvasive measure of carotid plaque inflammation in patients.* J Am Coll Cardiol, 2006. **48**(9): p. 1818-24.

12. Prati, F., et al., *Correlation between high frequency intravascular ultrasound and histomorphology in human coronary arteries.* Heart, 2001. **85**(5): p. 567-70.

13. Nasu, K., et al., *Accuracy of in vivo coronary plaque morphology assessment: a validation study of in vivo virtual histology compared with in vitro histopathology.* J Am Coll Cardiol, 2006. **47**(12): p. 2405-12.

14. Yabushita, H., et al., *Characterization of human atherosclerosis by optical coherence tomography.* Circulation, 2002. **106**(13): p. 1640-5.

15. Jang, I.K., *Near infrared spectroscopy: another toy or indispensible diagnostic tool?* Circ Cardiovasc Interv, 2012. **5**(1): p. 10-1.

16. Korosec, F.R., et al., *Time-resolved contrast-enhanced 3D MR angiography.* Magn Reson Med, 1996. **36**(3): p. 345-51.

17. Grobner, T. and F. Prischl, *Gadolinium and nephrogenic systemic fibrosis.* Kidney international, 2007. **72**(3): p. 260-264.

18. Gronas, R., et al., *Flow-independent angiography for peripheral vascular disease: initial in-vivo results.* J Magn Reson Imaging, 1997. **7**(4): p. 637-43.

19. Cai, J.M., et al., *Classification of human carotid atherosclerotic lesions with in vivo multicontrast magnetic resonance imaging.* Circulation, 2002. **106**(11): p. 1368-73.

20. Miyazaki, M. and H. Isoda, *Non-contrast-enhanced MR angiography of the abdomen.* European journal of radiology, 2011. **80**(1): p. 9-23.

21. Liu, X., et al., *Renal transplant: Nonenhanced renal MR angiography with magnetization-prepared steady-state free precession.* Radiology, 2009. **251**(2): p. 535-542.

22. Marckmann, P., et al., *Nephrogenic systemic fibrosis: suspected causative role of gadodiamide used for contrast-enhanced magnetic resonance imaging.* Journal of the American Society of Nephrology, 2006. **17**(9): p. 2359-2362.

23. Grist, T.M., *Magnetic resonance angiography of renal artery stenosis.* American journal of kidney diseases: the official journal of the National Kidney Foundation, 1994. **24**(4): p. 700.

24. Kaandorp, D.W., et al., *Motion of the proximal renal artery during the cardiac cycle.* Journal of Magnetic Resonance Imaging, 2000. **12**(6): p. 924-928.

25. Katoh, M., et al., *Free-breathing renal MR angiography with steady-state free-precession (SSFP) and slab-selective spin inversion: initial results.* Kidney international, 2004. **66**(3): p. 1272-1278.

26. Liu, Y.L., et al., *A monitoring, feedback, and triggering system for reproducible breath-hold MR imaging.* Magnetic Resonance in Medicine, 1993. **30**(4): p. 507-511.

27. Moghari, M.H., et al., *Subject-specific estimation of respiratory navigator tracking factor for free-breathing cardiovascular MR.* Magnetic Resonance in Medicine, 2011. **67**(6): p. 1665-1672.

28. Lanzman, R.S., et al., *Nonenhanced free-breathing ECG-gated steady-state free precession 3D MR angiography of the renal arteries: comparison between 1.5 T and 3 T.* American Journal of Roentgenology, 2010. **194**(3): p. 794-798.

29. Ehman, R., et al., *Magnetic resonance imaging with respiratory gating: techniques and advantages.* American Journal of Roentgenology, 1984. **143**(6): p. 1175-1182.

30. Santelli, C., et al., *Respiratory bellows revisited for motion compensation: preliminary experience for cardiovascular MR.* Magnetic Resonance in Medicine, 2011. **65**(4): p. 1097-1102.

31. Madore, B., et al., *A new strategy for respiration compensation, applied toward 3D free-breathing cardiac MRI.* Magnetic resonance imaging, 2006. **24**(6): p. 727-737.

32. Danias, P.G., et al., *Prospective navigator correction of image position for coronary MR angiography.* Radiology, 1997. **203**(3): p. 733-736.

33. Larson, A.C., et al., *Self-gated cardiac cine MRI.* Magnetic Resonance in Medicine, 2003. **51**(1): p. 93-102.

34. Brau, A. and J.H. Brittain, *Generalized self-navigated motion detection technique: Preliminary investigation in abdominal imaging.* Magnetic Resonance in Medicine, 2006. **55**(2): p. 263-270.

35. Jin, N., et al., *Respiratory self-gating for free-breathing abdominal phase-contrast blood flow measurements.* Journal of Magnetic Resonance Imaging, 2009. **29**(4): p. 860-868.

36. Fan, Z., et al., *Prospective self-gating for swallowing motion: A feasibility study in carotid artery wall MRI using three-dimensional variable-flip-angle turbo spin-echo.* Magnetic Resonance in Medicine, 2012. **67**(2): p. 490-498.

37. Davies, S., et al., *Ultrasound quantitation of respiratory organ motion in the upper abdomen.* British journal of radiology, 1994. **67**(803): p. 1096-1102.

38. Hu, P., et al., *Motion correction using coil arrays (MOCCA) for free-breathing cardiac cine MRI.* Magnetic Resonance in Medicine, 2011. **66**(2): p. 467-475.

39. Dietrich, O., et al., *Measurement of signal-to-noise ratios in MR images: Influence of multichannel coils, parallel imaging, and reconstruction filters.* Journal of Magnetic Resonance Imaging, 2007. **26**(2): p. 375-385.

40. Li, D., et al., *Coronary Arteries: Magnetization-prepared Contrast-enhanced Three-dimensional Volume-targeted Breath-hold MR Angiography.* Radiology, 2001. **219**(1): p. 270-277.

41. Lai, P., et al., *A dual-projection respiratory self-gating technique for whole-heart coronary MRA.* Journal of Magnetic Resonance Imaging, 2008. **28**(3): p. 612-620.

42. Stehning, C., et al., *Free-breathing whole-heart coronary MRA with 3D radial SSFP and self-navigated image reconstruction.* Magnetic Resonance in Medicine, 2005. **54**(2): p. 476-480.

43. Mendis, S., et al., *Global atlas on cardiovascular disease prevention and control*. 2011, Geneva: World Health Organization in collaboration with the World Heart Federation and the World Stroke Organization. vi, 155 p.

44. Yuan, C., et al., *MRI of carotid atherosclerosis.* J Nucl Cardiol, 2008. **15**(2): p. 266-75.

45. Gillard, J.H., *Imaging of carotid artery disease: from luminology to function?* Neuroradiology, 2003. **45**(10): p. 671-80.

46. Naghavi, M., et al., *From vulnerable plaque to vulnerable patient: a call for new definitions and risk assessment strategies: Part II.* Circulation, 2003. **108**(15): p. 1772-8.

47. Virmani, R., et al., *Pathology of the vulnerable plaque.* J Am Coll Cardiol, 2006. **47**(8 Suppl): p. C13-8.

48. Saam, T., et al., *The vulnerable, or high-risk, atherosclerotic plaque: noninvasive MR imaging for characterization and assessment.* Radiology, 2007. **244**(1): p. 64-77.

49. Wasserman, B.A., et al., *Carotid artery atherosclerosis: in vivo morphologic characterization with gadolinium-enhanced double-oblique MR imaging initial results.* Radiology, 2002. **223**(2): p. 566-73.

50. Corti, R., et al., *Effects of lipid-lowering by simvastatin on human atherosclerotic lesions: a longitudinal study by high-resolution, noninvasive magnetic resonance imaging.* Circulation, 2001. **104**(3): p. 249-52.

51. Stenvinkel, P., et al., *Strong association between malnutrition, inflammation, and atherosclerosis in chronic renal failure.* Kidney Int, 1999. **55**(5): p. 1899-911.

52. Shoji, T., et al., *Advanced atherosclerosis in predialysis patients with chronic renal failure.* Kidney Int, 2002. **61**(6): p. 2187-92.

53. Schlaudecker, J.D. and C.R. Bernheisel, *Gadolinium-associated nephrogenic systemic fibrosis.* Am Fam Physician, 2009. **80**(7): p. 711-4.

54. Qiao, Y., et al., *Identification of atherosclerotic lipid deposits by diffusion-weighted imaging.* Arterioscler Thromb Vasc Biol, 2007. **27**(6): p. 1440-6.

55. Clarke, S.E., et al., *Quantitative assessment of carotid plaque composition using multicontrast MRI and registered histology.* Magn Reson Med, 2003. **50**(6): p. 1199-208.

56. Kim, S.E., et al., *In vivo and ex vivo measurements of the mean ADC values of lipid necrotic core and hemorrhage obtained from diffusion weighted imaging in human atherosclerotic plaques.* J Magn Reson Imaging, 2011. **34**(5): p. 1167-75.

57. Young, V.E., et al., *Diffusion-weighted magnetic resonance imaging for the detection of lipid-rich necrotic core in carotid atheroma in vivo.* Neuroradiology, 2010. **52**(10): p. 929-36.

58. Kim, S.E., et al., *Diffusion-weighted imaging of human carotid artery using 2D single-shot interleaved multislice inner volume diffusion-weighted echo planar imaging (2D ss-IMIV-DWEPI) at 3T: diffusion measurement in atherosclerotic plaque.* J Magn Reson Imaging, 2009. **30**(5): p. 1068-77.

59. Thomas, D.L., et al., *A quantitative method for fast diffusion imaging using magnetization-prepared TurboFLASH.* Magn Reson Med, 1998. **39**(6): p. 950-60.

60. Alsop, D.C., *Phase insensitive preparation of single-shot RARE: application to diffusion imaging in humans.* Magn Reson Med, 1997. **38**(4): p. 527-33.

61. Koktzoglou, I. and D. Li, *Diffusion-prepared segmented steady-state free precession: Application to 3D black-blood cardiovascular magnetic resonance of the thoracic aorta and carotid artery walls.* J Cardiovasc Magn Reson, 2007. **9**(1): p. 33-42.

62. Wang, J., et al., *Improved suppression of plaque-mimicking artifacts in black-blood carotid atherosclerosis imaging using a multislice motion-sensitized driven-equilibrium (MSDE) turbo spin-echo (TSE) sequence.* Magn Reson Med, 2007. **58**(5): p. 973-81.

63. Feinberg, D.A., et al., *Inner volume MR imaging: technical concepts and their application.* Radiology, 1985. **156**(3): p. 743-7.

64. Fan, Z., et al., *Carotid arterial wall MRI at 3T using 3D variable-flip-angle turbo spin-echo (TSE) with flow-sensitive dephasing (FSD).* J Magn Reson Imaging, 2010. **31**(3): p. 645-54.

65. Feinberg, D.A. and K. Oshio, *Phase errors in multi-shot echo planar imaging.* Magn Reson Med, 1994. **32**(4): p. 535-9.

66. Yuan, C., et al., *Three-dimensional fast spin-echo imaging: pulse sequence and in vivo image evaluation.* J Magn Reson Imaging, 1993. **3**(6): p. 894-9.

67. Boussel, L., et al., *Swallowing, arterial pulsation, and breathing induce motion artifacts in carotid artery MRI.* J Magn Reson Imaging, 2006. **23**(3): p. 413-5.

68. Toussaint, J.F., et al., *Water diffusion properties of human atherosclerosis and thrombosis measured by pulse field gradient nuclear magnetic resonance.* Arterioscler Thromb Vasc Biol, 1997. **17**(3): p. 542-6.

69. Grobbee, D.E. and M.L. Bots, *Carotid artery intima-media thickness as an indicator of generalized atherosclerosis.* J Intern Med, 1994. **236**(5): p. 567-73.

70. Wasserman, B.A., et al., *Low-grade carotid stenosis: looking beyond the lumen with MRI.* Stroke, 2005. **36**(11): p. 2504-13.

71. Adams, H.P., Jr., et al., *Classification of subtype of acute ischemic stroke. Definitions for use in a multicenter clinical trial. TOAST. Trial of Org 10172 in Acute Stroke Treatment.* Stroke, 1993. **24**(1): p. 35-41.

72. Mohr, J.P., et al., *American Heart Association Prevention Conference. IV. Prevention and Rehabilitation of Stroke. Etiology of stroke.* Stroke, 1997. **28**(7): p. 1501-6.

73. Antiga, L., B.A. Wasserman, and D.A. Steinman, *On the overestimation of early wall thickening at the carotid bulb by black blood MRI, with implications for*

coronary and vulnerable plaque imaging. Magn Reson Med, 2008. **60**(5): p. 1020-8.

74. Qiao, Y., et al., *Intracranial arterial wall imaging using three-dimensional high isotropic resolution black blood MRI at 3.0 Tesla.* J Magn Reson Imaging, 2011. **34**(1): p. 22-30.

75. Dieleman, N., et al., *Imaging intracranial vessel wall pathology with magnetic resonance imaging: current prospects and future directions.* Circulation, 2014. **130**(2): p. 192-201.

76. Balu, N., et al., *Comparison between 2D and 3D high-resolution black-blood techniques for carotid artery wall imaging in clinically significant atherosclerosis.* J Magn Reson Imaging, 2008. **27**(4): p. 918-24.

77. Zhu, C., et al., *Optimization of Improved Motion-sensitized Driven-equilibrium (iMSDE) blood suppression for carotid artery wall imaging.* J Cardiovasc Magn Reson, 2014. **16**(1): p. 61.

78. Li, L., et al., *Black-Blood Multicontrast Imaging of Carotid Arteries with DANTE-prepared 2D and 3D MR Imaging.* Radiology, 2014: p. 131717.

79. Jara, H., et al., *Voxel sensitivity function description of flow-induced signal loss in MR imaging: implications for black-blood MR angiography with turbo spin-echo sequences.* Magn Reson Med, 1999. **41**(3): p. 575-90.

80. Li, L., K.L. Miller, and P. Jezzard, *DANTE-prepared pulse trains: a novel approach to motion-sensitized and motion-suppressed quantitative magnetic resonance imaging.* Magn Reson Med, 2012. **68**(5): p. 1423-38.

81. Yuan, C., et al., *In vivo accuracy of multispectral magnetic resonance imaging for identifying lipid-rich necrotic cores and intraplaque hemorrhage in advanced human carotid plaques.* Circulation, 2001. **104**(17): p. 2051-6.

82. Biasiolli, L., et al., *In-vivo quantitative T2 mapping of carotid arteries in atherosclerotic patients: segmentation and T2 measurement of plaque components.* J Cardiovasc Magn Reson, 2013. **15**: p. 69.

83. Zhu, D.C., M.S. Ferguson, and J.K. DeMarco, *An optimized 3D inversion recovery prepared fast spoiled gradient recalled sequence for carotid plaque hemorrhage imaging at 3.0 T.* Magn Reson Imaging, 2008. **26**(10): p. 1360-6.

84. Felmlee, J.P. and R.L. Ehman, *Spatial presaturation: a method for suppressing flow artifacts and improving depiction of vascular anatomy in MR imaging.* Radiology, 1987. **164**(2): p. 559-64.

85. Constantinides, C.D., E. Atalar, and E.R. McVeigh, *Signal-to-noise measurements in magnitude images from NMR phased arrays.* Magn Reson Med, 1997. **38**(5): p. 852-7.

86. Pelc, L.R., et al., *Arterial and venous blood flow: noninvasive quantitation with MR imaging.* Radiology, 1992. **185**(3): p. 809-12.

87. Dormont, D., et al., *MRI in cerebral venous thrombosis.* J Neuroradiol, 1994. **21**(2): p. 81-99.

88. Swartz, R.H., et al., *Intracranial arterial wall imaging using high-resolution 3-tesla contrast-enhanced MRI.* Neurology, 2009. **72**(7): p. 627-34.

89. Wang, J., V.L. Yarnykh, and C. Yuan, *Enhanced image quality in black-blood MRI using the improved motion-sensitized driven-equilibrium (iMSDE) sequence.* J Magn Reson Imaging, 2010. **31**(5): p. 1256-63.

90. Crowe, L.A., et al., *3D volume-selective turbo spin echo for carotid artery wall imaging with navigator detection of swallowing.* J Magn Reson Imaging, 2005. **22**(4): p. 583-8.

91. Fan, Z., et al., *Prospective self-gating for swallowing motion: a feasibility study in carotid artery wall MRI using three-dimensional variable-flip-angle turbo spin-echo.* Magn Reson Med, 2012. **67**(2): p. 490-8.

92. Maintz, D., et al., *Selective coronary artery plaque visualization and differentiation by contrast-enhanced inversion prepared MRI.* Eur Heart J, 2006. **27**(14): p. 1732-6.

93. Kawasaki, T., et al., *Characterization of hyperintense plaque with noncontrast T(1)-weighted cardiac magnetic resonance coronary plaque imaging: comparison with multislice computed tomography and intravascular ultrasound.* JACC Cardiovasc Imaging, 2009. **2**(6): p. 720-8.

94. Noguchi, T., et al., *High-Intensity Signals in Coronary Plaques on Non-contrast T1-Weighted Magnetic Resonance Imaging as a Novel Determinant of Coronary Events.* J Am Coll Cardiol, 2013.

95. Varma, N., et al., *Coronary Vessel Wall Contrast Enhancement Imaging as a Potential Direct Marker of Coronary Involvement: Integration of Findings From CAD and SLE Patients.* JACC Cardiovasc Imaging, 2014. **7**(8): p. 762-70.

96. Pang, J., et al., *Whole-heart coronary MRA with 100% respiratory gating efficiency: self-navigated three-dimensional retrospective image-based motion correction (TRIM).* Magn Reson Med, 2014. **71**(1): p. 67-74.

97. Kolodgie, F.D., et al., *Intraplaque hemorrhage and progression of coronary atheroma.* N Engl J Med, 2003. **349**(24): p. 2316-25.